III. The Silicon Tracker

1) Introduction

The AMS-02 Tracker (Figure 64) will extend the energy range of the spectrometer into the TeV region and improve its particle identification capabilities. Coordinated by R. Battiston it is designed and built by an international collaboration of Univ. and INFN-Perugia (B. Alpat), University of Geneva (M. Bourquin, M. Pohl), Aachen Ist Institute (K. Lübelsmeyer, S. Schael, W. Wallraff), NLR (M. Brouwer), Holland, University of Turku (J. Torsti), MIT (M. Capell), Taiwan (S.C. Lee, H. Chang) and ETHZ (G. Viertel) and NIKHEF.

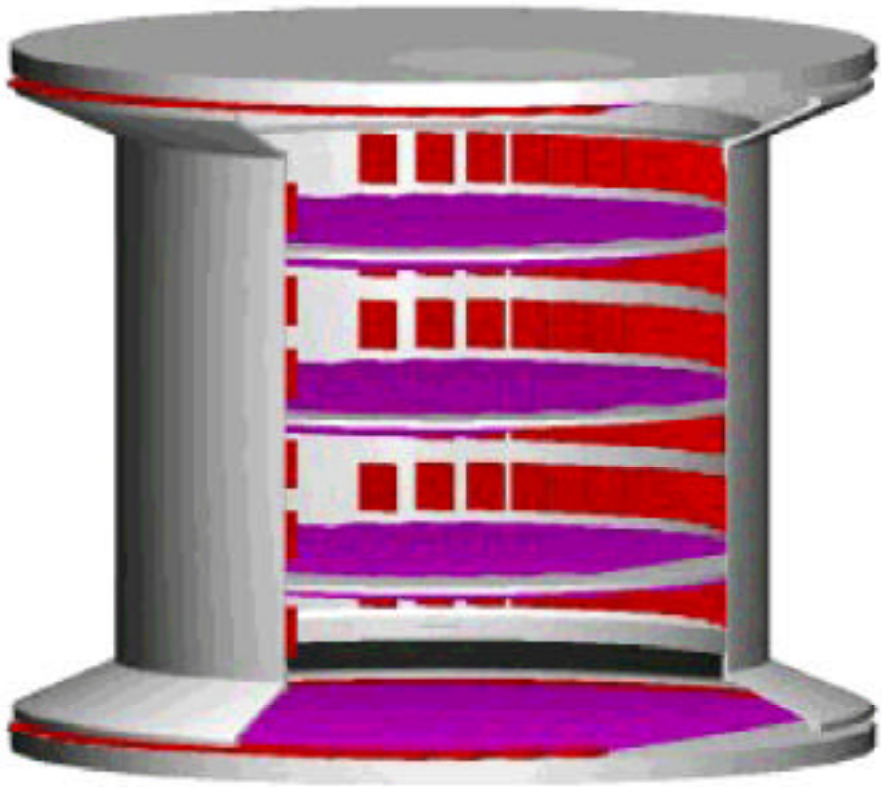

Figure 64: Schematic layout of the AMS tracker. The support structure is shown in grey, the 8 layers of silicon ladders in violet and front-end readout electronics in red.

The success of AMS-01 shows that we can indeed use large quantities of accelerator grade precision silicon in a magnetic spectrometer in space. To match with the higher field of the cryomagnet, the Tracker group has spent considerable effort to work with industry (particularly COLYBRIS, Switzerland) to improve the resolution and to reduce the dark current of the silicon

sensors. Furthermore, in order to re-use the extra high precision support structure developed for AMS-01, we have built the cryomagnet with the same inner diameter as that of the AMS-01 magnet (Figure 65). To have more layers for redundancy and improve the momentum resolution, the arrangement of the inner planes has changed (Figure 64): three inner planes will be used fully equipped with silicon sensors on both sides. The outermost two planes will also be completely covered with sensors for a total of 8 layers. The design and prototyping for the new Silicon Tracker has been completed and production of the silicon detectors is progressing well. The new design requires the production of a total of 192 ladders corresponding to 2270 silicon sensors.

Figure 65: The AMS Silicon Tracker after the STS91 mission.

2) Silicon Ladder Production

The Tracker building blocks are the silicon sensors, each having an active surface of 4×7 cm^2 (Figure 66). The main differences between AMS-01 and AMS-02 silicon detectors are a lower leakage current, a thicker metalization on the strips, and a modified biasing method on the non-bending plane to increase the polarization resistance. These modifications improve the signal to

noise (S/N). A passivation layer has also been deposited on the AMS-02 detectors to protect them against mechanical damage during assembly. A typical current distribution is shown in Figure 67.

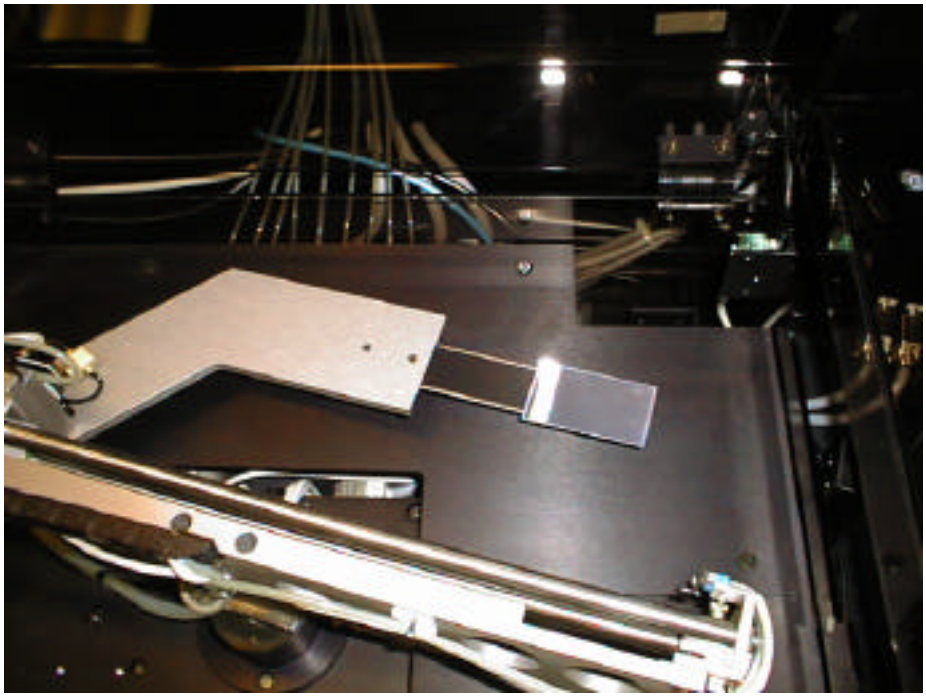

Figure 66 : A silicon detector on the automatic test station at INFN-Perugia.

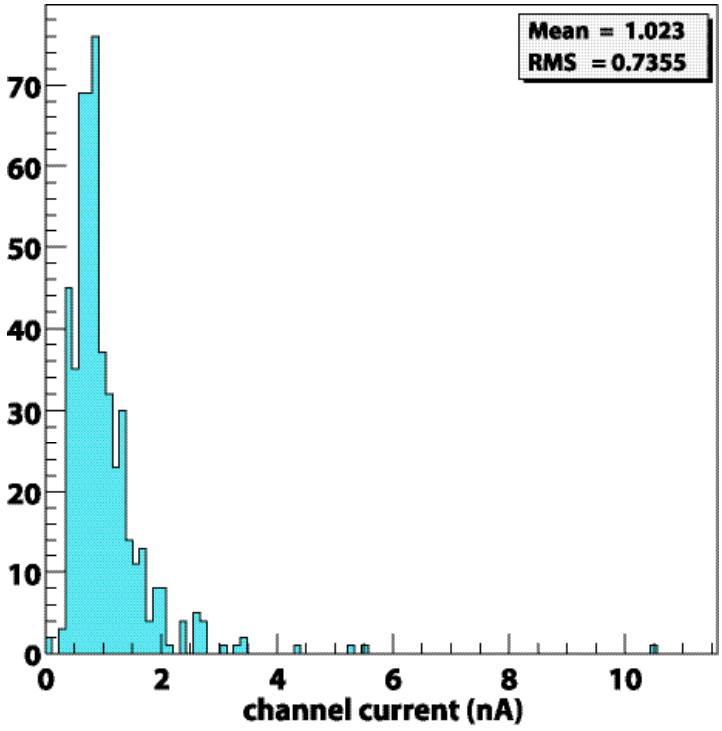

Figure 67 : Typical current distribution.

The sensors are interconnected in groups of up to 15 elements into a “ladder”. The structure of an AMS-02 tracker ladder is very similar to the one used for the AMS-01 flight (Figure 68).

The ladders cover eight layers assembled onto five support planes (Figure 69), with a total active surface of more than six square meters. With this large equipped area the AMS Silicon Tracker will be the largest assembly of silicon detectors before the advent of LHC detectors (Table 12). The corresponding assembly effort takes place in three laboratories operating in parallel with identical procedures located at University and INFN of Perugia, at G&A Engineering (Carsoli, Aquila) supported by the Italian Space Agency and at the Geneva University and CERN (operated by ETHZ).

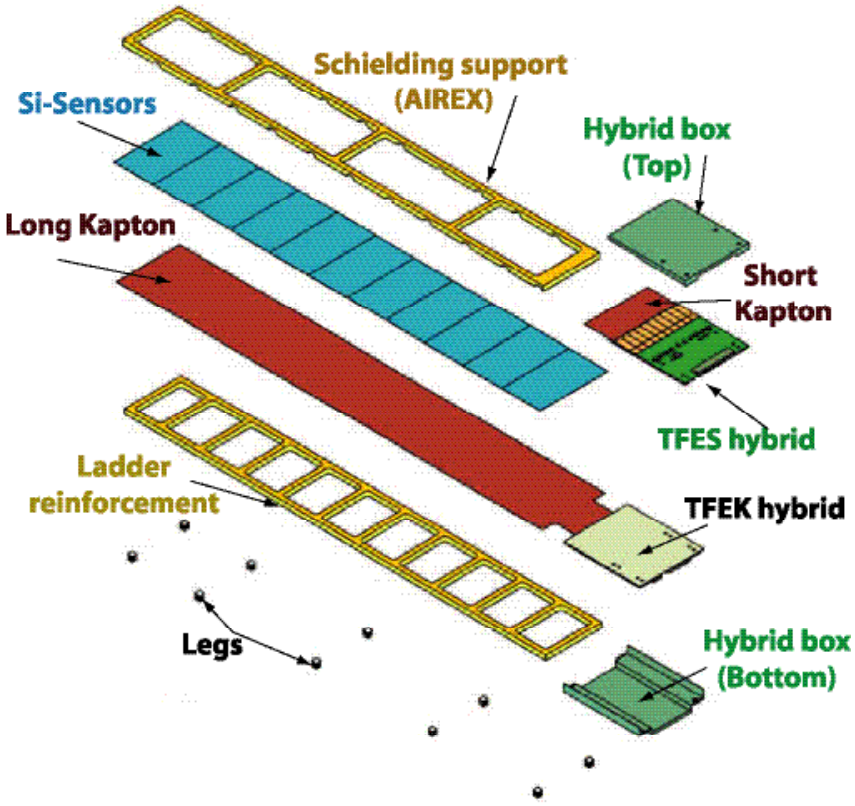

Figure 68: Expanded view of an AMS ladder showing the components needed in assembly and integration. The outer electromagnetic shielding is not shown.

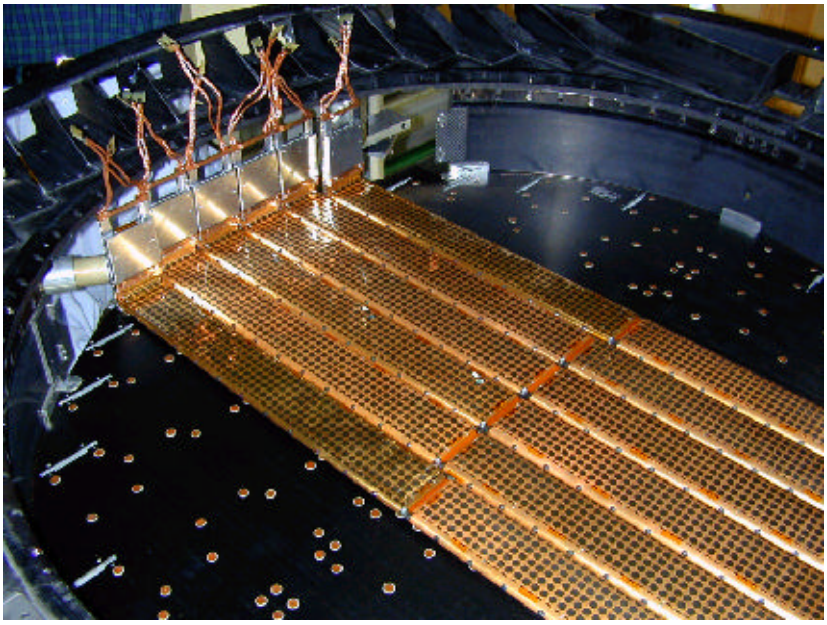

Figure 69: Silicon ladders, with shielding, equipping one of the 8 AMS Tracker planes.

All laboratories are located in Class 10000 clean rooms which are also being used extensively for electrical tests, ladder integration and plane installation activities, including storage of completed ladders.

The production of a ladder starts with the gluing of several sensors on to a upilex flex cable used to drive the side signals to the readout located at one end of the ladder. This assembly is then glued on to a carbon fiber stiffening frame: this submodule undergoes metrology control to check its dimensions with a few micron accuracy (Figures 70, 71).

The prefabricated modules undergo strip bonding and readout hybrid mounting and bonding. Completed ladders are then submitted to feet gluing, shield fixture gluing, shield wrapping and fixing, and final electrical tests before installation on the support planes. The shielding foil is made of 50 μm Kapton coated on both sides with a 3 μm copper pattern.

Experiment	#Channels	Area-m^2	#detectors
AMS-02	196 K	6.45	2300
CDF-SVX II	405 K	1.88	720
ALEPH	95 K	0.49	144
L3	86 K	0.23	96

Table 12: Comparison of existing silicon tracker detectors

Figure 70 (left): Sensor positioning under metrology control. Figure 71 (right): wire bonding of sensors, on a silicon ladder of the AMS-02 production (Geneva University and CERN/ETHZ).

Many mechanical and electrical prototypes have been built to validate the final assembly procedure of the new AMS-02 tracker modules and to fully test the compatibility of the three assembly lines. They also served to finalise parameter settings (metrology, glue dispenser, bonding). The "flight quality" ladder assembly has then started at each of the three assembly lines.

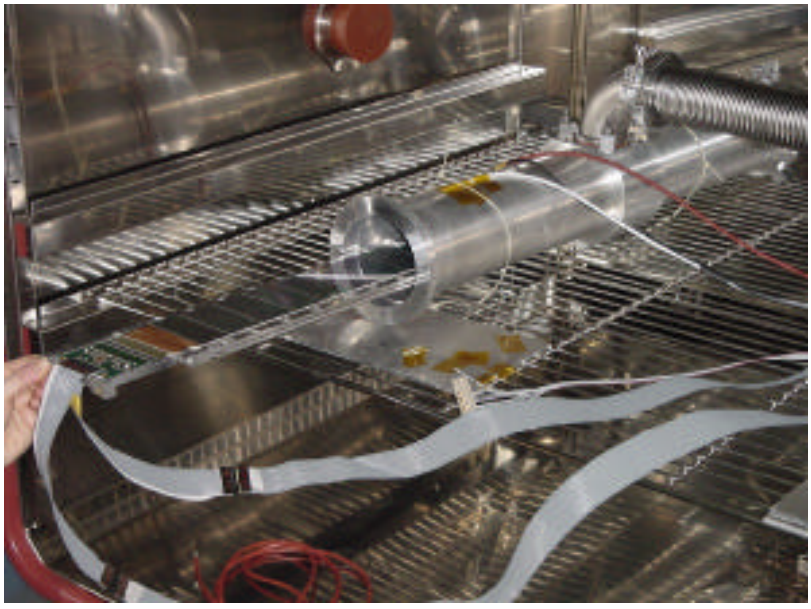

Figure 72: Thermovacuum test of an AMS-02 silicon ladder at the University of Perugia.

Systematic tests for space qualification of the Tracker ladders have been carried out to prove that modules will indeed withstand the extreme thermal and mechanical conditions at launch and landing of the Space Shuttle and during operation for three years in space (Figure 72).

During all phases of the assembly and testing of the ladders all the relevant information are stored online in a relational database. The database contains all the information relative to the construction of the detector, such as the names of the individuals at each production step, description and characteristics of components and results of quality control tests. It also contains an index of calibration files which will be used to reconstruct the measured events on ISS.

The production rate is 1.5 ladders/week/assembly line, while the integration and test rate is 5 ladders per week. This is sufficient to fully equip and test 192 ladders for all eight sensitive tracking layers in time for a beam test at CERN in 2002 and final system integration at ETH Zurich in spring 2003.

3) Tracker Test Beam Results

In September 2000, the new prototype ladder was tested at CERN with 120 GeV muons. The goals of this test were the validation of the new silicon and the new VA front-end chip. 200,000 events were collected and the analysis of the results shows an improved performance compared to the AMS-01 sensors.

After event selection, a fit to the distribution of the residuals yields a resolution of 8.5 μm and 30 μm on the two sides, as shown in Figure 73. The corresponding resolutions for AMS-01 were 10 μm and 30 μm (see chapter II).

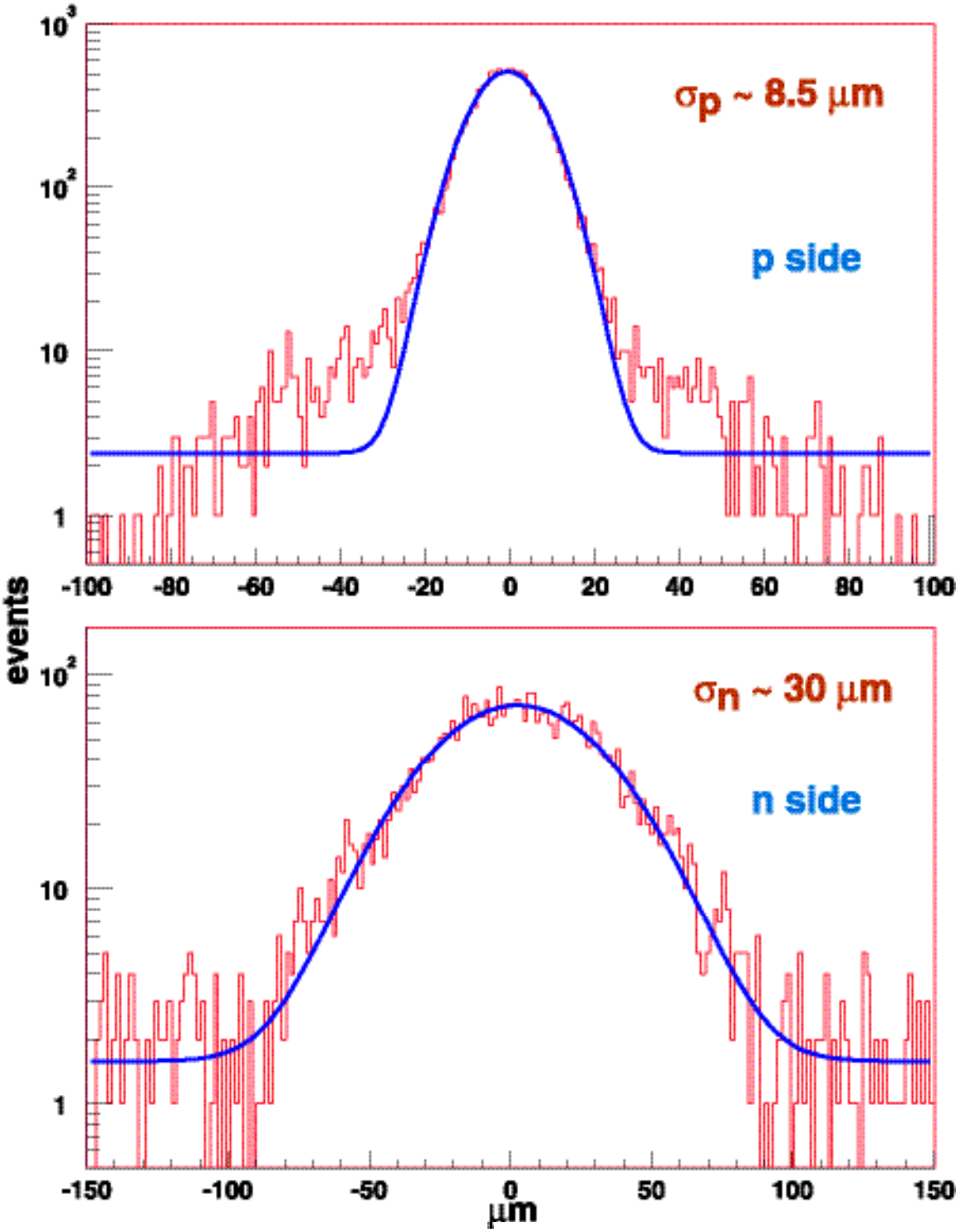

Figure 73: Residual distribution of hits on the prototype ladder with respect to the position expected from the beam telescope. The resolution is 85 μm on the p-side (bending plane) and 30 μm on the n-side (non bending plane).

With respect to the AMS-01 design, on the new AMS-02 n-side the width of the strip metalizations are increased to 40 μm, while two of the three intermediate strips are suppressed yielding a better charge collection efficiency. In the neighbourhood of a strip, the whole charge

is collected by one strip, giving a resolution of 104 μm/$\sqrt{12}$ where 104 μm is the strip pitch. Between strips an improved resolution of 9 μm is obtained after correction (Figure 74).

The most probable values of the S/N distribution of matched clusters are 12.0 and 7.6 for the two sides. The charge correlation between the sides is 23%, with an average charge loss on the n side of 3.6%. Requesting the extrapolated track to hit a region of the detector without defects, an intrinsic efficiency of 99% is obtained.

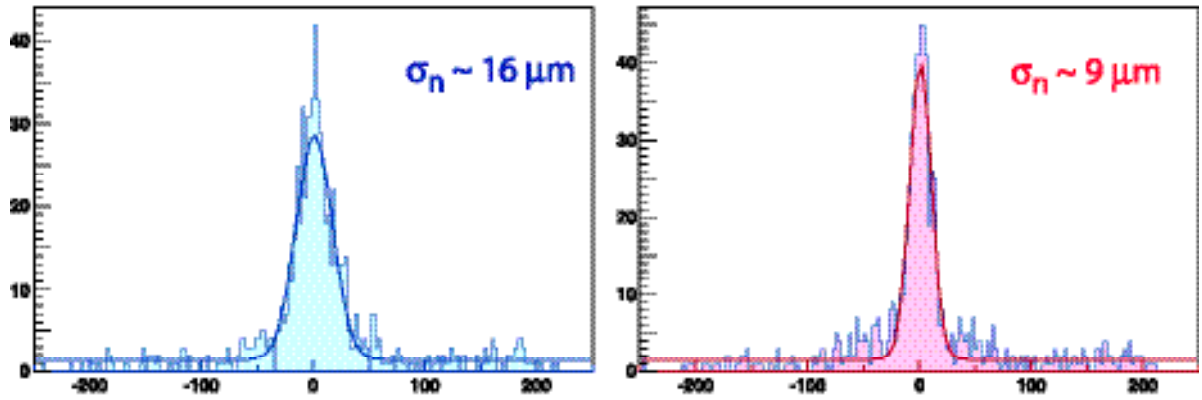

Figure 74: n-side resolution for particles impinging between two strips (left). After correction a resolution of 9 μm is obtained (right).

4) Tracker Thermal Design

The AMS-Tracker cooling system (Figure 75) is a mechanically pumped two-phase loop with carbon dioxide (CO_2) as the working fluid coupled to a set of thermal bars connected to the front-end hybrids. CO_2 was chosen as refrigerant because of its very good thermodynamical properties and the possibility of using small diameter evaporators. This small amount of cooling system hardware inside the AMS-Tracker makes integration possible with the existing tracker hardware. The complicated tracker support structure can therefore be reused for AMS-02, while no major modifications have to be made to accommodate this cooling system. Figure 76 shows a test setup in which a CO_2 system was proven to work within the thermal specifications of the AMS-Tracker

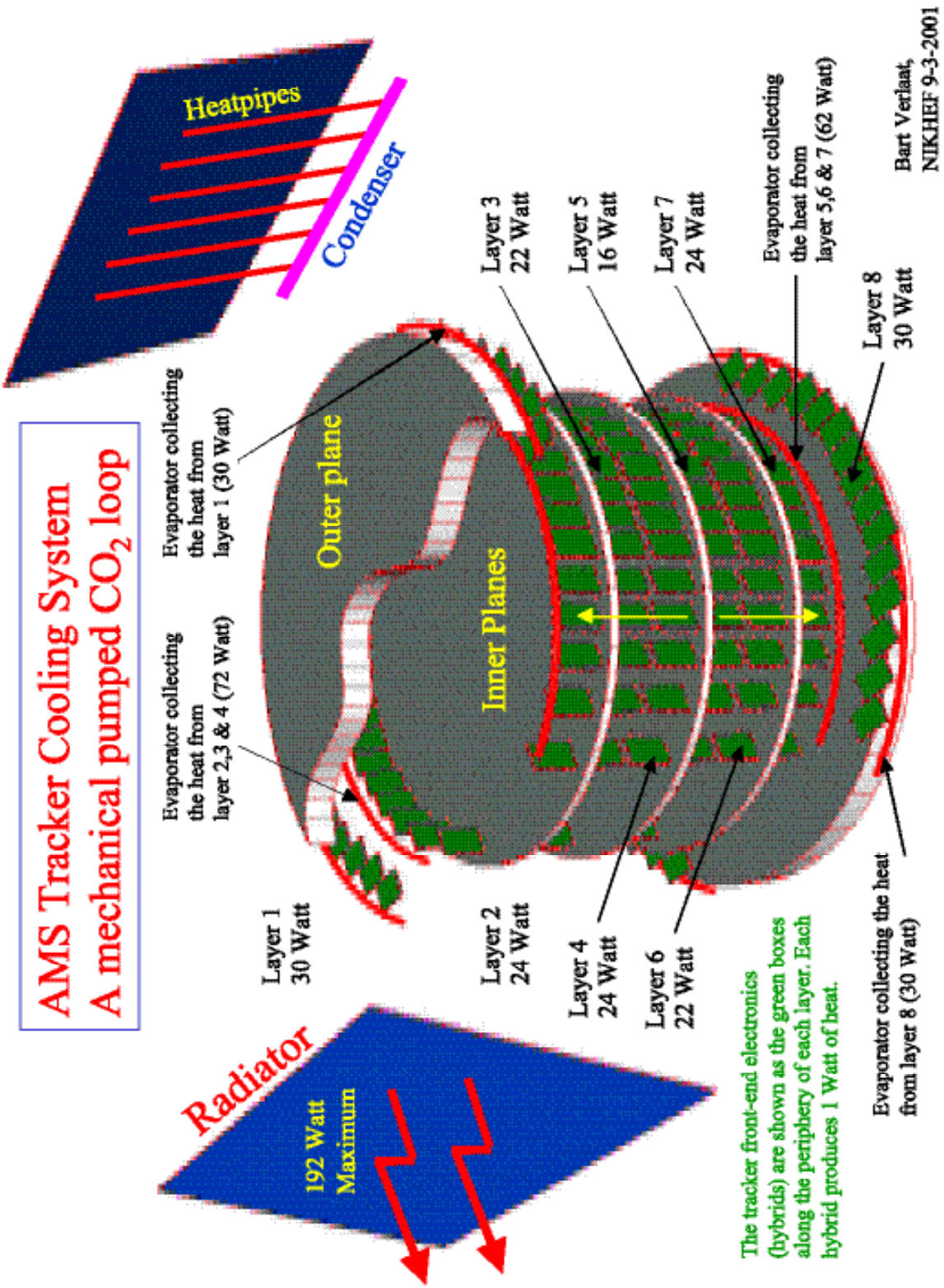

Figure 75: Thermal control system of the AMS-02 Silicon Tracker.

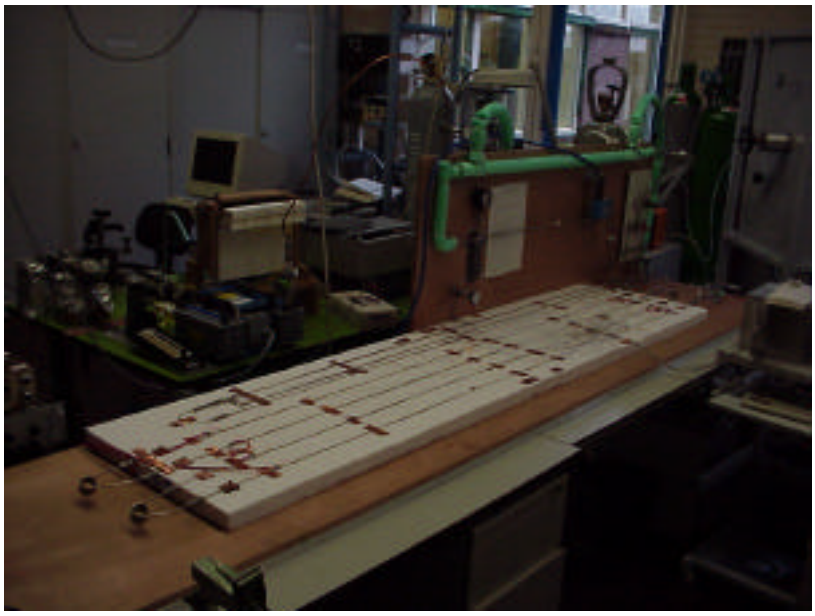

Figure 76: Test of the CO_2 two phases cooling loop at NIKHEF.

The result of the calculated temperature gradient for two extreme ISS attitude cases is shown in Figure 77. These results show that it will be possible to reach small (~1°) temperature gradients within the Tracker. The Tracker system effort will be shared with the new AMS collaborators from the Dutch National Aerospace Laboratory, NLR, with help from NIKHEF, Amsterdam.

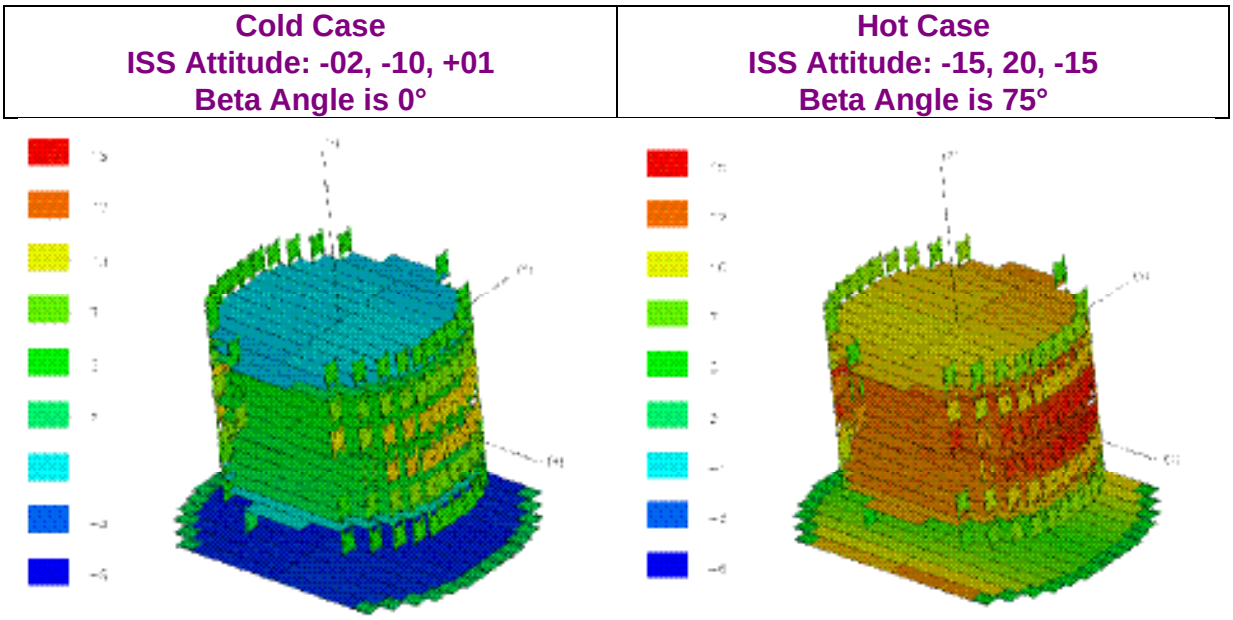

Figure 77: Finite Elements Analysis of Tracker temperature distributions for two extreme ISS attitude cases. The scales are in degree Celsius.

5) Tracker Electronics

The front-end hybrids containing the front-end readout are an improved version of the AMS-01 hybrid based on the VA_Hdr64 low noise preamplifier. This new version is based on submicron (0.8 μm) technology and is also more resistant to ionizing radiation.

As ground support equipment a new PC based test system, complete with power supply has been developed to test the functionality of detectors and readout electronics at each processing step. This test system is available at all production lines, thus enabling consistent measurements of relevant parameters.

There is one Tracker Data Reduction unit, TDR, per ladder, integrated in pairs onto a single board. This board is the interface between the detector front-end electronics and the main AMS DAQ system. It also distributes and monitors the power to the front-end. The TDR has two functional blocks: the Detector Dependent Part, DDP, and the Common Digital Part, CDP. For AMS-02 each subdetector (Tracker, TRD, etc…) will design and test the different DDPs but there will be a unified design of the CDP.

For the tracker the DDP will consist of three analog chains and a glue logic gate array to interface with the CDP. Each analog chain is composed of:

- an amplifier (AD8051), that will shape the analog signal from the front-end.
- a 12-bit parallel, low power ADC able to digitise at 5 MHz (AD803S).

Further details will be found in the Electronics section below.

6) Space Qualification

Space qualification testing includes vibration, pressure, thermal vacuum, thermal cycling and radiation resistance. These tests are performed in facilities which are available to the AMS Collaboration. For example, several of these qualification tests will be performed at the Universita' of Perugia, Terni section where an integrated group of laboratories is being developed for space applications (Figure 78) as well as at Aachen.

Radiation tests to qualify COTS (Commercial Off The Shelf) components for space are also routinely performed at Casaccia (Rome) (Cobalt source total dose tests), GSI (Darmstadt) (high energy heavy ions) and the INFN Laboratory of Legnaro (Padova) (low energy heavy ions) where a test beam line dedicated to AMS has been set up (Figure 79).

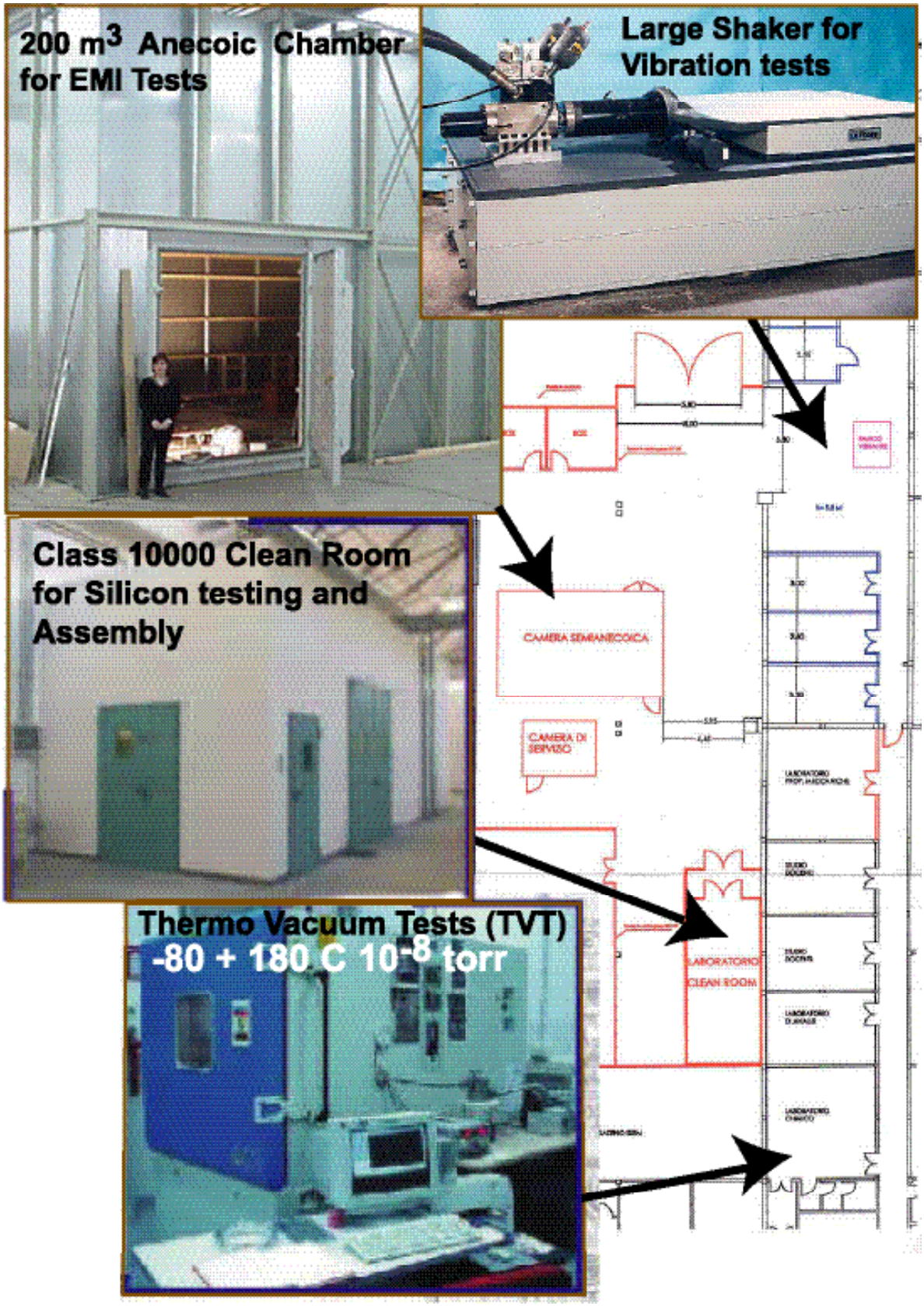

Figure 78: Space Qualification Laboratories at the University of Perugia, Terni Section.

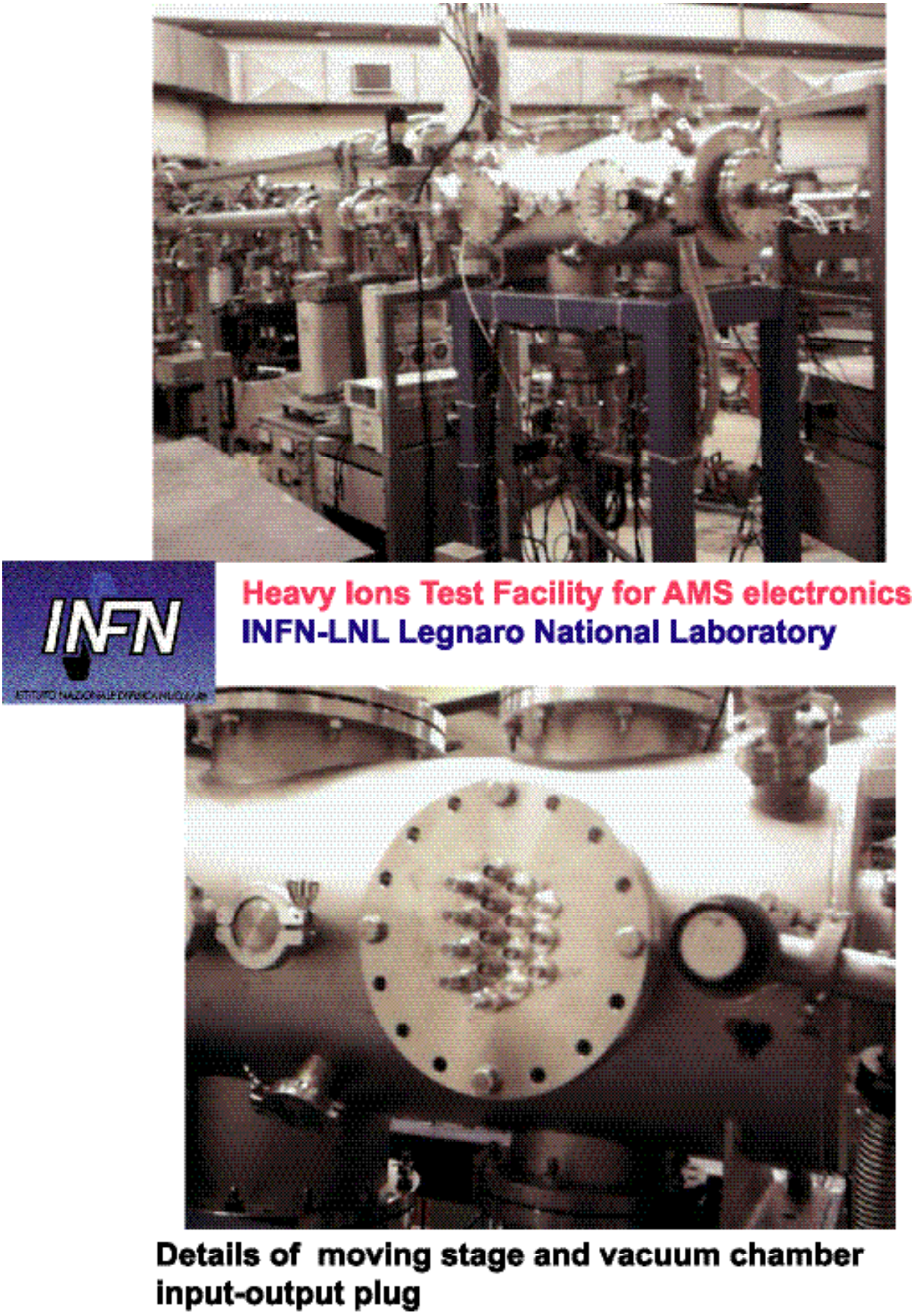

Figure 79: AMS Heavy Ions Beam exposure facility for electronics qualification at INFN Legnaro Laboratories.

7) Tracker Alignment

In order to maintain the precise momentum measurement, the Tracker position must be known with an accuracy of better than a few microns. Straight tracks measured with the Silicon sensors themselves are the most appropriate tool for an alignment check of these sensors on the 8 detector planes.

Following the successful laser alignment technique developed by W. Wallraff at RWTH-I, we will use 10 laser rays to maintain the tracker alignment at all times (see also chapter II). From our AMS-01 experience the alignment will be straightforward. One purpose of the beam tests foreseen in 2002 and 2003 will be to cross check tracker alignment.

IV. The Time-of-Flight system of AMS02.

1) Design considerations

The use of a superconducting magnet has the consequence that the TOF system had to be redesigned to operate in a strong magnetic field.

The TOF system is under construction at the INFN Laboratories in Bologna (under the leadership of A. Zichichi, A. Contin, F. Palmonari, G. Laurenti and others.) and will provide:

(i) the fast trigger;

(ii) the measurement of the time of flight of the particles traversing the detector with a resolution sufficient to distinguish upward from downward going particles at a level of at least 10^{-10} to 10^{-11};

(iii) the measurement of the absolute charge of the particle .

The main TOF system characteristics are:

(i) Total sensitive area: ≈ 1.6 m^2 per plane.

(ii) Trigger selection: for an efficient background rejection, the system consists of two pairs of planes, one before and one after the magnet, with the paddles arranged perpendicularly to each other in the two planes of each pair.

(iii) Weight: ≤ 280 kg.

(iv) Power consumption: ≤ 150W

(v) Time-of-flight resolution: ~ 120 ps

(vi) Operation in space: the counters are housed in mechanically robust and light-tight covers with a system for fast depressurization. In addition the system must have redundancy.

2) Construction of the TOF:

The AMS-02 superconducting magnet produces a field (about 2 to 3 kG) in different directions on the TOF planes. Figure 80 shows the magnetic field at the vertical coordinates where the TOF planes are positioned. To work in such conditions the light detectors must withstand the magnetic field without much shielding in a large interval of angular orientation with respect to the field direction.

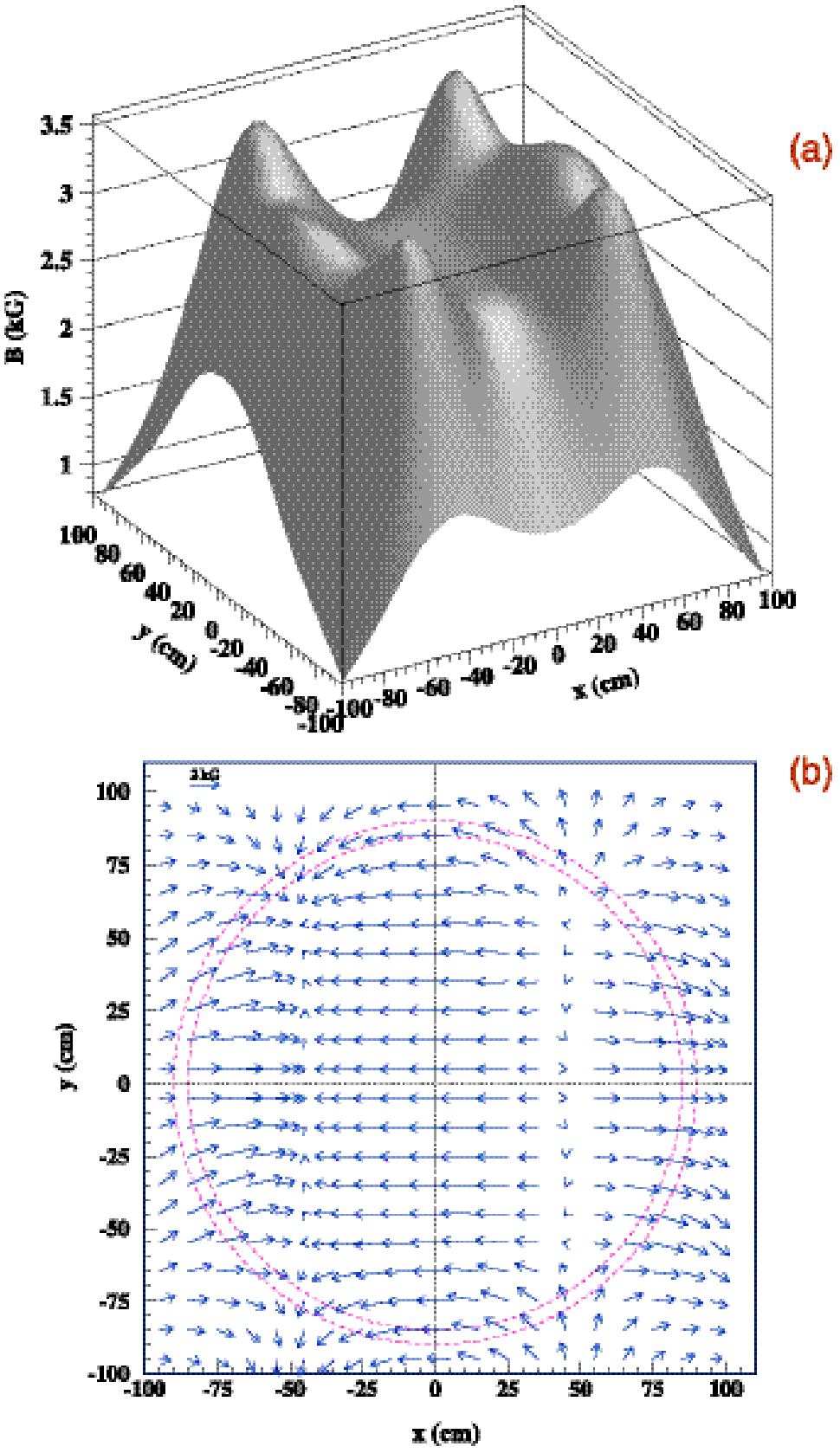

Figure 80: (a) The magnetic field magnitude at Z=60 cm (b), its component in the plane at *z*=60cm. The dashed circles in (b) represent the approximate position of the TOF system PMs.

(i) The Photomultiplier (PM)

After a market study, the Hamamatsu R5946 photomultiplier tube (with a photocathode area 572 mm^2) was considered the best choice. We have thoroughly tested these PMs for time resolution and pulse height response in magnetic field. The test setup (shown in Figure 81) includes a red light emitting diode (LED) operated through a CAMAC module, which provides a variable pulse with amplitude between 0 and –20 V and duration between 5 and 100 ns. The system is clocked at about 20 Hz.

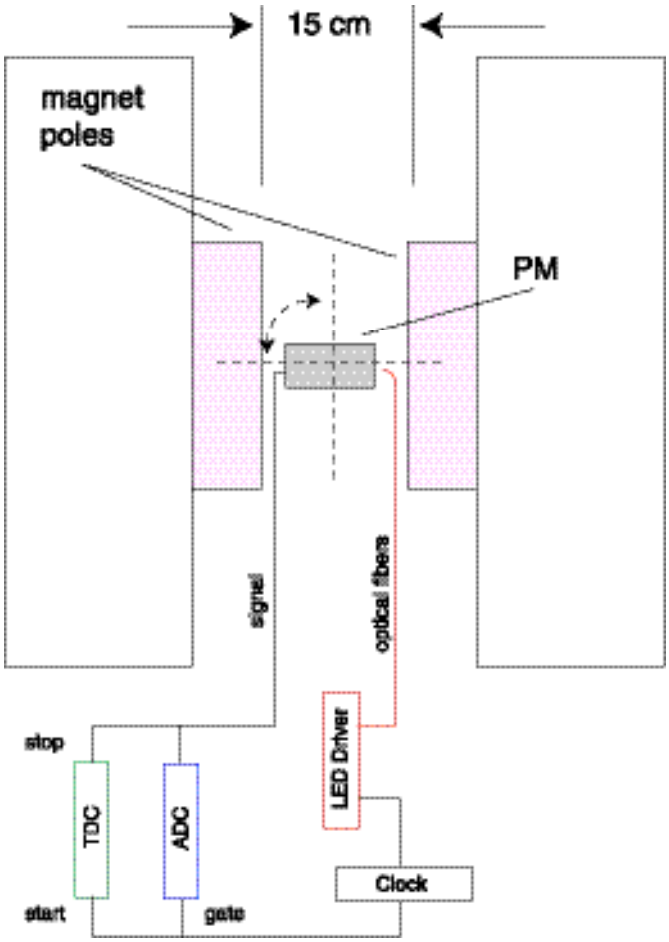

Figure 81: The experimental setup used for the measurement of the PM behaviour in magnetic field. The maximum field is 5 kG.

The light is guided to the PM by two optical fibres. The PM is placed between the poles of an electro-magnet (maximum field 5 kG) on a movable stand which can be rotated at a maximum angle of 90°. The charge signal from the photomultiplier is digitized by an ADC with two 12-bit scales (0.25 pC/channel and 0.033 pC/channel, respectively) and registered by a PC-based data acquisition system.

(ii) PMs gain and energy response

As the gain of the R5946 PMs show large variations from sample to sample (about a factor of 6), three PMs were selected for testing in magnetic field: one with high gain, one with intermediate gain and one with low gain. All three PMs were then operated at a gain of about 2 x 10^6, with voltages of 1700 V, 2000 V and 2200 V, respectively.

The PM responses have been measured for different values of the magnetic field B and of the angle θ between the PM axis and the field. Figures 82 shows the response of the PMs at different values of the magnetic field, relative to that at B=0 G, as a function of θ. For angles ≤ 50° the relative response variation is not greater than 50% up to the highest values of B. At θ ≥ 60° the response degrades quickly for B ≥ 1000 G.

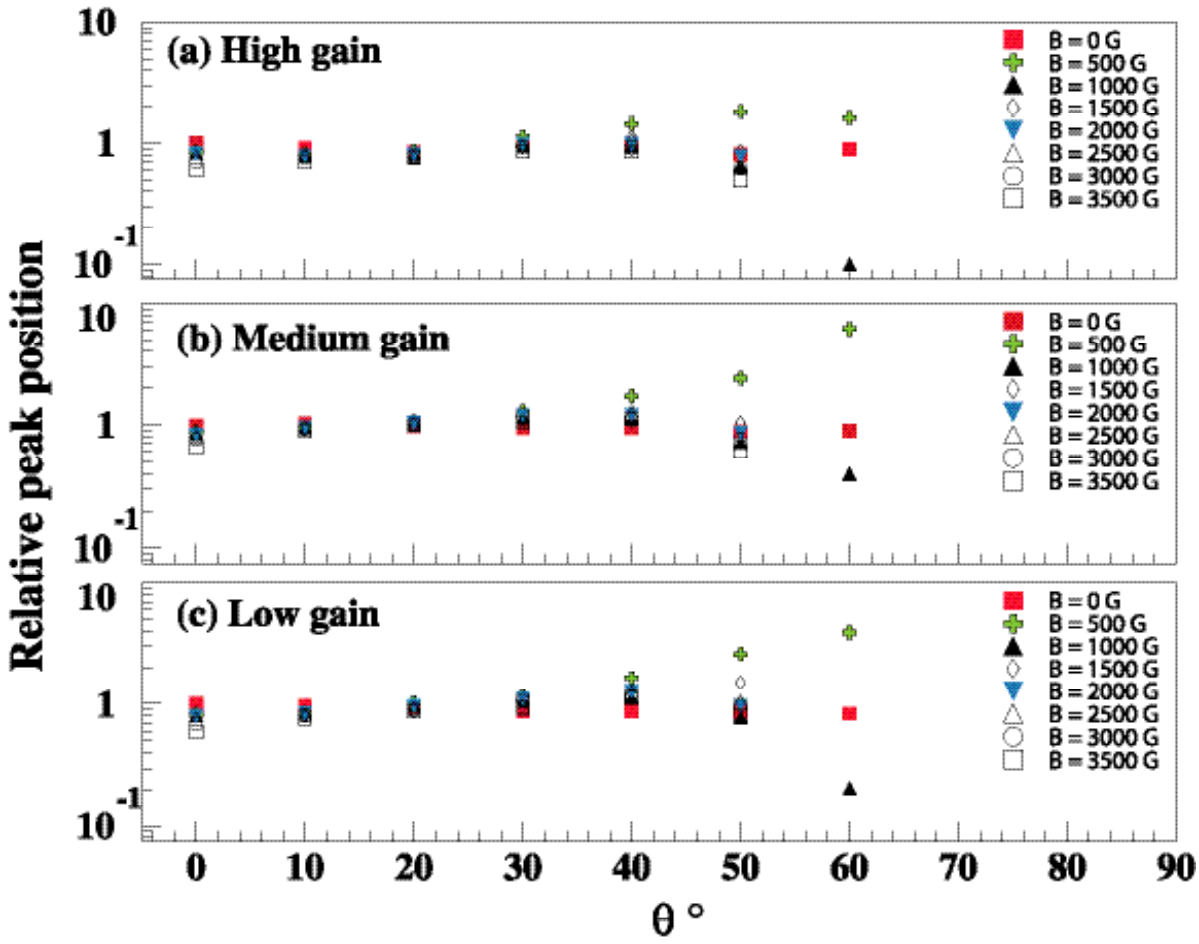

Figure 82: The relative response of the three PMs as a function of the angle θ between the PM axis and the field direction, for different values of the magnetic field B. The PM response is seriously degraded for θ ≥ 60°

The single photoelectron response has been measured using a very low-level light pulse from the LED for several PM orientations and field magnitudes. The resolution degrades rapidly with increasing magnetic field at large angles and with increasing angle at fixed magnetic field. A summary of the resolution measurements is shown in Figure 83 for the three PMs and for different values of the magnetic field and of the angle θ. The consequence of the worsening of the single photoelectron resolution with increasing field and θ is a small degradation in the energy measurement resolution, as shown in Figure 84 for High gain PM when illuminated with a signal equivalent to about 240 photoelectrons.

No difference has been seen between the three categories of PMs.

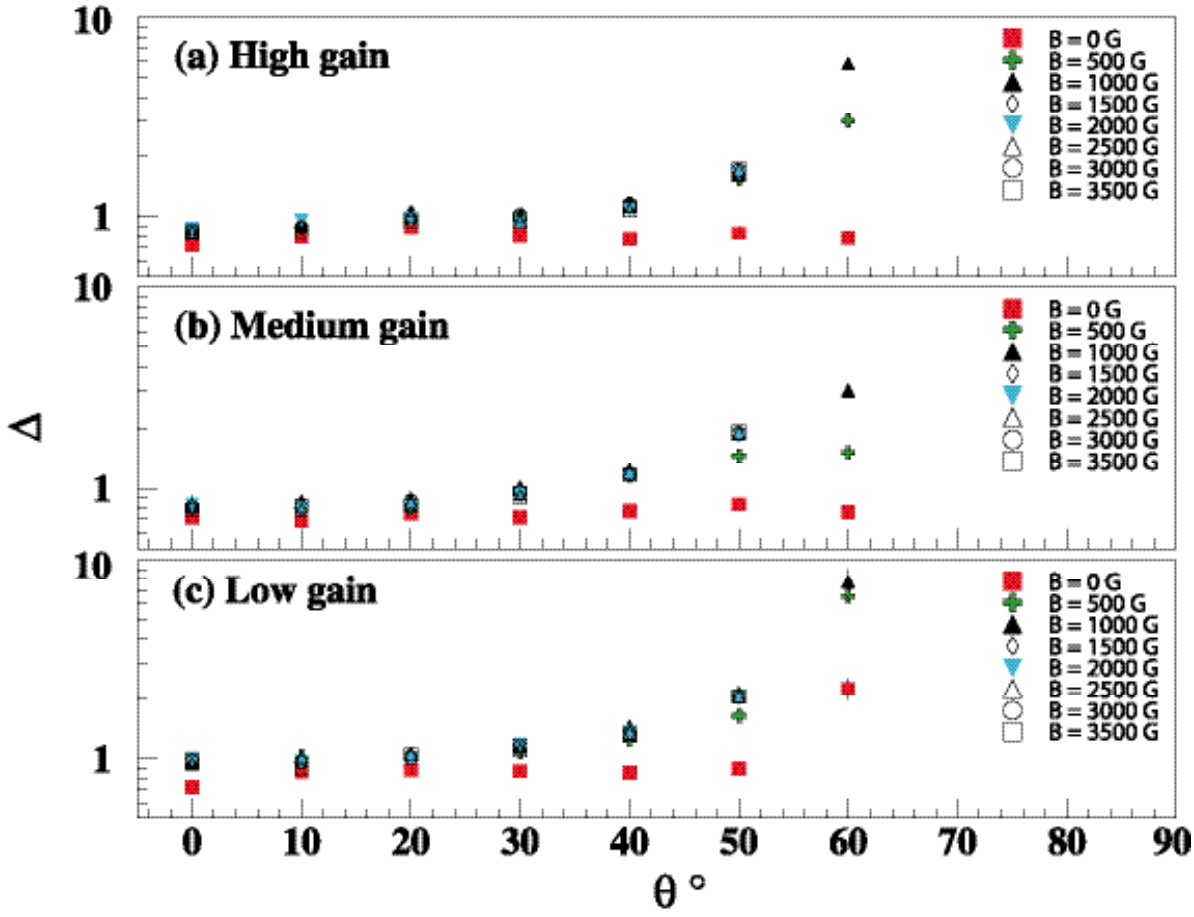

Figure 83: Single photoelectron resolution Δ=(signal spread / peak position)as a function of the angle with respect to the field direction for the three PMs and for different values of the magnetic field.

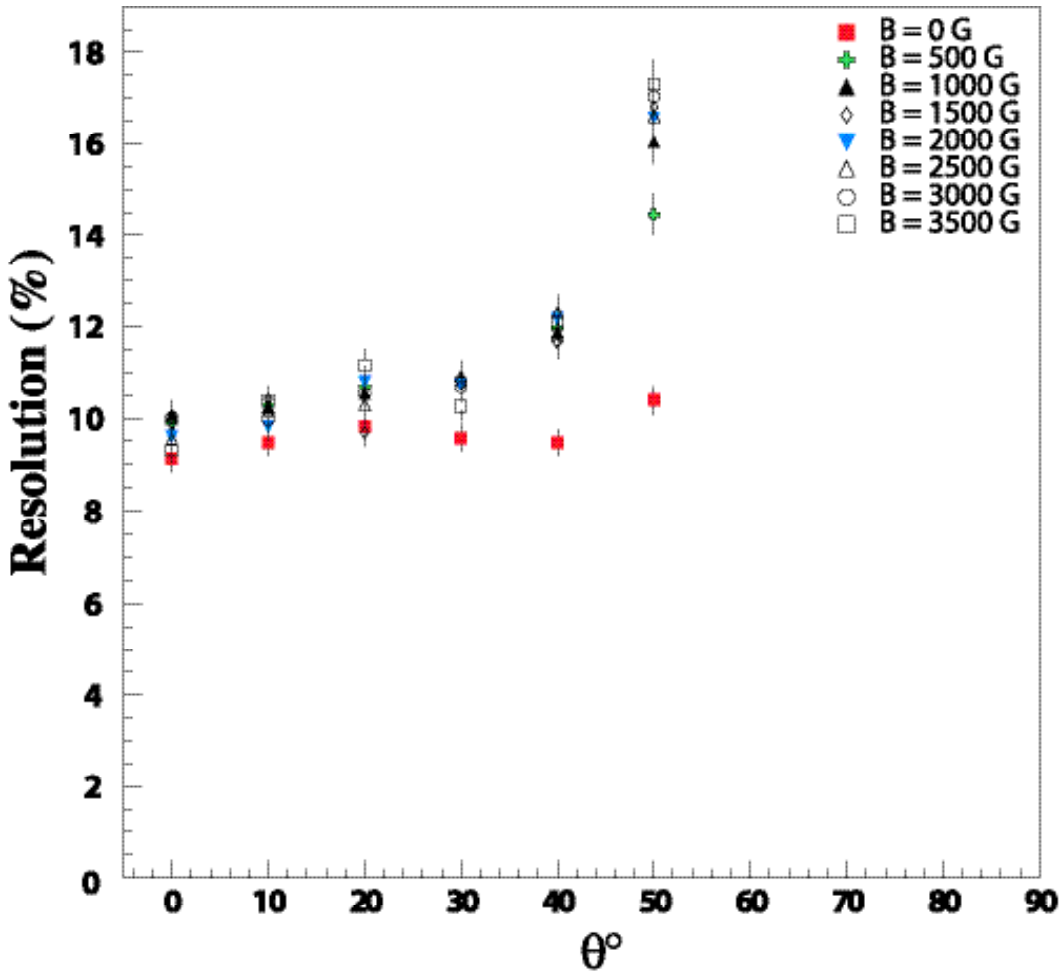

Figure 84: Energy resolution for a signal, equivalent to a minimum ionizing particle (240 photoelectrons) as a function of the angle with respect to the field direction and for different values of the magnetic field.

(iii) Time resolution

Although the test system has not been designed for a very precise measurement of the time resolution of the PMs, some conclusions on the effect of the magnetic field can nevertheless be drawn. The signal from the PM is sent to a discriminator (with the threshold set at 30 mV) and then to the *stop* input of a 50 ps/bin TDC, started by the pulse driving the LED.

The transit times and the time resolutions for Low gain PM and High gain PM are shown in Figure 85 as function of the magnetic field and for different values of θ. The most relevant observation is that the PM operated at higher voltage (Low gain PM) shows a shorter transit time and a better time resolution. A strong correlation is observed between the time resolution and the transit time for both PMs and a serious degradation in the time resolution is found for $\theta \geq 30°$.

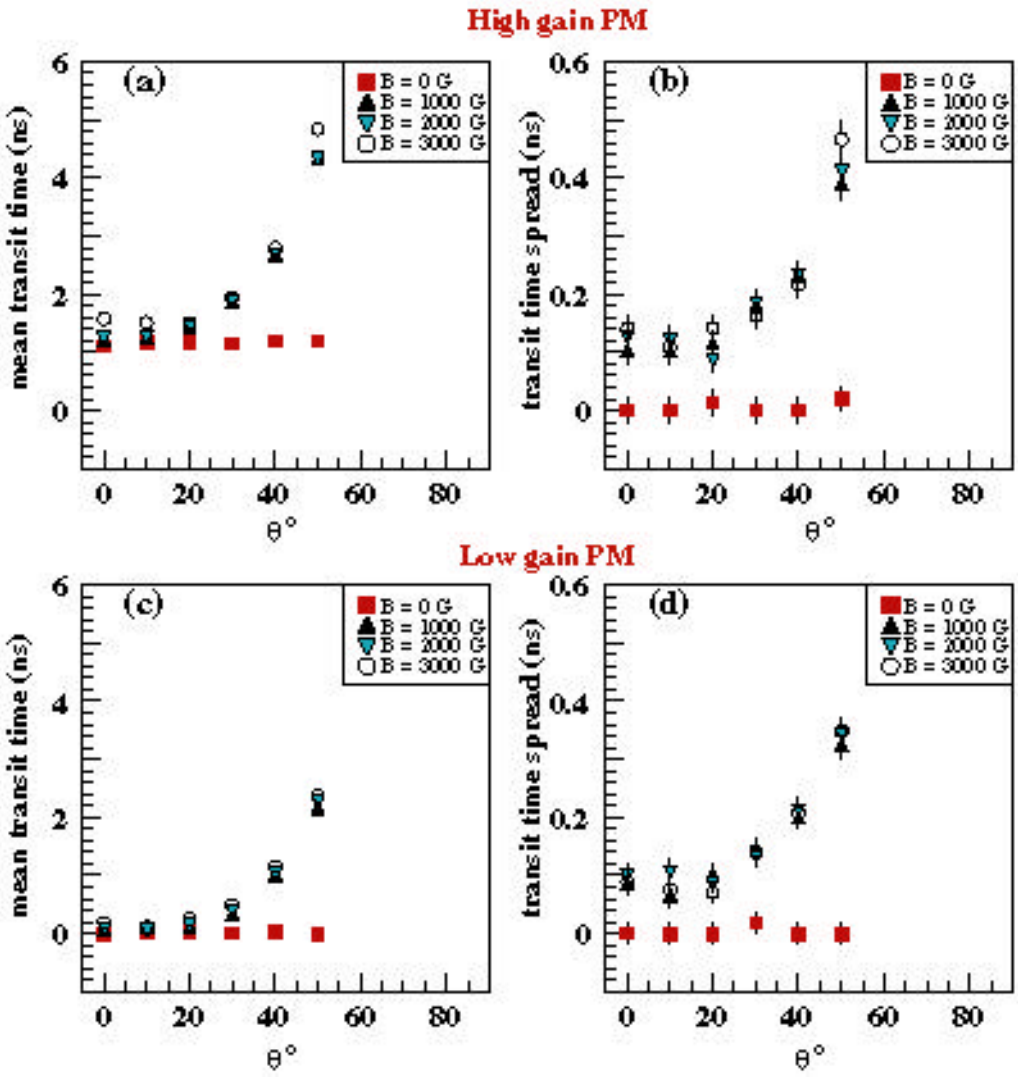

Figure 85: Time delay with respect to LED ('mean transit time') and transit time spread as function of the magnetic field and the value of θ for High gain PM (a,b) (higher gain - lower voltage: 1700 V) and Low gain PM (c,d) (lower gain - higher voltage: 2200 V). The mean transit times are compared to the transit time of Low gain PM at B=0 G. The transit time spread at B=0 G is subtracted. The PM operated at higher voltage shows the shorter transit time and the lower transit time spread.

(iv) Module design

- Due to their larger size, only two PMs are accomodated in each side of the counter.
- The light guide is designed so as it can be tilted to various directions. The light is guided independently to each PM on one side.
- Due to mechanical constraints, some of the counters have a clear plastic extension between the scintillator and the light guides.

A picture of one module is shown in Figure 86a. A photograph of sample light guides after tilting is shown in Figure 86b.

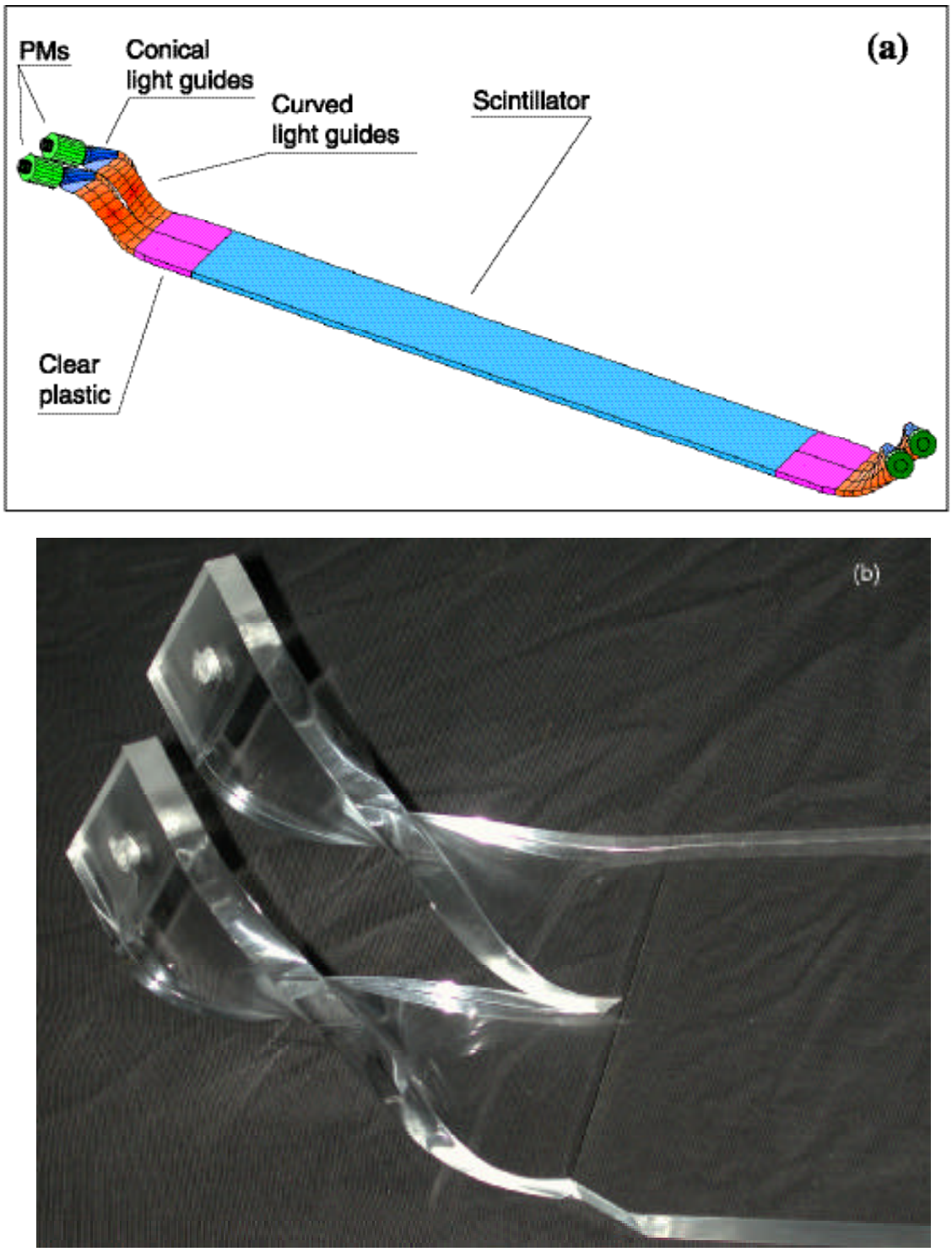

Figure 86: ***(a)*** **General TOF counter design. The configuration of the light guides and the dimension of the clear plastic section are different for counters in different positions.** ***(b)*** **Photograph of sample light guide after tilting. The straight section on top of the guide has a hole to hold it during tilting and will be cut away before mounting**

(v) TOF plane design

Each TOF plane consists of 12 counters, 12 cm wide. Figure 87 shows the design of planes 1 and 2 of the TOF system. The PM orientation with respect to the magnetic field and the field magnitude are shown in Figure 88 for all PMs of the system. Most of the PMs are in a region ($B<3000$ G, $\theta < 35°$) where the influence of the magnetic field is negligible.

The counters are attached to a honeycomb plate which is connected to the AMS-02 unique support structure (USS).

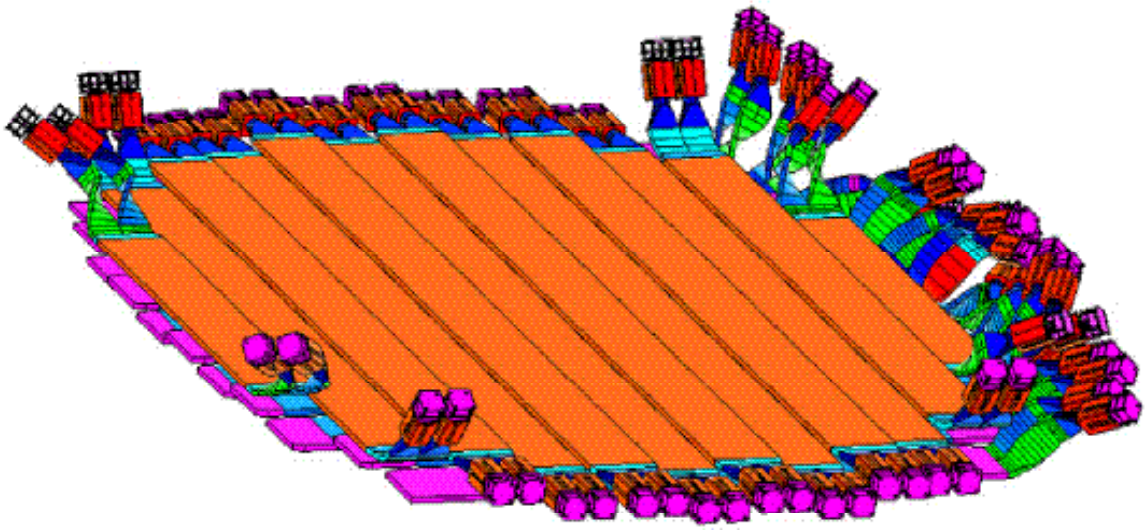

Figure 87: Sketch showing the positioning of the counters and of the PMs in planes 1 and 2 of the TOF system. Note that the PMs of plane 1 are shown on one side only.

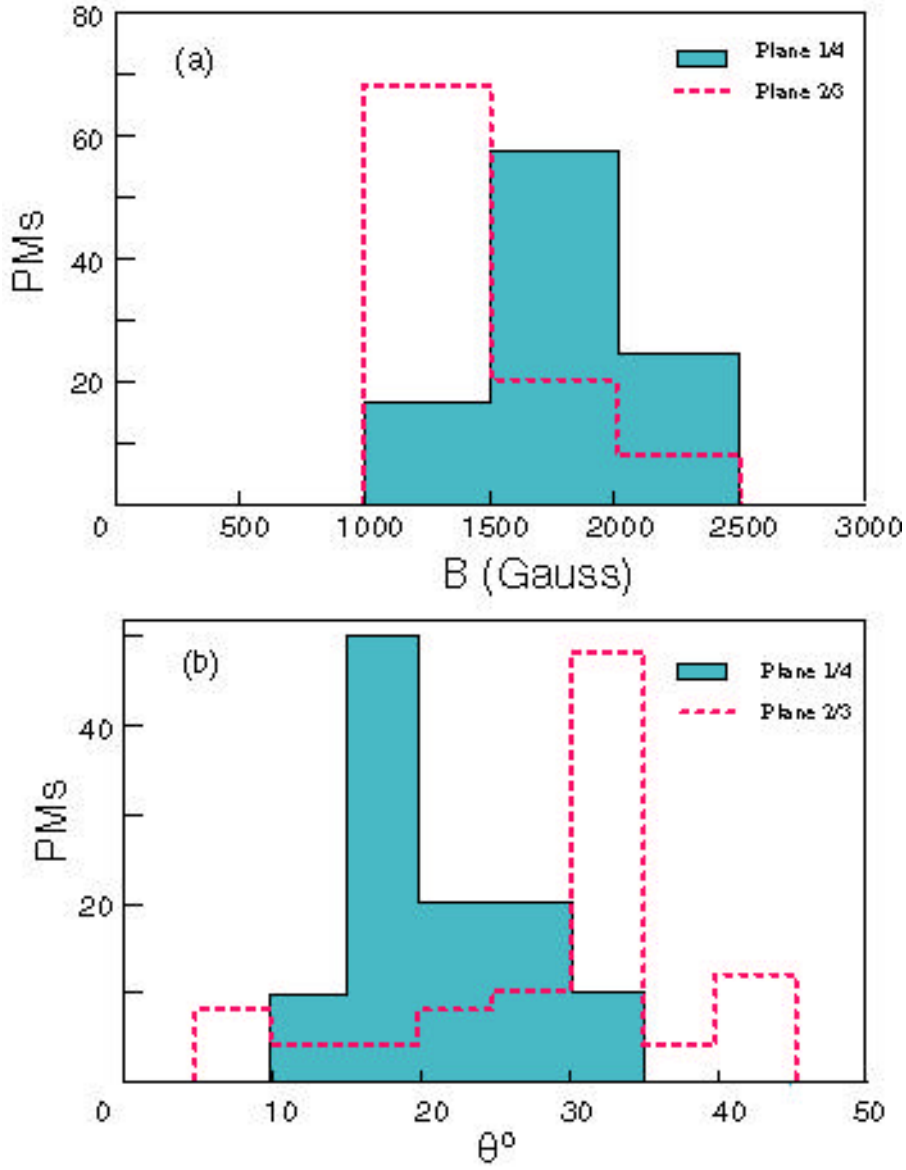

Figure 88: ***(a)*** **Magnetic field and** ***(b)*** **angle between the PM axis and the magnetic field direction for PMs on planes 1 and 4 (full line) and planes 2 and 3 (dashed line), respectively.**

3) Electronics

The characteristics for the TOF electronics are:

- redundancy;
- complete control on every channel for fine tuning during 3 years of data taking;
- low power consumption (150 W), i.e. high efficiency both for power conversion (up to 2400 V) and for read-out.

There are 192 PMs in total. The signals from the two PMs on each side of the scintillator paddle will be summed to provide one signal from the anodes and one from the 3rd last dynodes. The anode signal will be used for time measurement, while the dynode signal will be used for charge measurement using linear ADCs.

The TOF electronics will be housed in two pairs of crates (known as S-crates) (see Figure 89), each pair servicing one pair of planes and containing the PM power supplies and the read-out electronics. Part of the electronics will be positioned near to the counters (see Figure 90) to minimize the high voltage cable length.

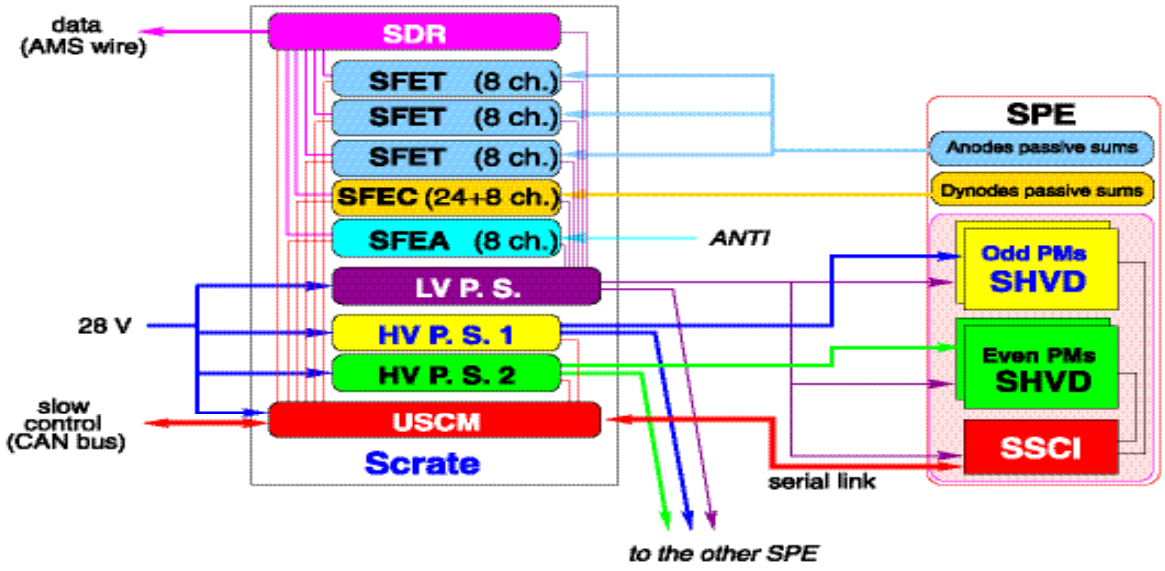

Figure 89: TOF electronics crate (S crate). SDR=Scintillator Data Reduction; SFET=Scintillator Front-End Time; SFEC=Scintillator Front-End Charge.

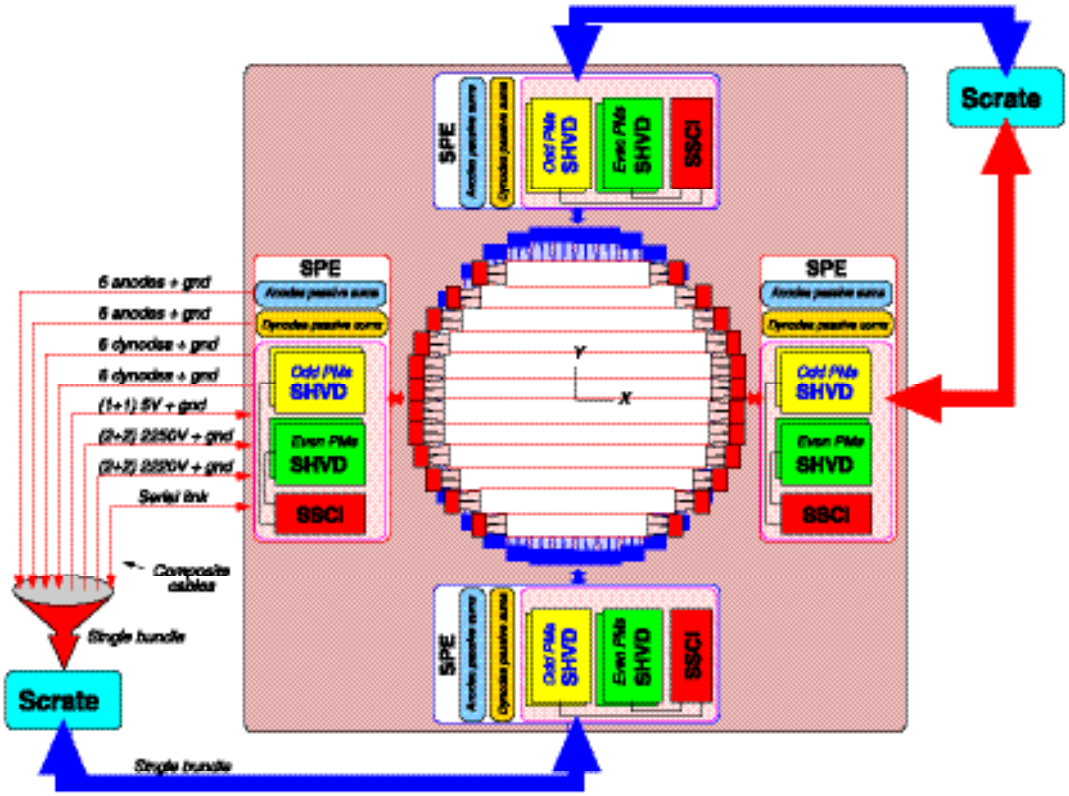

Figure 90: The TOF peripheral electronics. SPE = Scintillator Peripheral Electronics; SHVD = Scintillator High Voltage Distributor; SSCI = Scintillator Slow Control Interface

(i) Voltage dividers

In order to reduce power consumption, the voltage divider of the TOF PMs will have a total impedence of 80 MΩ. The measured maximum rate with AMS-01 was 10 kHz, much larger than the expected trigger rate (between 200 Hz and 2000 Hz).

The validity of this choice is confirmed by the good behavior of the TOF system of AMS-01, which was able to keep a 99.98% trigger efficiency over all geomagnetic coordinates (with the exception of the South Atlantic Anomaly).

(ii) PM power supplies

As seen from Figure 90, the 24 PMs on the same side of a plane will be connected to 2 power supplies (via SHVD), one for the 12 "odd" PMs, the other for the 12 "even" PMs, to increase redundancy. Moreover, each power supply will have two sides, one "hot" and one "cold", which will only be powered in case of failure of the "hot" side. The HV from the power supply will be distributed to 12 regulators, sitting near to the counters, with a current limiter as protection against short circuits.

(iii) Read-out

As seen from Figure 89, each electronics crate will house:

- one *Scintillator Data Reduction* (SDR) board collecting data from three *Scintillator Front-End Time* (SFET) measurement boards reading 8 TOF channels each;
- one *Scintillator Front-End Charge* (SFEC) measurement board connected to 24 TOF channels and 8 anticoincidence channels;
- one *Scintillator Front-End Anticoincidence* (SFEA) board reading 8 anticoincidence channels.

Each board will be doubly redundant with "hot" and "cold" sides.

(iv) Slow control

As shown from Figure 89 the slow control functions of the TOF system will be executed by two boards :

- The *Universal Slow Control Module* (USCM) will control all the electronic boards and will be connected to 2 *Scintillator Slow Control Interface* (SSCI) units placed near the PMs through serial links. The SSCI board will be responsible for setting and reading the HV of a plane side.

The temperature of the TOF system will be read by the USCM. USCM will also turn on and off each board in the crate, selecting the "hot" or "cold" sides.

4) Test results

In order to determine the effectiveness of the new PMs and of the new light guide design, the time resolution of two counters equipped with Hamamatsu R5946 PMs and with different light guide design have been measured using minimum ionizing particles selected with a cosmic ray telescope.

Figure 91 shows the time resolution as a function of the position along the counter for straight light guides and for light guides tilted at 90° with respect to the counter plane. The resolution for straight guides is similar to what was obtained with the AMS-01 counters. The observed worsening of resolution for tilted guides indicates that about half of the photoelectrons are lost due to the geometry.

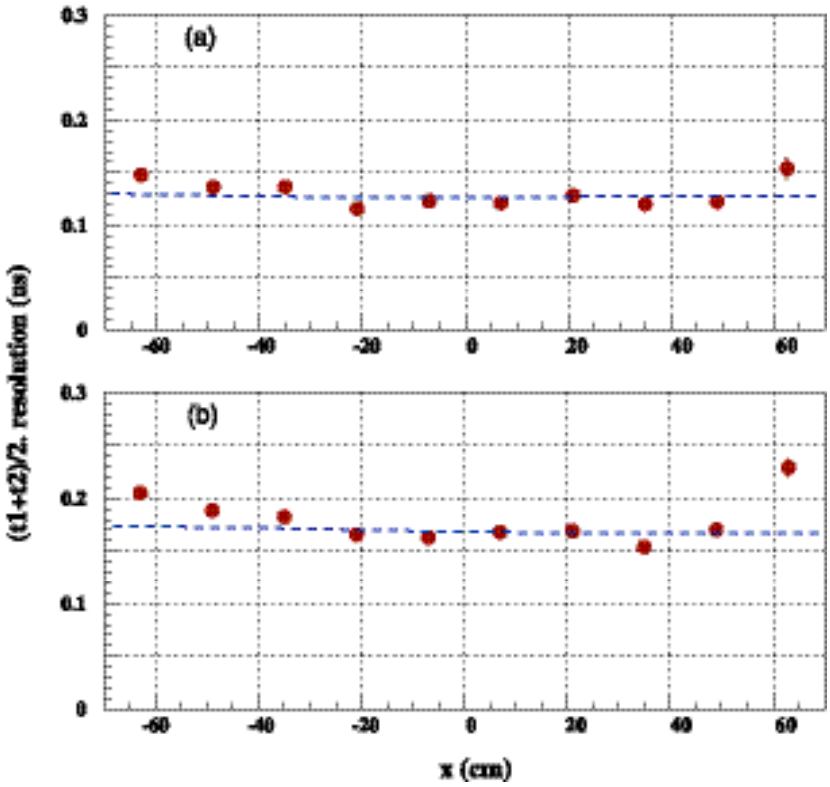

Figure 91: Results of the tests with the new R5946 PMs: time resolution as a function of the position along the counter for straight light guides *(a)* and curved light guides *(b)*.

5) Conclusions

Based on the test results, the AMS-02 TOF system is expected to have a slightly worse time resolution then in AMS-01, due to the tilted light guides and to the effect of the magnetic field. In particular, some of the PMs will have an angle with respect to the magnetic field direction greater than 30°. Figure 92 shows the expected resolution in β as a function of the time resolution of the TOF system. The main TOF purpose of fast trigger, rejection of upward particles and dE/dX will be comfortably achieved.

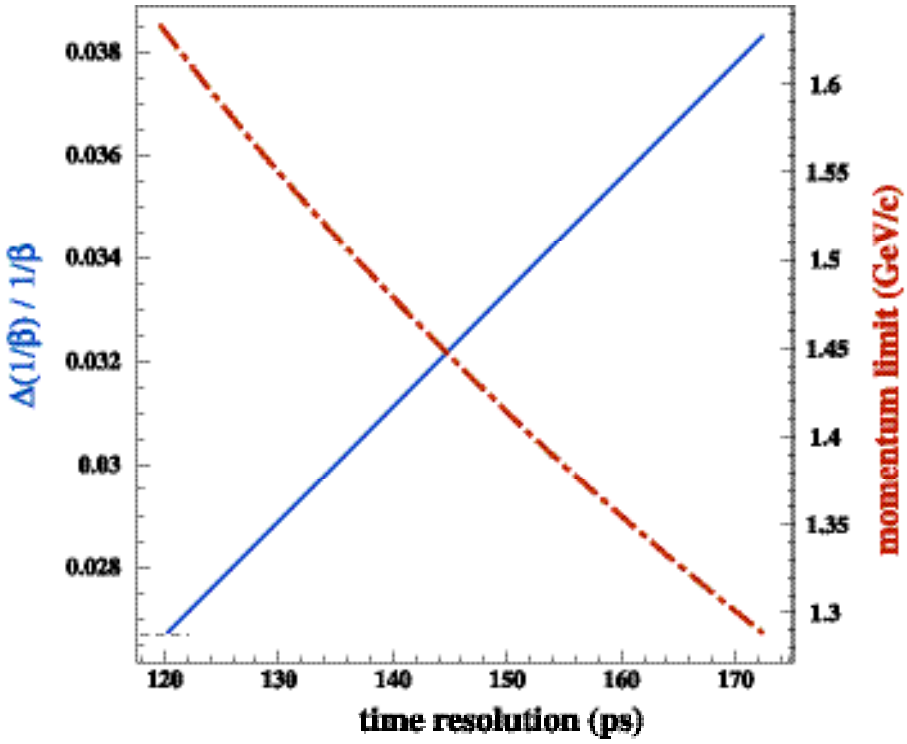

Figure 92: Expected resolution in 1/β (full line - left scale) and standalone momentum limit for positron identification (dashed-dotted line - right scale) as a function of the TOF system resolution.

V. The Anti Coincidence Counter System (ACC).

1. General Description of the ACC-System

The Anti Coincidence Counters (ACC) form a barrel around the central Tracker of the AMS experiment (figure 93). Its purpose is to detect charged particles which penetrate the AMS detector from the side. If such an event coincides with a good track which was triggered by the Time of Flight system (TOF) the measurement of the good track is disturbed. Another disturbance are multi track events which are produced when a high energetic particle which is triggered by the TOF system creates δ electrons or even a shower on its passage through the AMS detector (LEPS, TRD, TOF).

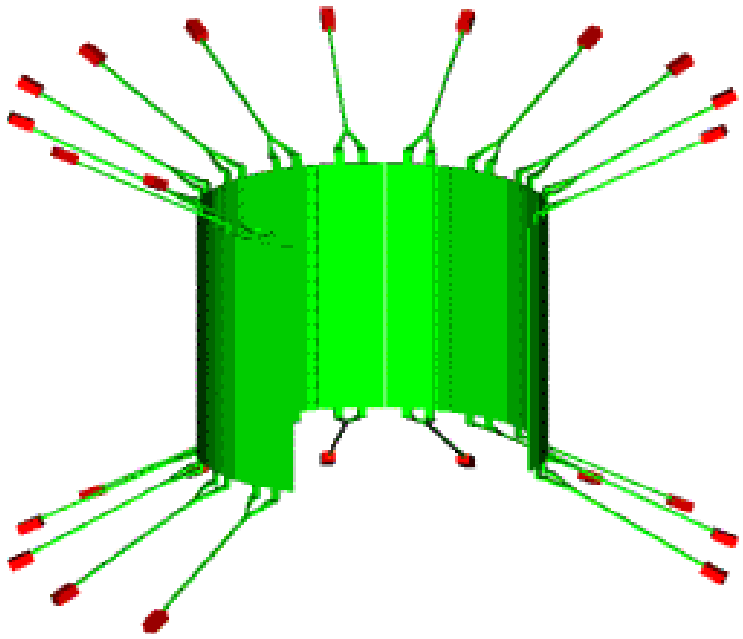

Figure 93: Three-dimensional sketch of the ACC-System

The ACC modules are made of scintillating material BC414 (manufactured by BICRON) which predominately emits light with a wavelength between 380 and 420 nm.

Due to the much larger AMS-02 magnet and the conical shape of the vacuum case the PMTs have to be placed at a larger radius on the flange. To prevent light loss caused by

absorption in the wave length shifting fibres the longer distance to the PMTs (1-2m) is bridged by glass fibres.

2. Geometry of the ACC-System

The ACC module design is shown in Figure 94. As the inner dimensions of the super-conducting magnet of the AMS-02 experiment are the same as those of the permanent magnet of the AMS-01 detector, the same scintillator modules will be used. 16 scintillator modules with a height of 832 mm form a cylinder with an inner diameter of 1091 mm. The scintillating material is 10 mm thick, the wrapping ≈ 0.3 mm. The 16 modules are mounted by means of grooves and ribs on their long edges on the inner surface of the magnet vacuum case. They are further stabilized on their inner side by a reinforcement cylinder of an outer diameter of 1087 mm with a wall thickness of 1 mm and a length of 850 mm. Both the 16 modules and the reinforcement cylinder are supported by clamps and spring elements to the vacuum case allowing for different thermal expansion coefficents and resulting in a first eigenfrequency of the whole system of 50 Hz.

On the outer surface of each module two times 37 grooves (1.5 mm deep, 1.0 mm wide with a spacing of 2.9 mm) are milled from top to bottom in which the fibres (1 mm) are glued in. The fibres are combined in two bundles on each side of the ACC modules. The two bundles, which run through light tight Viton tubes, end in a coupling connector where the light is transmitted to glass fibres of the same diameter. The length of these light guide bundles will be in the range of 1 to 2 meters, the diameter about 10 mm.

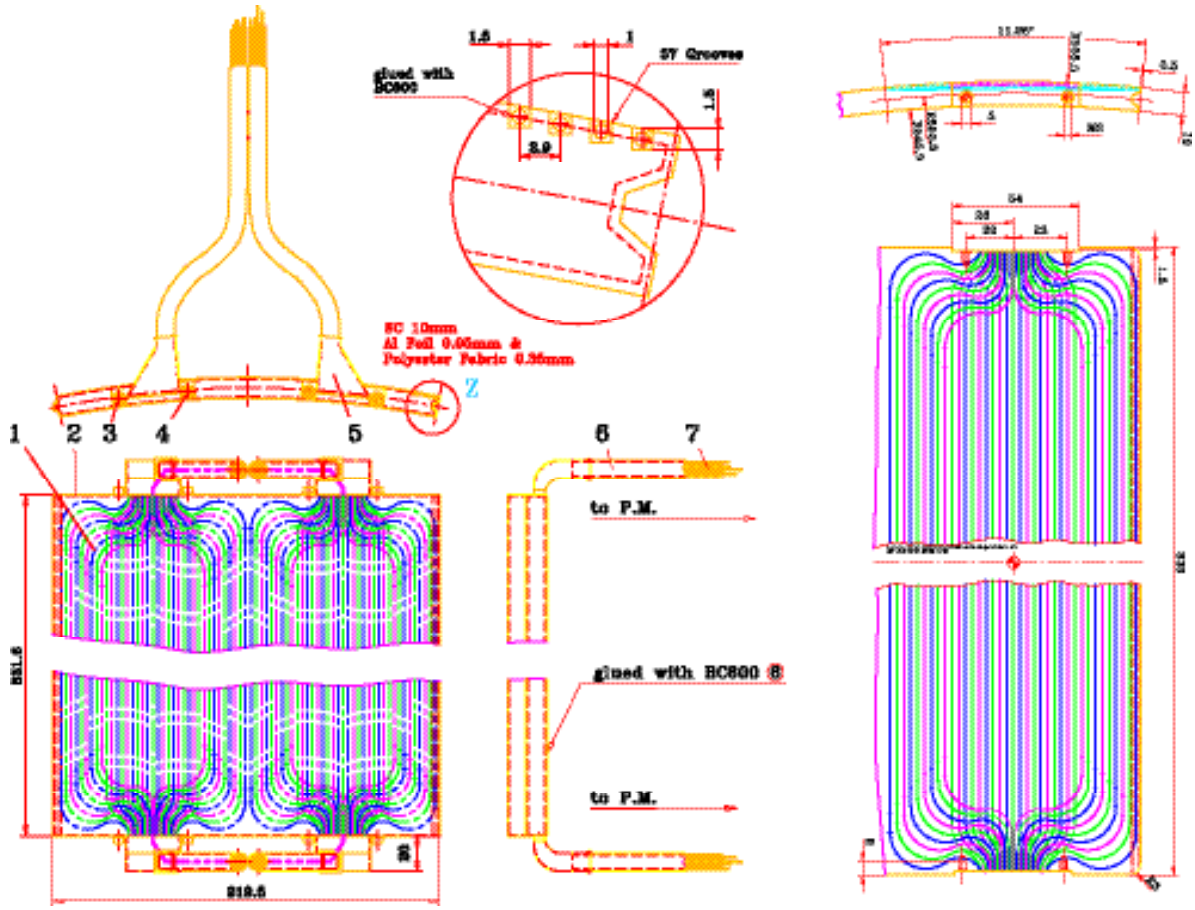

Figure 94: Dimensions of an ACC Module.

Photo-multiplier Tubes

Calculations of the magnetic field at the positions of the PMTs in the AMS-02 experiment (Figure 95) result in a much higher field ≈ 0.16 T. Therefore the same Hamamatsu R5946 PMTs as for the TOF will be used.

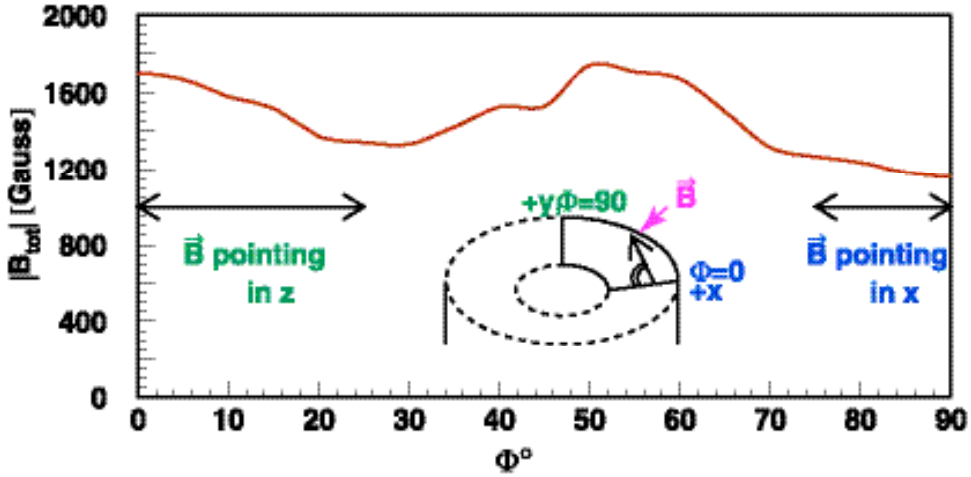

Figure 95: Calculated strength and direction of the magnetic field at the positions of the PMTs.

In the *+y / -y* region, i. e. 70° < φ < 110° and 250°< φ < 290°, the magnetic field vector points in the *x* direction. Therefore we will group all PMTs in this region and orient their axis in the *x* direction (figure 96).

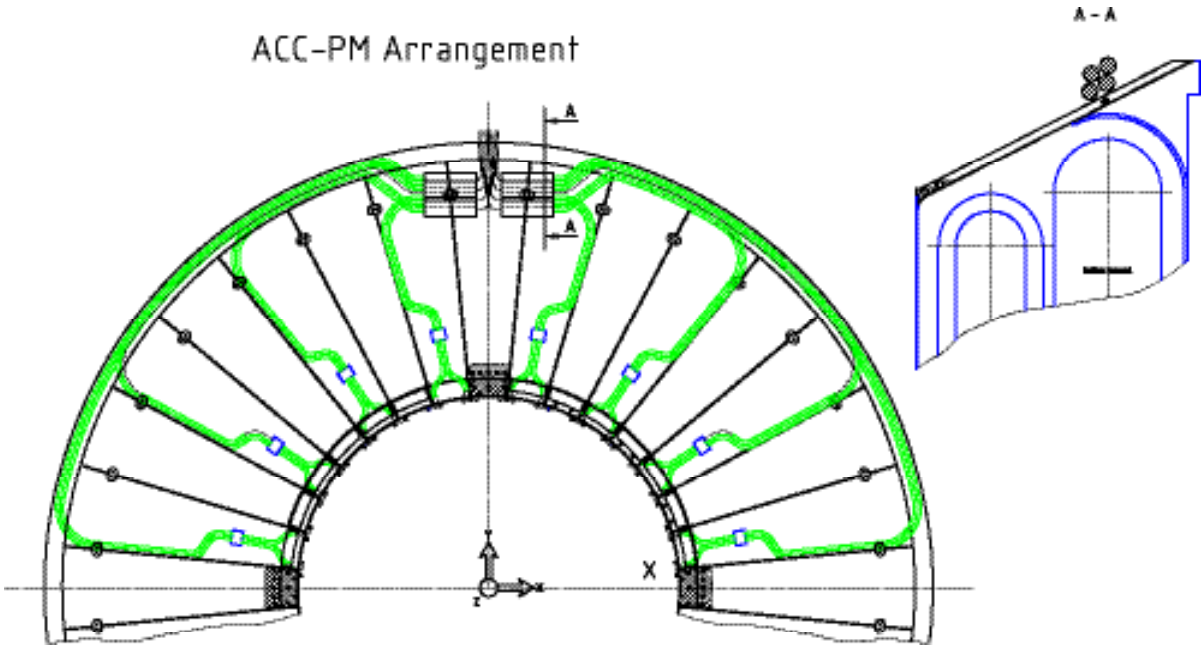

Figure 96: Schematic view of the PMT positioning on the magnet flange.

3) Electronics and Trigger

The HV supply and the read out of the 32 PMT signals of the ACC modules are designed similar to those of the TOF system.

The signals of the ACC counter PMTs (anode) are processed in the same way as the TOF signals by the front end electronic boards in the S-crates. The front-end electronics provide signals with a length of 50-100 ns to the AMS-02 trigger system to look for coincidences with TOF signals.

Information from the ACC can not be used in the Fast Trigger, due to the back-splash of the EMC. If a high energy deposit is measured in the EMC, the veto signal from the ACC must be ignored. Therefore the information from the ACC and the EMC must be combined in the level-1 trigger.

VI. The Ring Image Cerenkov Detector (RICH)

1) Introduction

Precise mass determination is important in the search for antimatter and the measurement of relative abundances of light isotopes. In particular to obtain a $\overline{He}$ / He background rejection ratio of $1 / 10^{10}$ the identification of $\overline{He}$ requires multiple redundancies: multiple measurements of dE/dX from TOF and Tracker to determine Z^2 and multiple measurements of the trajectory from the AMS tracker to determine the sign of Z. In addition the precision measurement of velocity provides a redundancy to determine the particle mass.

As seen in Figure 3 in the AMS spectrometer, the momentum is determined with the precision of 1% up to 30 GeV. To measure the velocity with an accuracy of about 1 per mil will provide an excellent mass determination.

Figure 97 shows the Monte Carlo study of isotope separation with AMS-02 spectrometer with RICH providing a velocity resolution of 0.1%

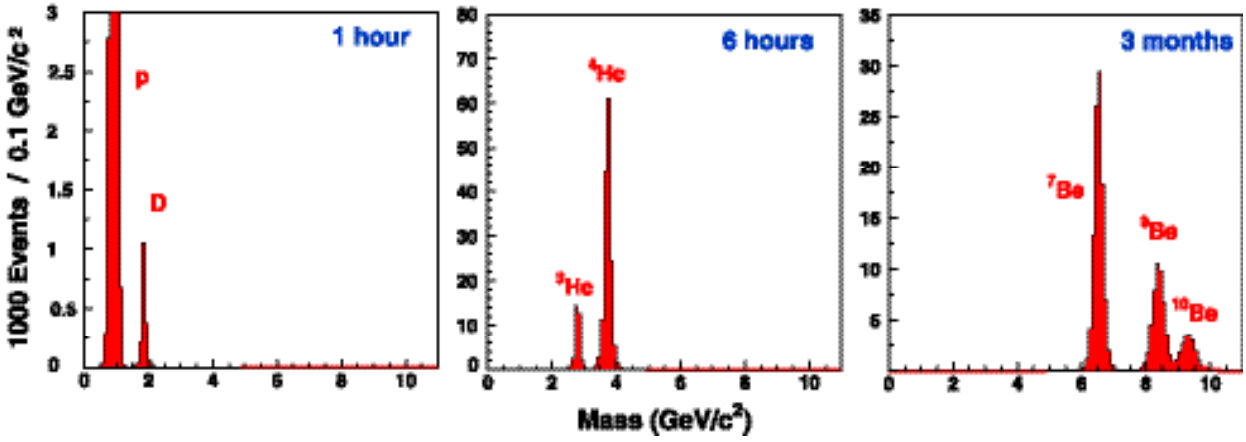

Figure 97: The AMS RICH light Isotopes yields for different collection time on ISS expected from the Monte-Carlo studies with E_{kin} < 10 GeV/N.

In addition to the experience of the successful AMS-01 Aerogel Counter, before the final design of the RICH, we have spent two years of R&D to master the techniques of building reliable

RICH to be used in space. We have also performed many beam tests on various designs and choices of radiators for the RICH. Figure 98 shows the results of one of the very early tests of a RICH equiped with NaF radiators in GSI Germany.

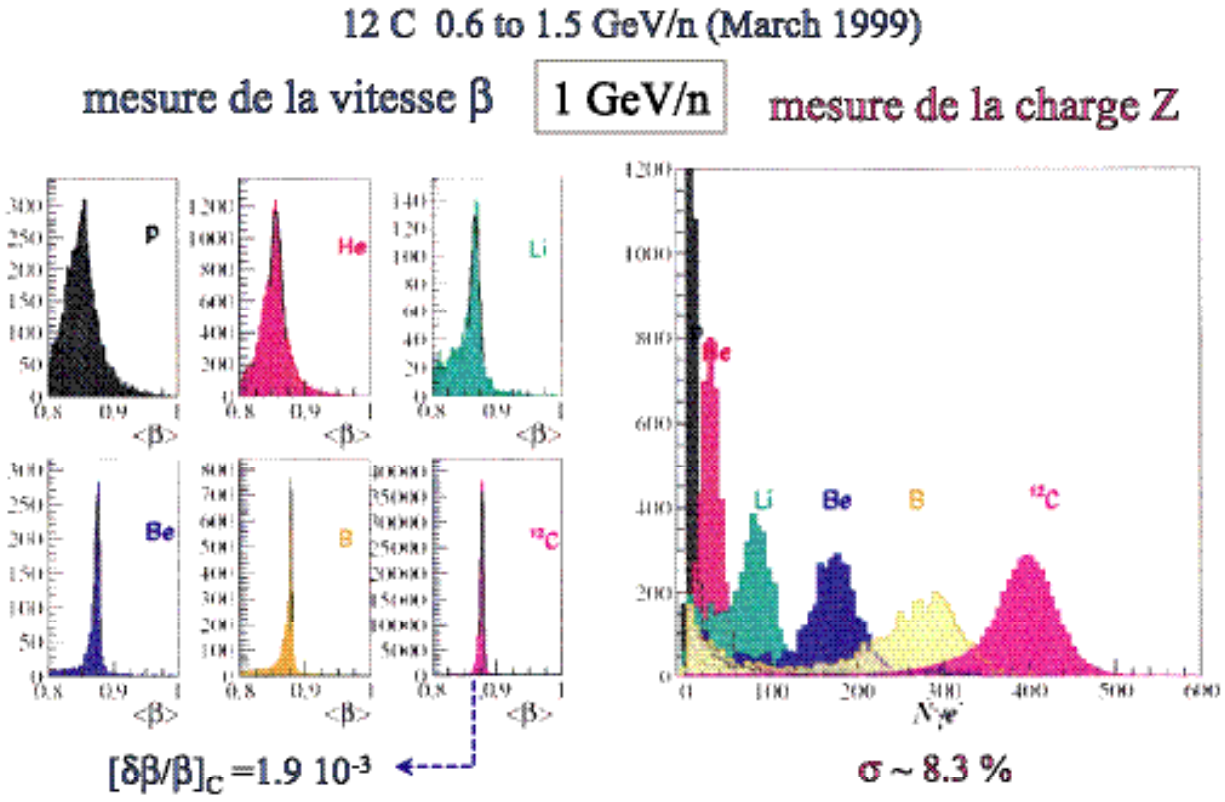

Figure 98: Test results with an earlier version of RICH using NaF (n=1.35) as radiator.

The AMS RICH is being constructed by an international collaboration coordinated by G. Laurenti of INFN Bologna, together with C. Maña of CIEMAT, Madrid, G. Barreira, Lisbon, and M. Buenerd of ISN Grenoble. In addition P. Fisher of MIT participated in the conceptual design work.

The location of RICH is shown in Figure 2. The RICH (Figure 99) has a truncated conical shape with 60 cm upper radius, 70 cm lower radius, a height of 60 cm and two supporting plates on the top and the bottom. The upper plane holds a 2 cm thick layer of radiator. The lower plane, which has a 63 x 63 cm^2 squared central hole to let particles pass unaffected to the Electromagnetic Calorimeter, supports an array of 1000 light guides and photomultipliers with front end electronics.

When an incoming charged particle passes the radiator, most of the Cerenkov radiation goes directly through the light guides to the photomultipliers. The remaining photons are reflected by the inner surface of the reflector cone to the photomultiplier. From the spatial coordinates of the photomultiplier pixels and the direction of the incoming particle, the Cerenkov angle is reconstructed and the velocity of the particle determined.

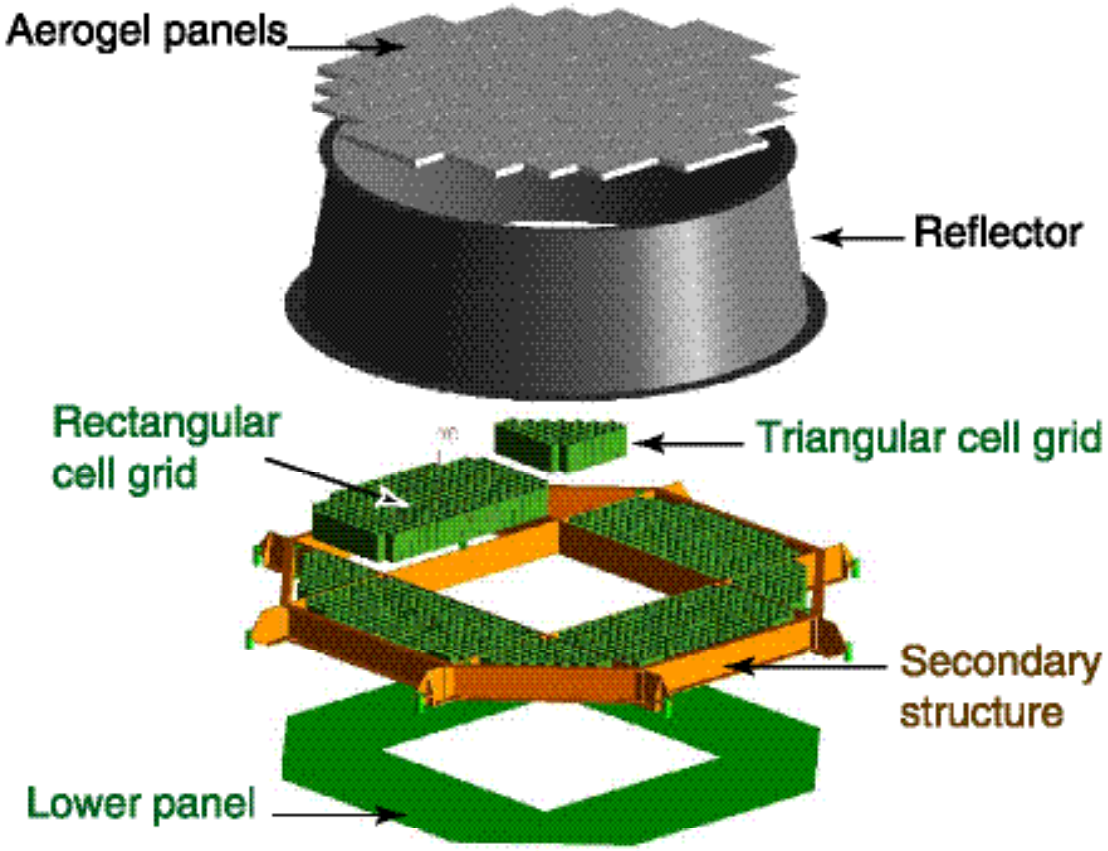

Figure 99: RICH with the main structural components.

2) The Radiator

The performance of many dielectric materials has been studied with a Monte Carlo simulation. For the most promising ones, tests have been performed with nuclei beams (He and C) at GSI (Darmstadt) and Cosmic Rays at ISN (Grenoble). The material which has shown best performances is the aerogel which we have used successfully on AMS-01. The aerogel refraction index (n) has a linear dependence with the density (ρ) given by:

$$n = 1 + 0.25\ \rho\ (g\ cm^{-3})$$

With treatment, aerogel densities can be selected in the range of 0.1 to 0.3 g cm^{-3} and, therefore, a variety of refractive indices are available. According to Monte Carlo simulations and the tests performed on different samples with cosmic rays, we have chosen the Aerogel produced by Matsushita Electric Works Ltd. which has *n* between 1.03 and 1.05.

The mechanical structure of the radiator consists of 121 rectangular blocks of aerogel of 11x11x2 cm^3 (Figure 99). The array of blocks is supported from the bottom by a 1 mm thickness layer of methacrylate with no UV absorbing additives.

3) The Photon detection system

The magnetic field in the region where the photomultipliers are placed is 300 G. The photomultipliers have to be protected by a shielding case. To collect the Cerenkov photons, a light collecting system has been designed. The main components are shown in Figure 100.

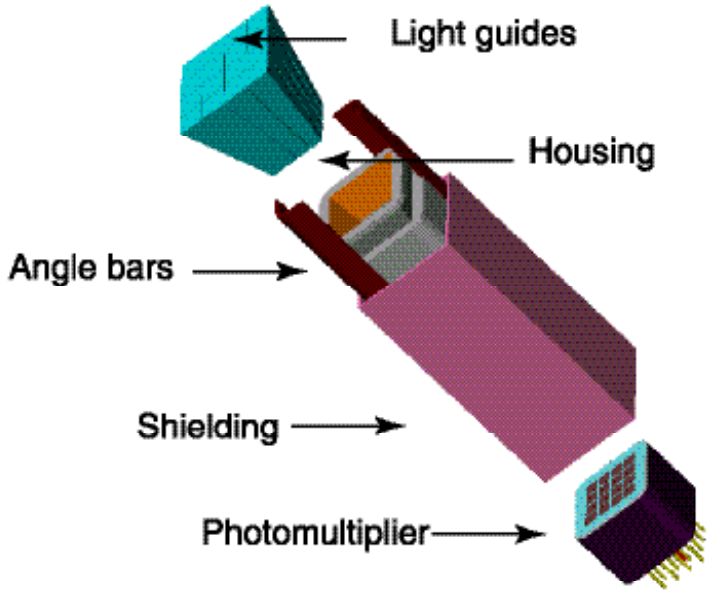

Figure 100: ThePhoton Detection System with the main components.

As seen from Figure 100 the photon detection system has 4 major components:

(i) The Photomultipliers (PMT)

PMTs from different manufacturers have been studied. The HAMAMATSU R7600-00-M16 were chosen due to their small size, fast response under low operational voltage (800 V), large anode uniformity (shown in Figure 101) and insensitivity to external magnetic fields.

The Cerenkov photons are detected on the image plane at 40 cm from the radiator material. Therefore, the accuracy in the measurement of the velocity depends significantly on the size of the photon sensors. These photomultipliers have a 4x4 multi-anode structure, each anode with a sensitive zone of 4x4 mm^2. This ensures a resolution in the measurement of the velocity of 0.1%. The PMTs have a high quantum efficiency ($\varepsilon \approx 20\%$) in a range of wave-lengths between 300 and 600 nm, well within the optical region of the radiator. This efficiency determines that, for an ultrarelativistic particle of charge Z=1, an average of 10 photons are detected for a radiator with n=1.05 refractive index.

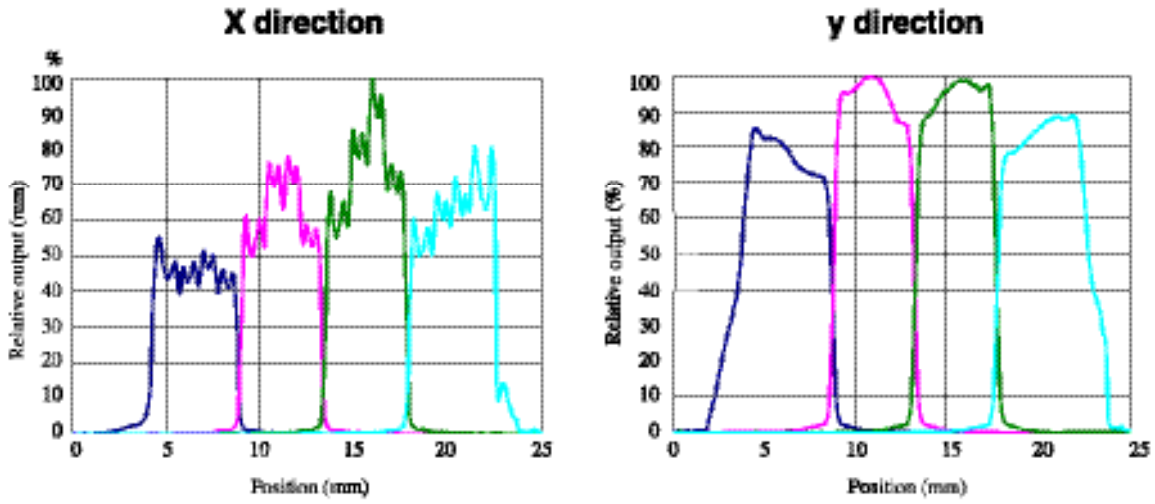

Figure 101: Anode uniformity of a row of 4 pixels along the x and y directions.

(ii) The Magnetic Shielding

Each photomultiplier, together with the front end electronic boards, is placed inside a VACOFLUX 50 cell whose dimensions are larger that those of the photomultiplier to avoid boundary effects. Due to the geometry of the array of photomultipliers, several cells are assembled

forming up a grid with two different geometries: square (with 104 cells) and triangular (with 42 cells). A square grid is shown in Figure 102.

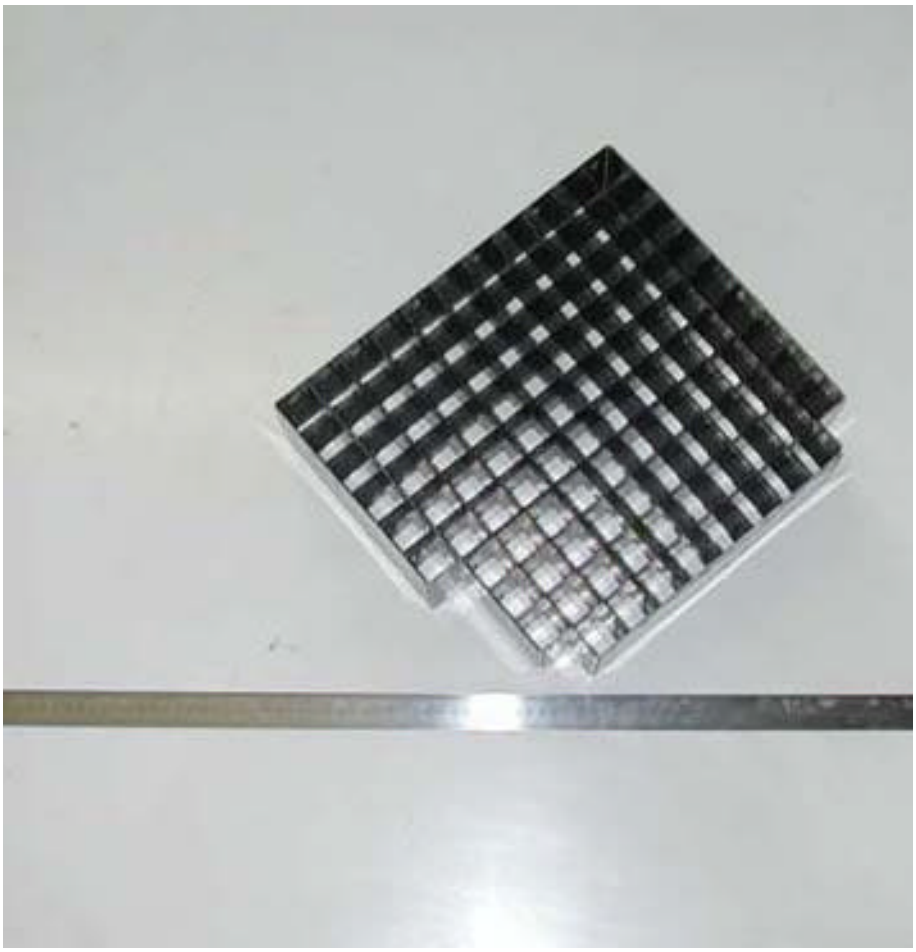

Figure 102: Square grid structure with 104 cells.

The grids are supported by a structure of aluminum beams which holds also the frustum of the conical reflector. The elements of the grid are grouped together by spot welding. The VACOFLUX 50 has to undergo an annealing treatment to obtain the desired magnetic properties. This thermal treatment modifies the crystalline structure of the material and therefore its mechanical properties. Thus, a series of mechanical measurements have been performed to measure the properties of the material after welding, annealing and final assembly. Each cell has two angle bars in the corners to reinforce the mechanical strength of the grid and to conduct the heat flow from the cells to the thermal radiators. Prototypes have been tested to optimize the welding procedure.

(iii) The Housing

The interface between the photomultipliers and the walls of the shielding grid is a polycarbonate box (housing) which contains also the front-end electronic boards. The housing has been designed to ensure the tolerances on the relative positions of the photomultipliers and the light guides within the shielding cells.

(iv) The Light Guides

In order to construct an efficient light guides system, different options have been analyzed: fiber optic cables, hollow light guides with reflecting inner surfaces and solid light guides working by internal reflection. Detailed Monte Carlo simulations have shown that the solid light guides are the most efficient. However, the optical and mechanical properties of the solid light guides are crucial for the good performance of the light collecting system. The photomultiplier response has a high quantum efficiency for wave-lengths between 300 and 600 nm. Therefore, we require a high transmittance over this wave length region, in particular materials with no UV absorbing additives. The light guide refractive index should be near to that of the photomultiplier window (n=1.5), its density has to be low to minimize the weight and the thermal expansion coefficient should be small to stand temperature gradients. Further, in order to reduce significantly the losses due to different optical interfaces, a thin film (1 mm) of optical contact is deposited between the bottom of the light guides and the photomutiplier window. Different organic materials have been tested for the light guides BC-800 from BICRON has been chosen. The measured transmittance for a 12.7 mm thickness layer is shown in Figure 103 together with the one corresponding to a 3 mm thickness layer of optical contact.

Since each photomultiplier has 4x4 pixels, each light guide structure has 16 independent units with 4 different geometries and a total volume of ≈ 13 cm^3. The optimum dimensions have been determined to maximize the photon collection efficiency (shown in Figure 104). A Monte Carlo simulation has shown that, with this design, enough Cerenkov photons are collected to achieve a resolution in the velocity of single charged particles of $\sigma_\beta/\beta \approx 10^{-3}$.

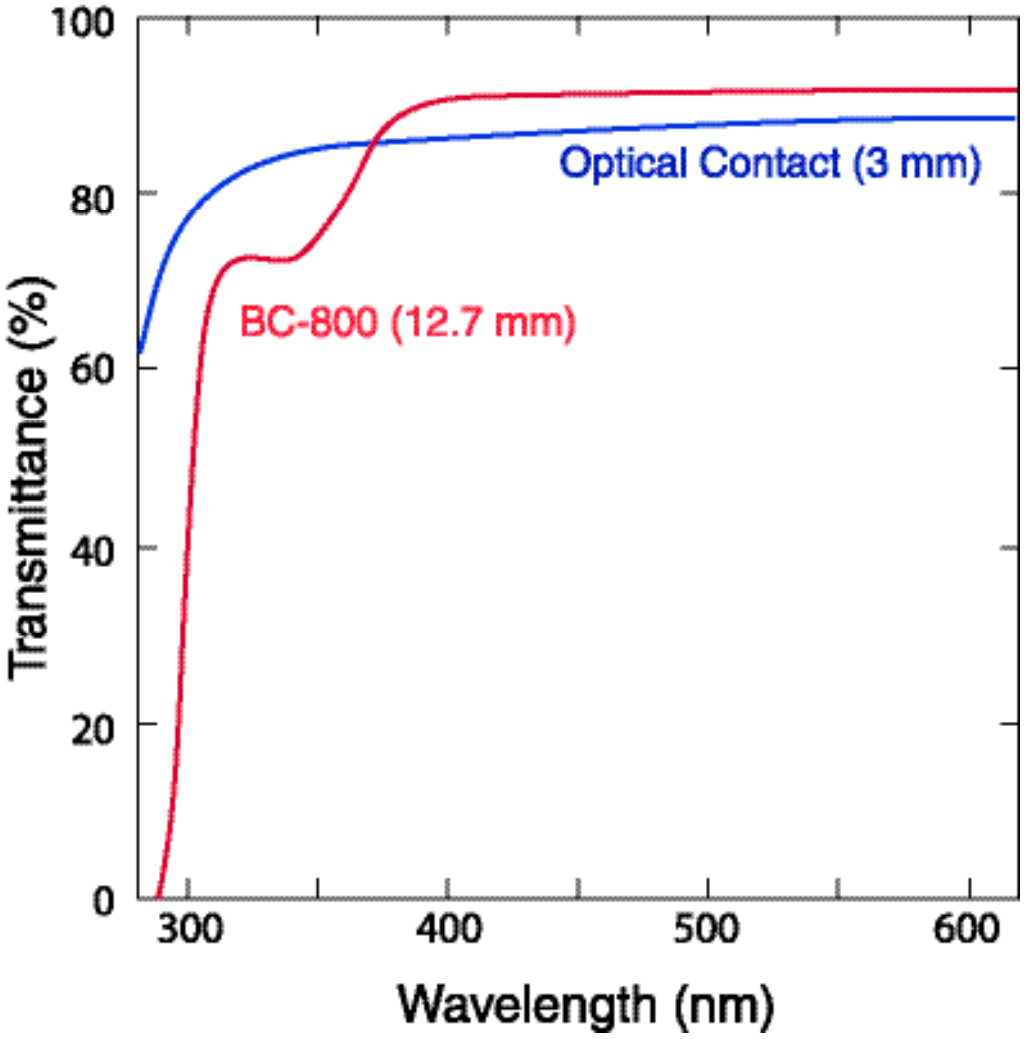

Figure 103: Measured transmittances of a 12.7 mm thickness layer of BC-800 (ρ = 1.19 g cm^{-3}, Softening point = 96°C, n = 1.49, Coefficient of thermal expansion =0.0074%/°C) and 3 mm thickness layer of optical contact.

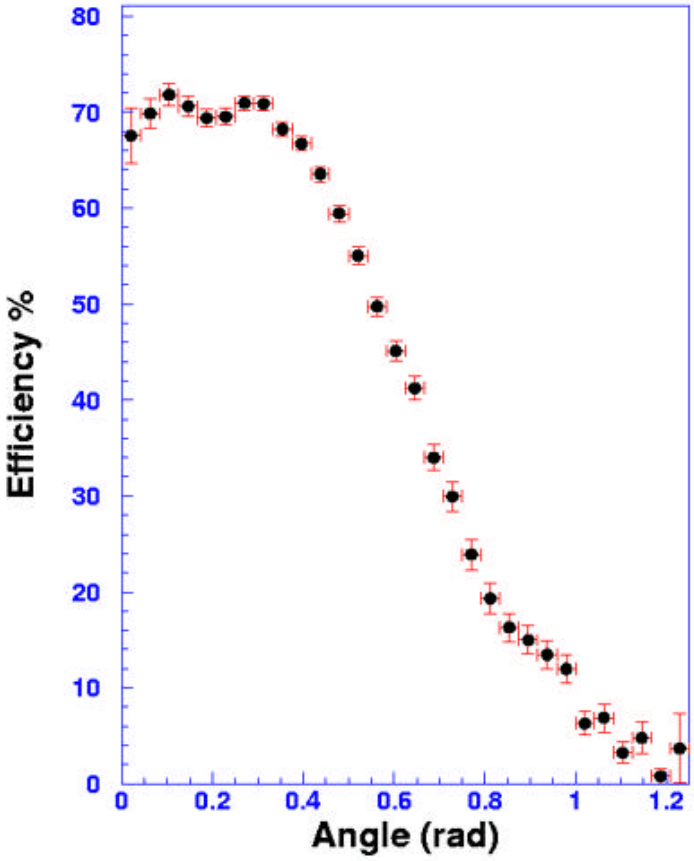

Figure 104: Average photon collection efficiency for a full structure of 4x4 light guides as function of the photon angle of incidence.

4. The Reflector

About 30% of the Cerenkov photons intersect the inner surface of the conical shell. A reflector (see Figure 105) has been designed to reflect those photons to the photomultipliers. It consists of a supporting structure with a truncated conical shape of 1340 ± 0.2 mm and 1140 ± 0.2 mm diameter for the lower and upper sections and a thin film of reflective coating deposited on the inner surface. In order to have a 0.1% resolution in the velocity, stringent requirements on the tolerances are necessary as shown in Table 13.

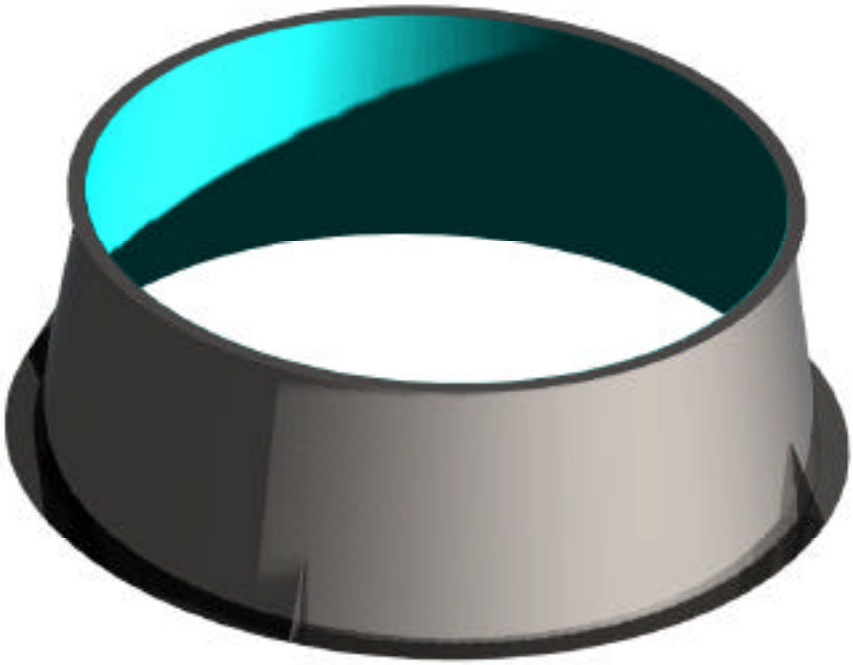

Figure 105: The reflector of the Cerenkov detector.

Conicity	200 μm
Centering	100 μm
Reflectivity	≥ 90 % (for λ = 420 nm)
Roughness	≤ 150 nm
Slope error	< 1 mrad

Table 13: Parameters and designed tolerances for the reflector.

Several options have been studied:

a) Nickel based structures have been successfully used for earth-based X-Ray telescopes and space telescopes but are very heavy and have been discarded.

b) A composite material (carbon fibers or graphite reinforced fibers). A model of carbon fiber reinforced material (CFRC) with a steel plate die of 30 nm roughness was built. Keeping the

overall roughness within the specified tolerance of 150 nm, the measured reflectivity was in the range of 50 to 70% (depending on the wave length and on the incidence angle). The test has shown that, for composite materials, the roughness and reflectivity are not compatible with requirements.

c) A plasma-spray of aluminum and titanium oxide (Al_2O_3/TiO_2). With the plasma-spray technique, alumina is sprayed on a mandrel by a plasma spray gun in similar way as was done for the CFRC option. Aluminum oxide (Al_2O_3) alloyed with titanium oxide (TiO_2) has good mechanical properties but shows also an intrinsic roughness. Thus, when it is sprayed on the mandrel, the structures on the surface get through the gold plate ruining the final surface. For this reason, an epoxy resin layer has be placed between the gold plate and the layer of alumina. In order to lower the density of the resin and to grant a better grasping of the alumina, a small amount of glass microspheres have been added to the resin. A model test in a reduced scale of 1:5 has been built (Figure 106). It has a cylindrical shape of 300 mm diameter, a height of 100 mm and is made out of the following layers:

    1. Alumina (1 mm);
    2. Epoxy resin (400 μm);
    3. Gold (0.2 μm);
    4. Chromium (150 μm);
    5. Aluminum (0.1 μm);
    6. Quartz (0.1 μm).

Two different tests have been performed with this model: a reflectivity test and an image quality test. The results of the reflectivity test, which measured the amount of reflected light, are shown in table 14. The measured values are close to the design goal and will improve with optimizing the thickness of the quartz and aluminum layers.

Figure 106: Cylindrical reflector model at scale 1:5.

Reference Mirror M90 (Optics National Institute – Italy)

Wavelength (nm)	Test model relative reflectivity	Reference absolute reflectivity	Test model absolute reflectivity
365	0.93 +/- 0.03	0.9118	0.85
420	0.95 +/- 0.01	0.8826	0.84
470	0.95 +/- 0.02	0.8484	0.81

Reference Mirror M10 (Optics National Institute – Italy)

Wavelength (nm)	Test model relative reflectivity	Reference absolute reflectivity	Test model absolute reflectivity
365	0.95 +/- 0.02	0.9025	0.86
420	0.96 +/- 0.01	0.8656	0.83
470	0.98 +/- 0.01	0.8290	0.81

Table 14: Results of the reflectivity test.

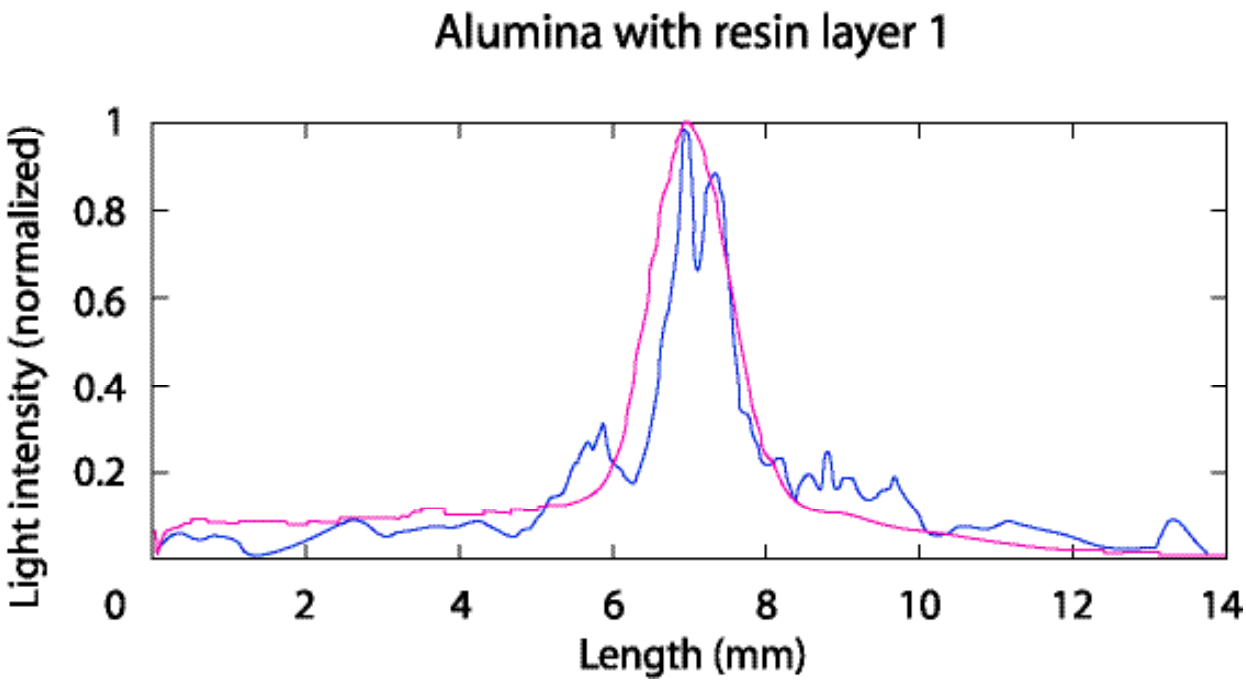

Figure 107: Results of the image quality test. The pink line shows the measured profile of the reference mirror and the blue one that of the model.

For the image quality test, a laser beam reflected by a reference mirror (with a roughness of 0.2 nm) has been compared with a laser beam reflected by the model. The reflected beam profiles are shown in Figure 107. There is a good agreement showing that the process is satisfactory.

The structural performances of the alumina supporting frame have been studied with the finite element model shown in Figure. 108. With a weight of 10.7 kg, a safety margin of 0.9 has been obtained.

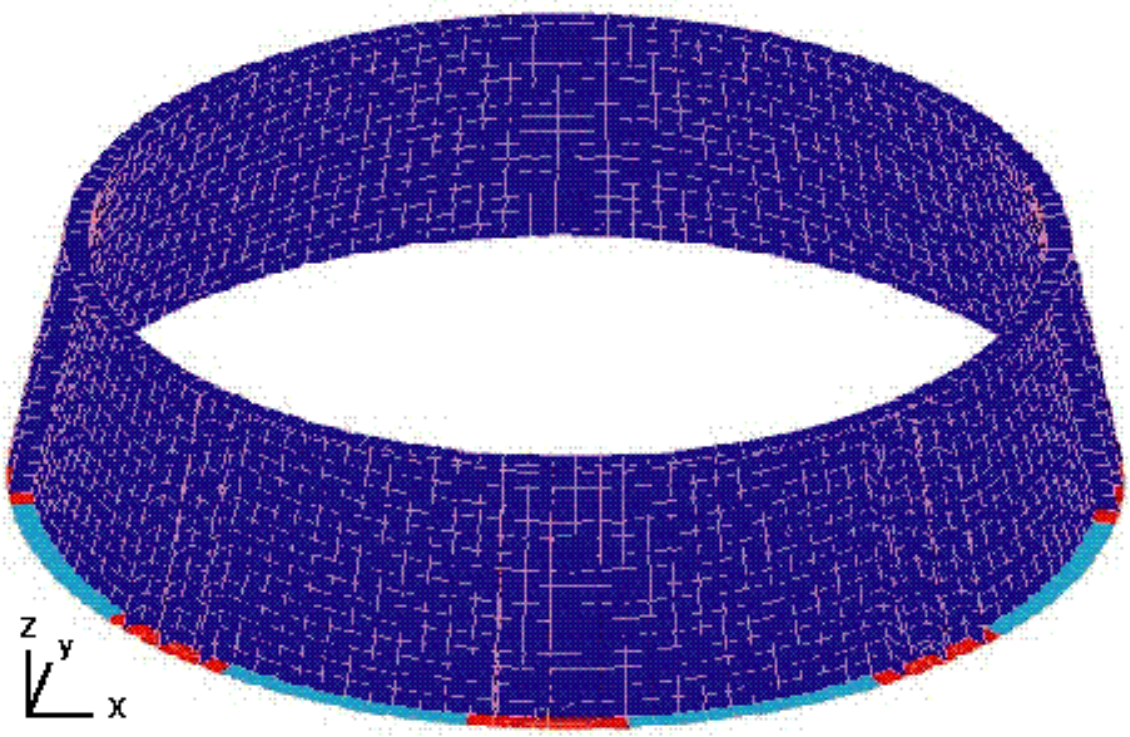

Figure 108: Finite element model of the reflector.

5. Stress and Modal Analysis

The RICH detector is supported by an aluminum alloy structure. In order to have the opportunity to remove each grid independently from the others, a modular solution has been chosen that gives also the possibility to achieve better dimensional tolerances.

The RICH structure must be stiff enough in order to support the detector grids and their content without inducing excessive deformations. In order to verify stresses, deformations and frequencies, a Finite Element Model (FEM) has been built (see following Figure 109).

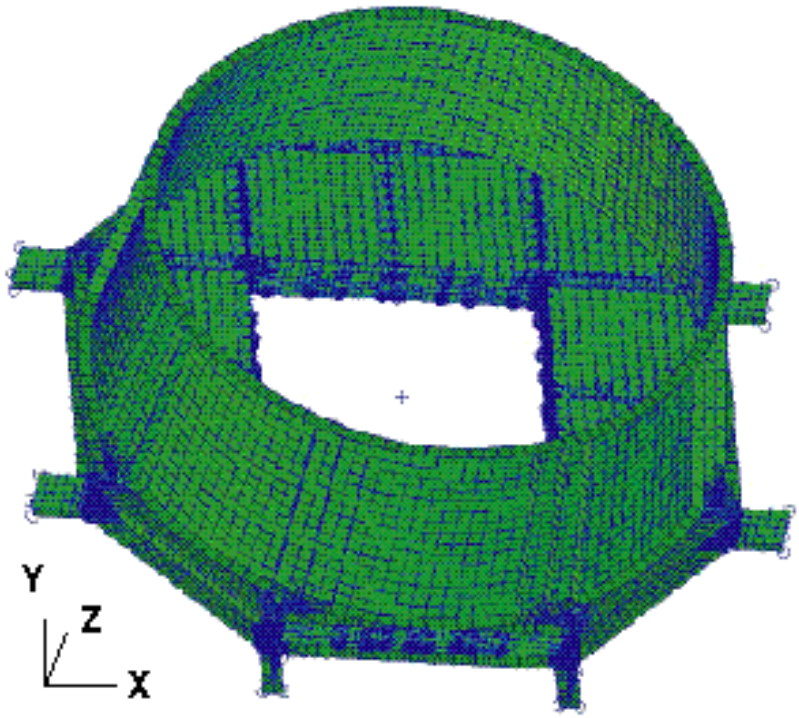

Figure 109: RICH structure finite elements model.

The F.E.M. model has been developed with a step approach studying the different structures making up the global model. The global model is made of shell elements with non-structural masses associated for some parts.

The steps of the analysis are the following:

- Secondary structure and joint system modeling with relative model correctness checks
- PMT modeling and joint system modeling with relative model correctness checks
- Reflector modeling and joint system modeling with relative model correctness checks
- Global model modal analysis with relative model correctness checks

A study has been performed on the secondary structure supporting PMTs cells and reflector frame. This step includes all secondary structure checks and modal analysis to verify the model validity.

The PMTs shell structure with associated electronic parts has been modeled and a study on the reflector frame has been carried out to ensure good local deformation and local yields. Several static analysis tests have been performed to understand which one could be the best reflector configuration; the result is a reflector with a reinforcing flanges. The following Figure 110 represents the yield values of the RICH reflector frame.

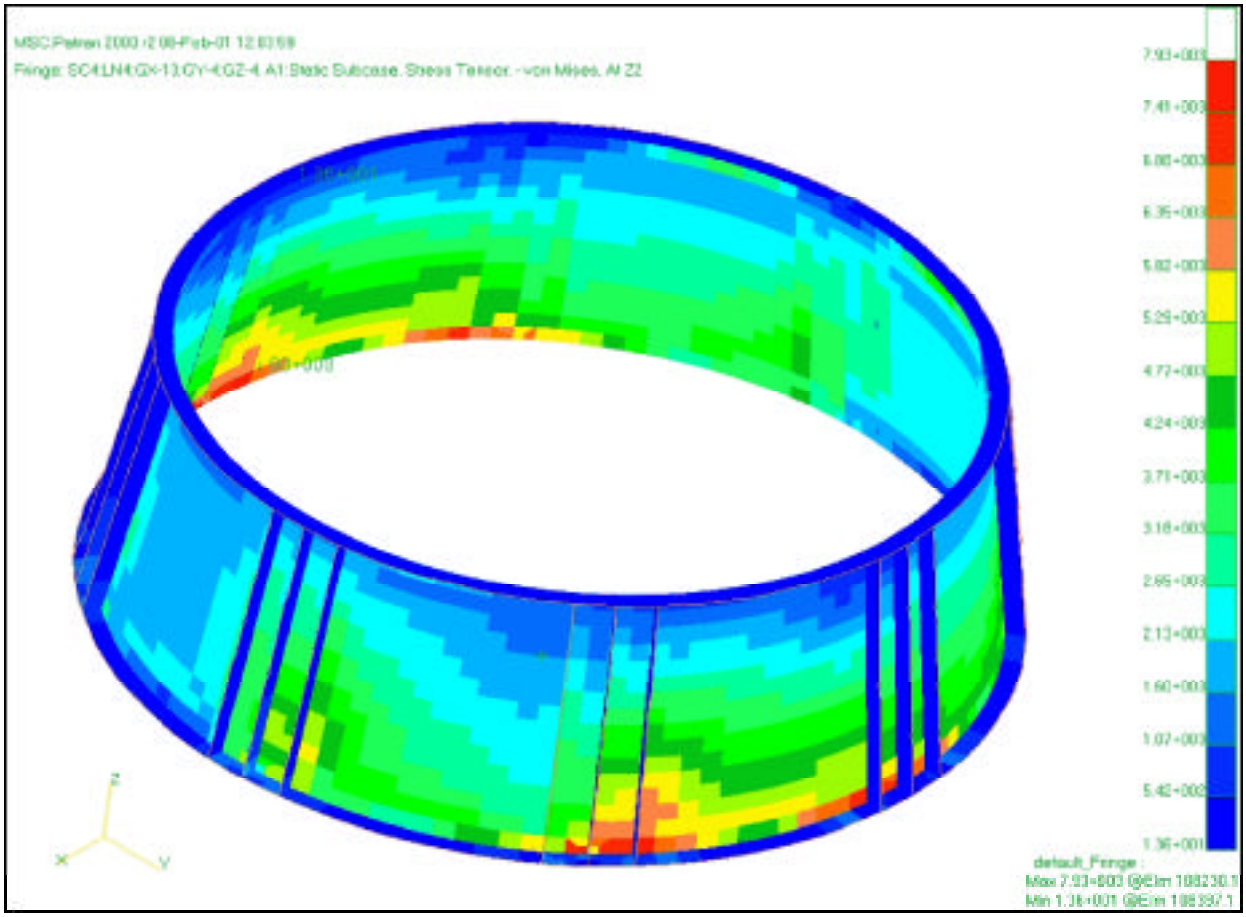

Figure 110: Reflector yield values. The color code on the right has the unit of mmNewton/mm^2.

The interface plates placed between the primary and the secondary structure have to be stiff enough in order to achieve a first eigenvalue higher than 50 Hz. The results of the structural analysis show that the this constraint has been satisfied (see following Figure 111)

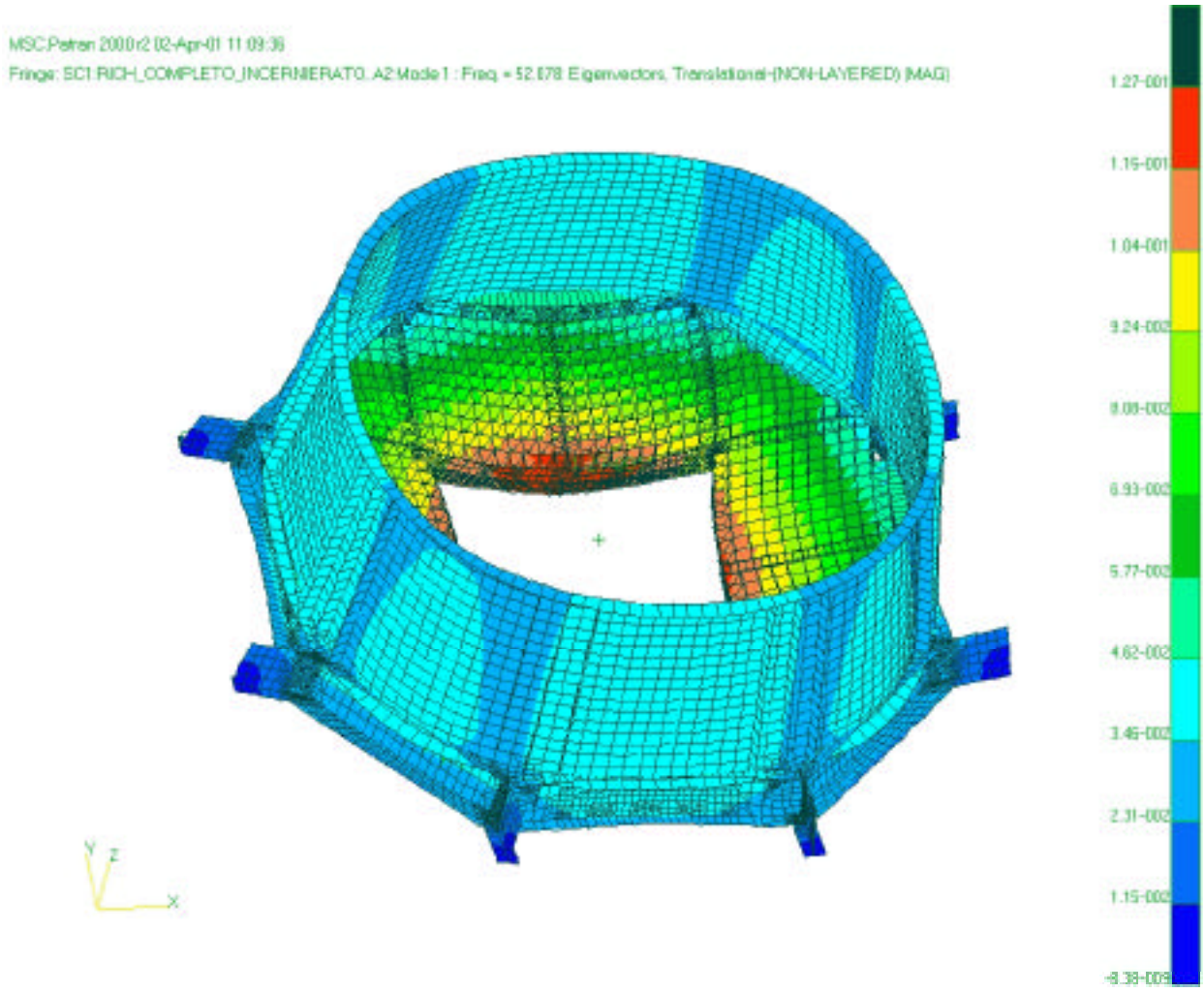

Figure 111: Model analysis results. The color code on the right indicates the deformation in relative units

6. The RICH Electronics

The electronics of the RICH detector has four main parts:

1) The front end electronics;
2) The control and signal processing;
3) The monitoring and setting of working parameters;
4) The voltage power supplies.

The front-end electronics consists of two circuit boards located at the base of each photomultiplier. Their tasks are the biasing, signal conditioning and digitization of the analog signals. The control and signal processing stage is devoted to the generation of sequences of control signals for the front-end electronics and to the processing of the signal. It consists of a set of 24 electronic boards, each with two digital signal processors, three gate arrays, associated memories and a transceiver link to the rest of the system.

The third part deals with the monitoring and the setting of different parameters (like temperature, voltage and current) with a set of eight electronics boards. Last, there is one power supply unit for the high voltages required by the photomultipliers and a second one for the different low voltages needed for the rest of the electronics. Each unit has 24 electronics boards. Except for the front end electronics, all of the rest will be distributed in four electronics crates placed around the detector as shown in the schematic view of the Figure 112. We shall give below a more detailed overview of each one of the different components.

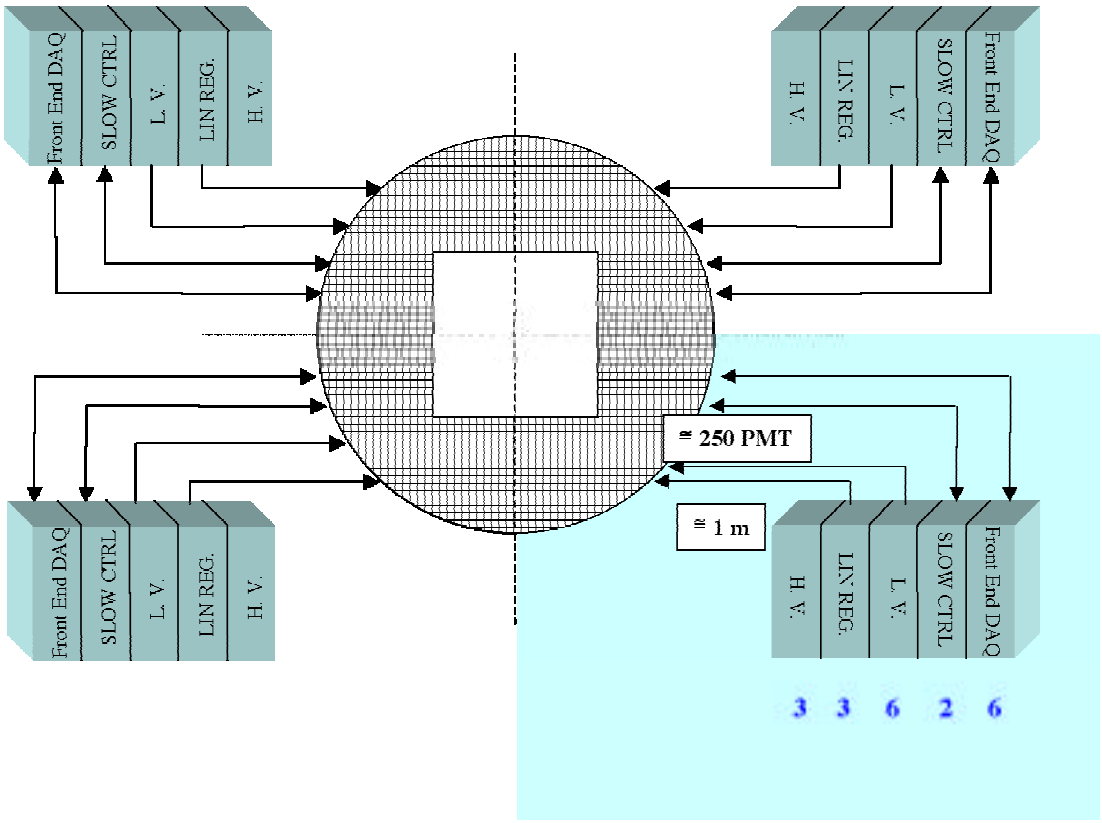

Figure 112: Distribution scheme of the electronic for the Cerenkov detector.

(i) The Front End Electronics

The front-end electronics biases and processes the signal of the photomultipliers. A resistor divider, with a total resistance of 80 Mohms, provides the biasing of each dynode of the photomultiplier optimising power requirements and keeping at the same time the linearity. A 16 channels Charge Sensitive Preamplifier (CSP) specifically designed for RICH reads the detector signals. Each channel output feeds a shaper, implemented with a RC-CR filter. After the shaper, one sample & hold (S/H) per channel fixes the maximum of the shaped signal. In order to increase the resolution for the small signals an amplifier, which selects between a gain factor 1 or 5, has been added to the chain. A multiplexed output buffer drives the signal to a current to voltage converter shared by the 16 channels of each CSP and are digitized afterwards with an analog to digital converter (ADC). A dedicated chip has been developed including S/H, RC-CR filter and output buffer. A serial ADC of 12 bits successive approximations with 1 million of samples per second, low voltage and low power consumption has been chosen for this purpose (AD7476).

A total of 1000 preamplifier chips, ADCs and resistor dividers are required. The implementation of the front end on a set of two small printed circuit boards (one for the resistor divider and one for the preamplifier) and the ADC located at the basement of the photomultiplier is shown in Figure 113.

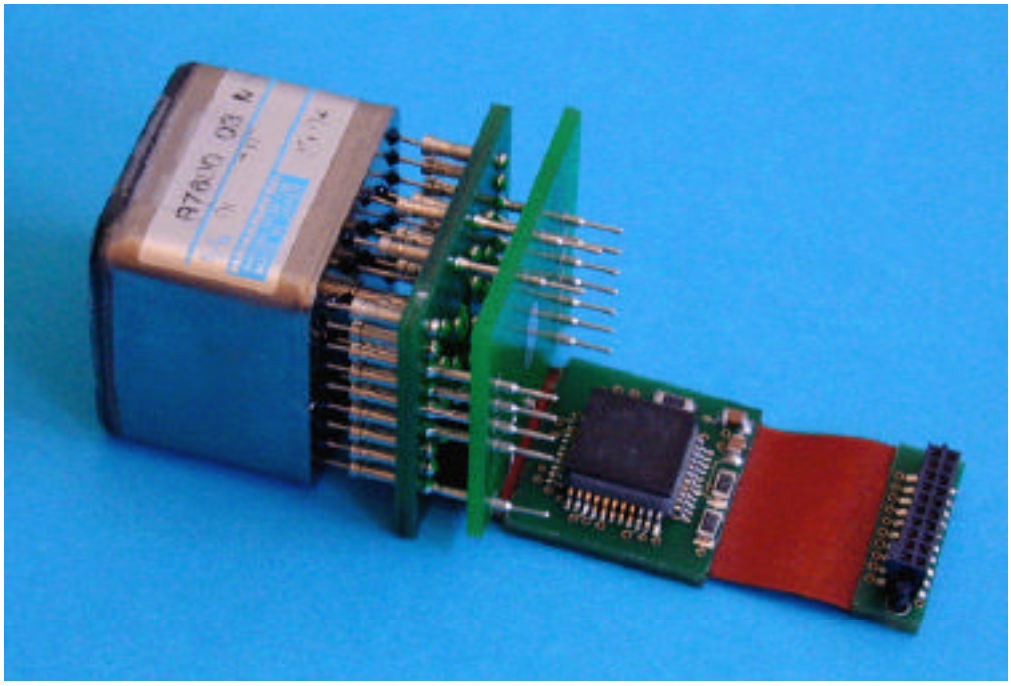

Figure 113: Front End Electronics at the basement of the photomultiplier.

(ii) Control and Signal Processing stage

The main trigger regulates the sample & hold, the multiplexing and the ADC operations. When the trigger signal arrives, a train of pulses is produced. The leading pulse puts the S/H of the front end stage in sample mode waiting for the peak of the signal. The next pulse puts the S/H in the hold mode waiting for the signal to be read out. On the front of each successive pulse the output of each S/H is then readout. At the same time that the signal of each S/H is multiplexed and readout, a successive approximations analog to digital conversion is performed. Two dedicated clock signals are generated for this task during the pulse train. One holds the signal at the ADC input while conversion is performed and the other performs the approximation of the digital output code to the input signal. The digitized signal is then sent to a buffer waiting to be processed. Once the conversion process is completed, the S/H of the front-end chip is reset and the ADC enters in a low power mode while waiting for the next trigger signal. The generation of the control signals and their sequences has been implemented through a state machine hardwired in a field programmable, radiation hard, low power and low voltage gate array.

Signal processing consist basically in pedestals subtraction and threshold comparison. The pedestals are related to the electronic offsets on each channel and the threshold is related to the electronic noise. A significant data reduction is achieved rejecting, on a trigger by trigger basis, those channels with amplitudes below the electronic noise. Once processed, the data are sent to an output buffer until they are read by the main acquisition system. A 50MIPS digital signal processor, with 32K words memory for buffers implementation, has been chosen for this task.

(iii) Monitoring

The performance of the detector depends on the applied voltages, currents values and on the temperature of operation. Therefore, it is required to have a control and a monitoring system. Due to the different kinds of sensors used (analog and digital for monitoring) and the different kinds of control signals needed, a multi-purpose and multi-tasking module has been designed. The main parameters to be set and monitor are temperature, voltage and current of the different power supplies. A set of eight modules equipped with 32 analog input channels, 16 analog outputs, 8 temperature sensor chain inputs, and general purpose control buses will be used for this task. The module is also equipped with a general purpose processor.

(iv) Power Supplies

Due to the different voltage values between the front end and the rest of the electronics (table 15) and for safety reasons two different systems, to be described next, are foreseen.

Low Voltage

Voltage Value	Power required	Ripple
3 V	40 W	< 5 mV
-2 V	15 W	< 5 mV
3.3 V	80 W	< 50 mV

High Voltage

Voltage Value	Power required	Ripple
800 V	16 W	< 20 mV

Table 15: Characteristics of each power supply unit.

(v) High Voltage Power Supply

The High voltage system for the RICH Detector has to provide a regulated low ripple voltage up to 900 V. This voltage is used to bias the photomultipliers and, due to the extremely high dependence of the gain with the voltage, a control and monitoring system is required. This part consists of 24 electronic boards. Half of them contain two voltage elevators. Only one of them works at the time providing a cold redundant system. The input voltage for the elevator is 28 V and the output voltage 900 V. The voltage elevator output feeds a set of 16 high voltage regulators and over current protectors. The output of each over current protector feeds a set of 5 photomultipliers. Each set of 16 regulators is implemented on one dedicated board. The voltage can be regulated between 750 - 850 V.

(vi) Low Voltage Power Supply

The low voltage system feeds all the electronics but the photomultipliers. As shown in table 22, three different voltages are required. Analog voltages feed the front-end chips and ADCs and digital voltages feed the control and processing part. The low voltage system of the Cerenkov

detector has 24 boards and each one has a couple of DC-DC converters, one for the analog part and one for the digital part. Each DC-DC converter has 28 V as input voltage and provide 3.6 V in the digital case and -2.6 V and 3.6 V in the analog case. On the same board there are 4 linear regulators and the associated protection against over current and over voltage. Each one provides power to 22 photomultipliers. A cold redundant system is also implemented for the low voltage system connecting together the outputs from two different boards, working one at a time.

VII. The Electromagnetic Calorimeter (ECAL)

1) Introduction

One of the physics aims of the AMS-02 experiment is the search for dark matter. Dark matter may consist of relic supersymmetric particles, such as neutralinos (χ). The local density of relic neutralinos in the galactic halo can lead to $\chi\chi$ annihilations: these may be identified by detecting e^+, π, γ from $\chi + \chi \rightarrow e^+, \pi, \gamma$... Neutralino annihilations manifest themselves as an excess of positrons above the level determined by the conventional sources. To measure the positron flux one has to make sure that the positrons are not confused with other particles much more abundant in the cosmic rays. For example, protons are the main background source of positively charged particles: at energies higher than 10 GeV there are ~ 10^4 protons for each positron. Therefore to look for $\chi\chi$ annihilations in the positron spectrum, protons have to be suppressed by a factor 10^6. To reach this result, AMS-02 has a sampling electromagnetic calorimeter (ECAL) which measures the energy, longitudinal and transversal parameters of the particle induced shower.

To obtain a clean $e^{\pm}$ sample over hadrons it is important to separate the $e^{\pm}$ detectors by a strong magnet so that hadron's δ-rays from the first detector do not enter into the second $e^{\pm}$ detector. In this way we can multiply the rejection power of the TRD and the ECAL to reach a rejection $h/e > 10^6$ (see Figure 2).

The rejection capability through the shower shape analysis depends on both the momentum resolution of the AMS-02 tracker and the energy/spatial resolution of the ECAL. A 3D sampling calorimeter, with an energy resolution $\sigma(E)/E$ $12\%/\sqrt{E} + 1.5\%$ (GeV) and fine granularity, provides a proton background suppression of ~ 10^4 up to hundreds of GeV. This together with TRD rejection of > 10^2 (see test beam result of the TRD section) ensures a $h/e > 10^6$.

The ECAL is being constructed by an international collaboration coordinated by F. Cervelli of INFN-Pisa, together with H.S. Chen of IHEP, Beijing, and J.P. Vialle of LAPP, Annecy, France.

Two identical ECAL modules are under construction. The first will be used for space qualification tests and beam tests at CERN during the summer 2001. The second module will be the flight unit.

2) The ECAL Structure

The Pisa Group has a unique experience in building the large KLOE Electromagnetic Calorimeter with lead-scintillator fibers to measure the 3D shower shape. The AMS ECAL design builds on this experience. The ECAL will be a lead-scintillating fiber device. The calorimeter is a square with 658 x 658 mm on the side and is 166.5 mm in thickness. It is subdivided into 9 super layers, each 18.5 mm thick. The super layers are arranged so that the scintillating fibers are running in orthogonal directions (Figure 114).

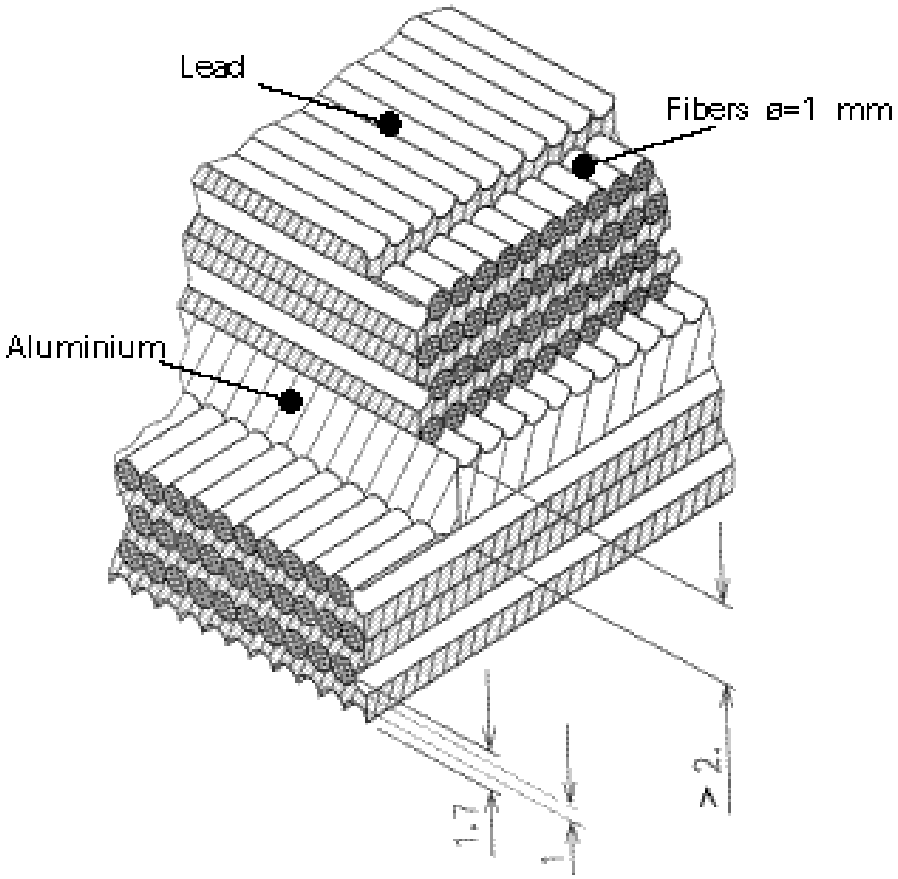

Figure 114 : Layer structure of the AMS ECAL.

Each layer consists of grooved lead foils, 1.0 mm thick, interleaved with 1 mm diameter scintillating fibers glued by means of an epoxy resin. The grooved lead foils were obtained by rolling 1.4 mm thick foils with special “shaping” machines developed in Pisa. The foil equivalent thickness (1 mm) was measured to be uniform within a few tens of microns; the grooves where the scintillating fibers are positioned deviated from a straight line by less than 0.1 mm.

To construct each super layer, the following stacking procedure is used: (i) a smooth layer of glue is applied on the lead foil; (ii) the fibers are positioned into the lead foil grooves; (iii) a new lead foil is glued on the fiber layer.

The epoxy resin is Bicron BC-600ML with a 0.28 ratio between hardener and glue to ensure a handling time of 1.5 hours. This epoxy does not damage the fibers.

To construct the ECAL, the two end faces and two lateral sides of each super layer are machined accurately with a numerically controlled milling machine. The resulting structure is shown in Figure 115.

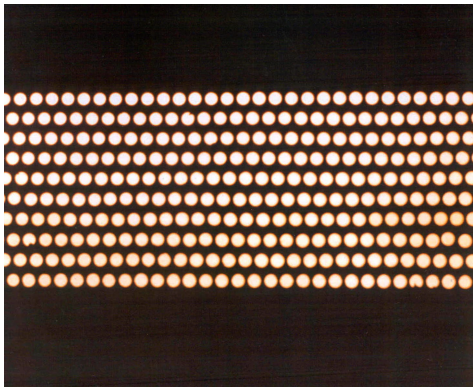

(a)

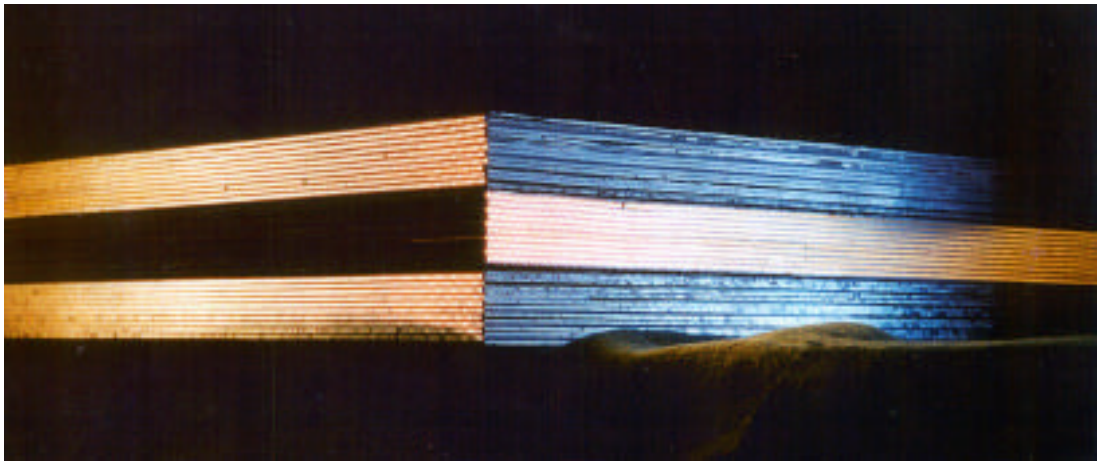

(b)

Figure 115 : a) side view of a super layer, b) assembly of 3 super layers according to the final structure.

The resulting composite structure has a lead-fiber-glue volume ratio of 1.:0.58:0.15. The average density is 6.85 ± 0.3 g/cm^3; the radiation length is about 11 mm and therefore the ECAL total thickness is 15 X_0 with a weight of 492 kg.

Preliminary tests on small calorimeter prototypes (Figure 116) filled with scintillating fibers (Pol. Hi. Tech. 0046) have been done using minimum ionizing cosmic rays.

Figure 116: Prototype ECAL.

From the tests, we learned that the fibers have the following properties:

a) attenuation length in the range 3 to 4 m :

b) a fast time response characterized by a decay constant τ in the range 2.2 to 2.5 ns;

c) a light propagation velocity of about 17 cm/ns;

d) a light yield corresponding to 11.7 detected photo-electrons per cm of crossed fiber material at a distance of 6 cm from the cathode of a bialkali linear focused photomultiplier.

3) The mechanical structure

The active part of the calorimeter is tightly housed in a light tight mechanical structure capable to withstand accelerations/decelerations up to 11 g. The specifications of the ECAL mechanical support are reported in Table 16.

Total weight:	≤ 600 kg
Design Load Factors:	Fx = ± 7.8 g's, Fy = ± 7.8 g's, Fz = ± 11.1 g's Rx = ± 146 rad/sec^2, Rx = ± 123 rad/sec^2, Rx = ± 51 rad/sec^2
Safety factor:	1.4
First natural frequency:	> 50 Hz

Table 16: ECAL mechanical support dynamic properties.

The structure consists of three main components: a) two honeycomb end plates, covering the upper and lower faces of the calorimeter, b) four lateral aluminum plates, accurately machined to house the light-guide/PMT package and c) four brackets, positioned at the corners, connect the ECAL to the USS. The ECAL mechanical structure is shown in Figure 117.

Figure 117: Mechanical support.

Each lateral plate is backed by another back panel (see Figure 118) to rigidly secure and transfer the heat out of the light-guide/PMT packages.

Figure 118: A back panel.

4) Light Guides and Photomultipliers

The light from the fibers is collected by photomultipliers through light guides, shaped as an empty truncated pyramid with reflecting material glued on the polycarbonate support tube (Figure 119). Fibers are read out on one side only.

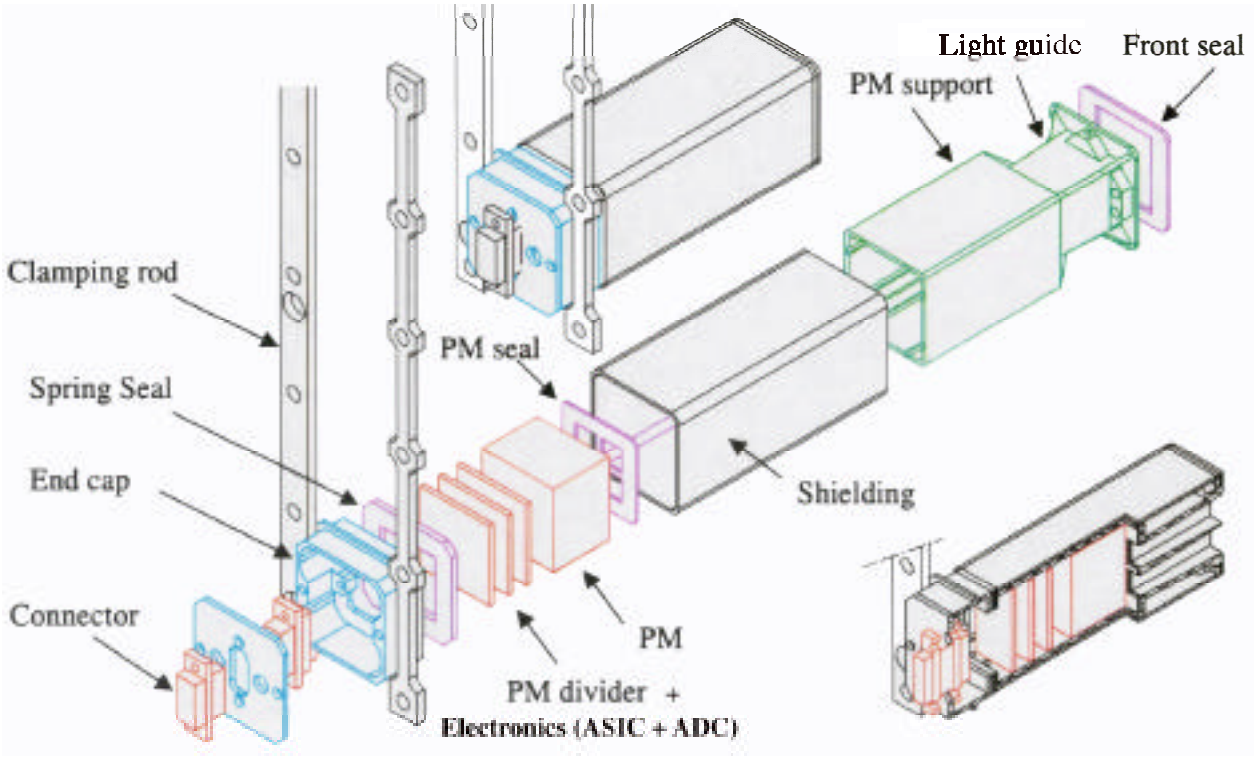

Figure 119: PMT mechanical assembly.

The light guide geometry has been chosen so as to fit the active area of each of the 4 cathodes on the surface of Hamamatsu R7600 00-M4 photomultipliers. The region seen by one of the four cathodes is called a "cell". Each photomultiplier has 4 square regions of 9 x 9 mm^2. As a result the calorimeter is subdivided into 1296 cells, corresponding to 324 photomultipliers (Figure 120). The PMT HV dividers together with the front-end electronics are packaged behind the PMT and potted to avoid HV discharge.

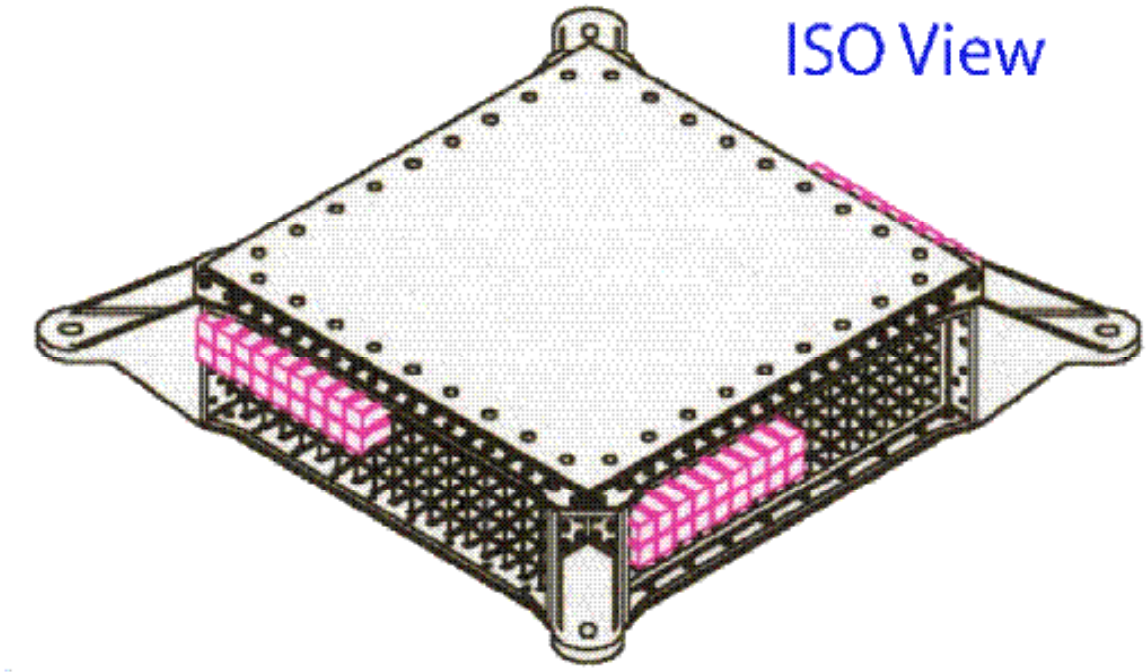

Figure 120: Calorimeter mechanical structure. Samples of PMT's are shown in red.

The photomultipliers are located in a region where the magnetic field is 0.1 to 0.2 KGauss at a varying angle with respect to the PMT. For this reason a "metal channel dynode" photomultiplier has been selected, which is specifically designed to operate in a magnetic field. To study its behavior, several PMTs have been tested in a magnetic field. The PMT gain is dependent on both the field value and direction. As shown in Figure 121, a thin μ-metal shield has been included to remove field effects.

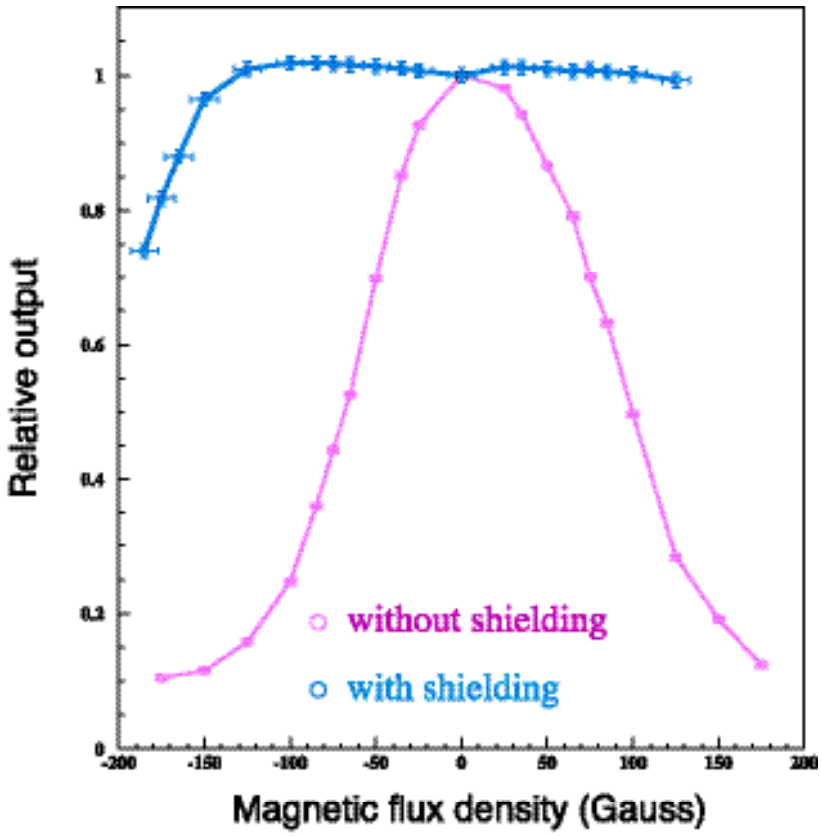

Figure 121: Behavior of PMT R7600 00-M4 in magnetic field.

5) Thermal Analysis

Since AMS-02 is an external payload, severe limits on the heat dissipation towards neighboring payloads and the ISS are imposed. Each of the 324 PMT's, located on the ECAL lateral panels, is supplied at 800 V with a current of about 150 μA. This results in a single PMT power dissipation of about 0.12 W and in an overall dissipation of about 39 W.

The temperature range requirements and power dissipation for ECAL are summarized in Table 17 . The survival temperature has been derived from the study of several ECAL prototypes inside a thermal chamber.

The thermal interfaces have been approved by NASA and the thermal engineering of the ECAL is being conducted by Carlo Gavazzi Space of Italy.

Item	Power (W)	Survival Temperature range [^{0}C]	Operational temperature range [^{0}C]
PMT	0.12	-60…+60	-40…+40
Front end electronics	20	-60…+60	-40…+40
9 super layers	0.0	Constrained by thermal expansion effects	Constrained by electronics

Table 17: Temperature requirements for ECAL.

6) Front-End Electronics and HV System

The front-end electronic chain consists of an amplification stage followed by a shaper and sample-and-hold. This chain was integrated into a custom "ASIC" chip. The chip was implemented in D-MILL technology to ensure radiation hardness and the power consumption was limited to 0.8 mW per channel. The main feature of this chip is its large dynamic range to fulfill the physics requirements to detect from MIP signals up to the e.m. showers from 1 TeV particles (producing up to ~ 10^4 MIP signal equivalents in a single channel). Figure 122 shows the chip layout.

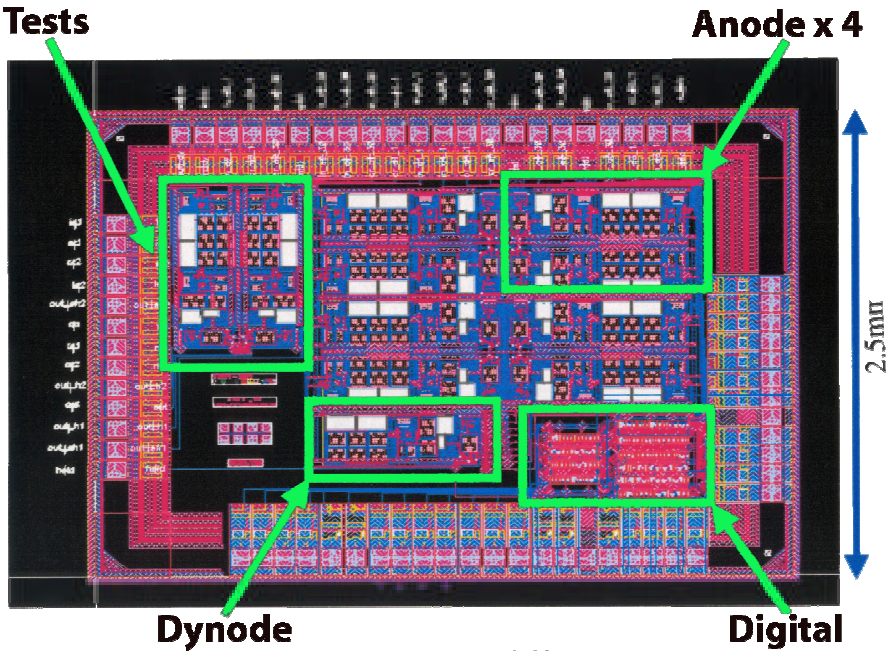

Figure 122: Front-end electronics chip showing the circuit to read out 4 Anodes, 1 Dynode and test circuits for one PMT.

This chip, together with a 12 bit ADC, is integrated into the mechanical structure supporting the PMT, as shown in Figure 119.

The digital output of the ADC is fed into the digital section of a card, containing a Digital Signal Processor (DSP) and related control logic. The read-out is carried out via a standard AMS data acquisition card (DAQ).

The ECAL HV system consists of two main elements: a) a DC-DC elevator (from 28 V to 850 V); and b) a linear regulator (from 0 to 800 V).

The DC-DC elevator is protected against over-current and over-temperature and is stable when providing up to 6 W maximum power. One elevator can feed ~40 tubes. The linear regulator features are: (i) an output voltage settable from 0 to –800 V with 8 bit resolution; (ii) a shut down capability for each single channel; (iii) an output voltage monitor with 8 bit resolution; (iv) an output current protection in constant current mode.
As shown in Figure 123, the elevator will be doubly redundant (one hot – one cold), to ensure long term reliability.

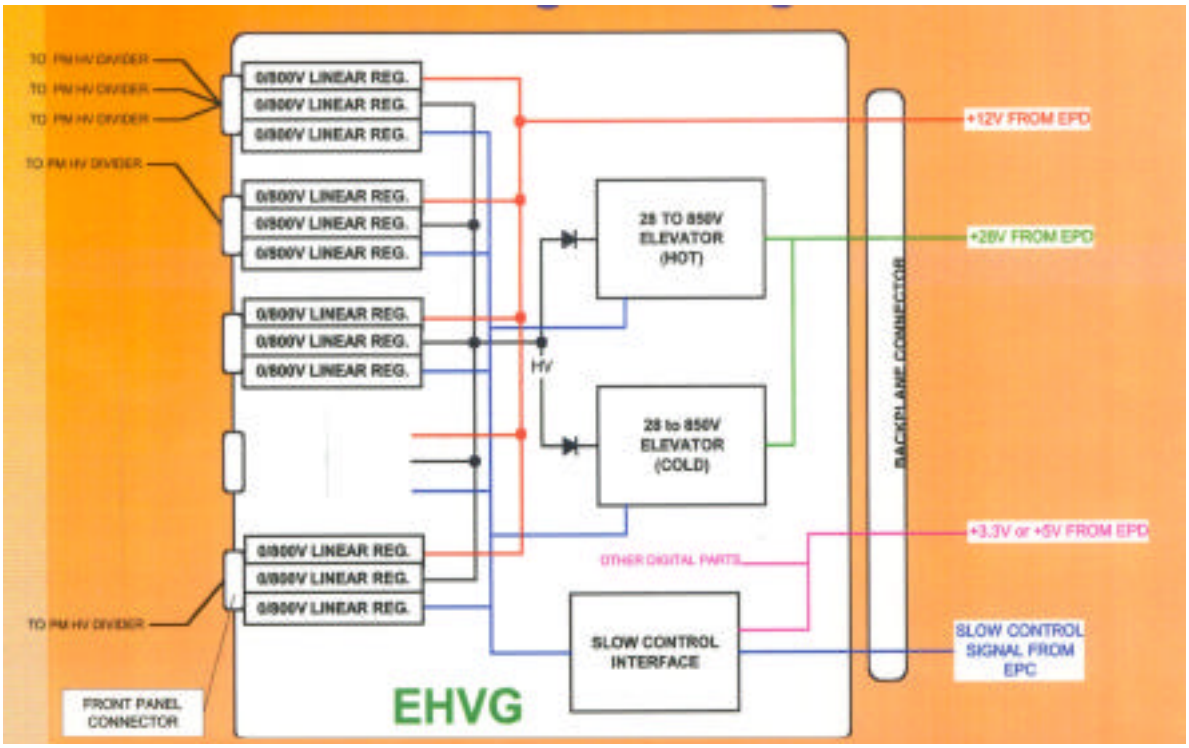

Figure 123: Schematic layout of the HV system.

7) Calorimeter Prototype Beam Test

A calorimeter prototype (Figure 124), with the final thickness (9 layers, 166.5 mm) but with reduced surface (230 x 230 mm^2), was tested in August 2000 at CERN using pions, electrons and protons with energies ranging from 5 to 250 GeV. In this test 36 PMT's were installed on the calorimeter with an effective active surface of 72 x 72 mm^2. The measured e^-, p spectra at 40 GeV are shown in Figure 125.

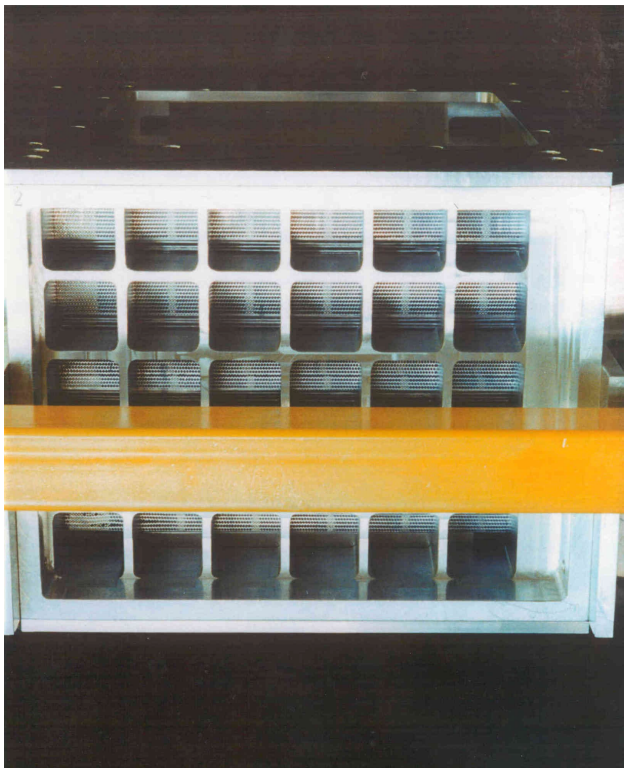

Figure 124: (23x23) cm^2 ECAL Prototype.

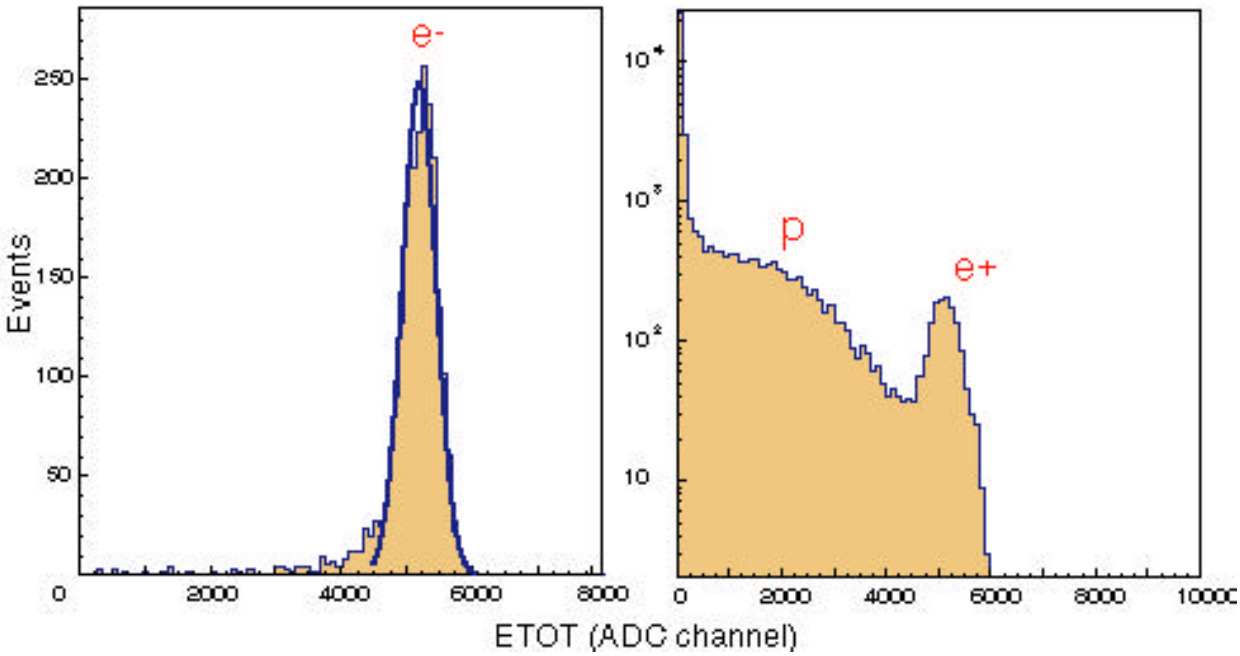

Figure 125: Energy spectra at 40 GeV for electrons (on the left) and protons (on the right). The peak in the proton spectrum is due to the positron contamination of the beam.

The energy resolution was found to be 12%/√E (GeV) + 5% for electrons in the range 1 to 100 GeV. While the energy dependent term of the resolution is consistent with previous Monte Carlo calculations, the constant term is larger then expected (~1.5%) owing to: a) pending PMT calibration and b) the reduced dimensions of the prototype active area.

The imaging capability of this calorimeter is illustrated in Figure 126, where the mean longitudinal profiles for 100 GeV electrons and protons are plotted. The longitudinal granularity is clearly sufficient to discriminate electrons from protons.

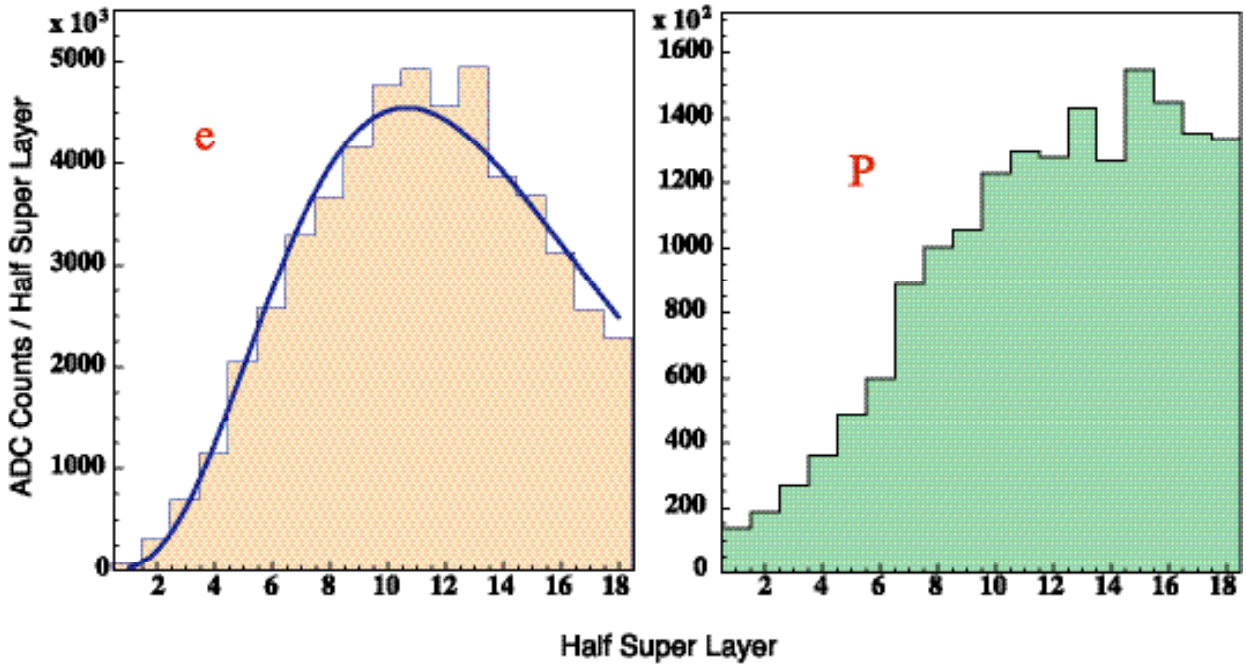

Figure 126: Mean longitudinal profile for electrons (on the left) and protons (on the right) at 100 GeV.

As mentioned in the introduction section, a full-size calorimeter will be tested at CERN test beams during the summer of 2001.

VIII. AMS-02 Electronics

1) Introduction

The electronics of AMS-02 is organized as five systems : subdetector electronics, ancillaries, power and thermal, monitoring and control, and trigger and data acquisition. Key to understanding the function of the electronics is understanding the NASA provided interfaces. Figure 127 shows the major AMS-02 electronics elements.

The physics data flow in the electronics is driven by the trigger system. This system recognizes when a charged particle has passed through the detector based on the coincidence of fast signals from the time of flight scintillators. It then looks at fast signals from the veto counters and ECAL to check that the particle cleanly passed through the detector. This trigger rate is estimated from the measurements performed by AMS-01 to vary from 200 to 2000 Hz, depending on the geomagnetic latitude. The electronics system is being conservatively designed to perform precision physics at twice these rates.

High energy gamma rays are triggered when they pair produce electrons in the upper part of the detector and by a stand-alone trigger from the ECAL. These will contribute substantially to the trigger rate.

The electronics effort is coordinated by Dr M. Capell of MIT, and MIT is involved in most parts of the electronics. The other key contribution comes from our Taiwanese collaborators.

As shown in Figure 128, commands and data flow to the ground data handling complex, which is described at the end of this section.

2) Interfaces

As indicated in Figure 128, NASA provides three electrical interfaces on the ISS: power, Low Rate Data Link (LRDL) and High Rate Data Link (HRDL). The interfaces are located physically within the Umbilical Mechanical Attachment (UMA) located at bottom of the USS. After AMS is mechanically installed on the ISS attach site, the UMA activates and mates the connectors. Then power is applied, the data links activated and experimental operations commence.

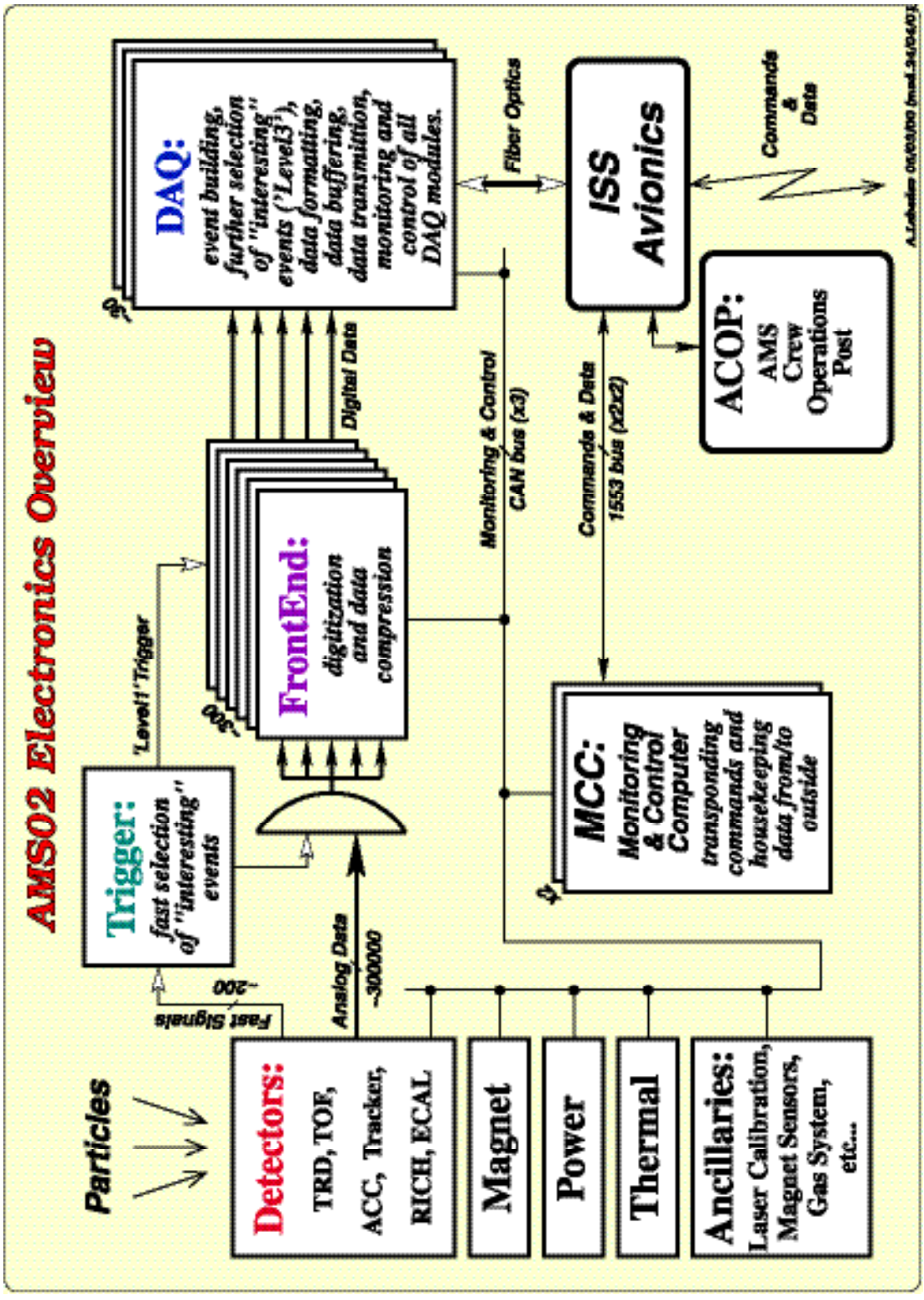

Figure 127 : Overview of AMS-02 Electronics on the ISS.

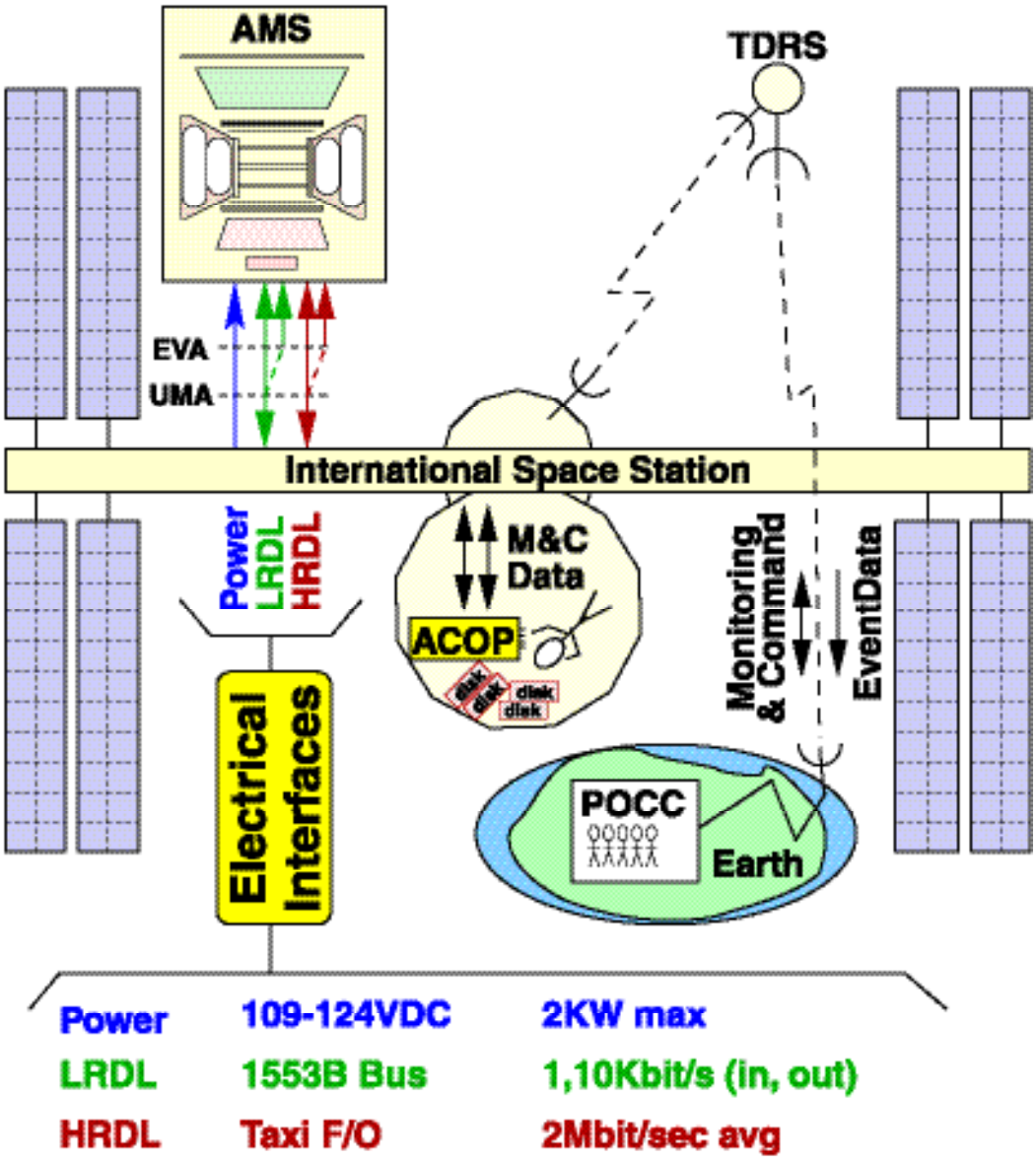

Figure 128 : AMS electrical interfaces on ISS.

(TDRS : Tracking and Data Relay Satellite,
POCC : Payload Operations and Control Center,
M&C : Monitoring and Command).

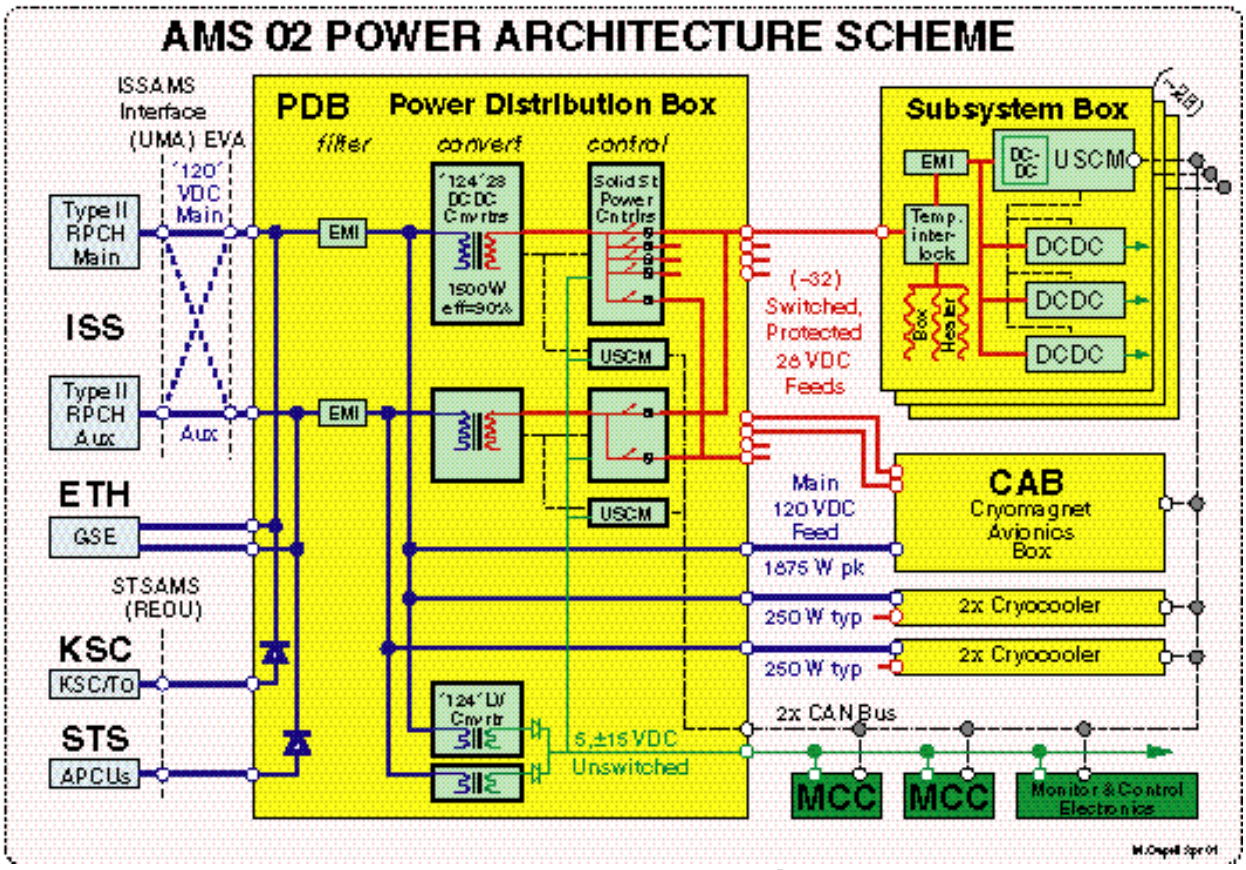

Figure 129 : AMS-02 Power Architecture.

(RPCH : Remote Power Control Hardware on ISS,
GSE : Ground Support Equipment at ETH-Zürich,
KSC/TO : Cable disconnected from shuttle at launch,
APCU : Assembly Power Conversion Unit on shuttle (STS)).

(i) Power Interface

The power source on ISS are the eight large solar arrays. AMS will have two power feeds, each one connected to one of the arrays. The power is provided at voltages ranging from 109 to 126 VDC with 124 VDC nominal. The maximum power draw allocated to AMS is 2000 W summed over both feeds, this limit being extended to 2300 W for the final 30 minutes of magnet charging.

Stringent requirements are placed on AMS by ISS in terms of isolation, grounding, electromagnetic compatibility, inrush current, and complex impedance. To accommodate these requirements, and to maximize the overall power efficiency, we have adopted the power architecture shown in Figure 129. For each of the two feeds (Main, Aux.), the power distribution box (PDB)

contains an electromagnetic interference filter (EMI), a set of DC to DC converters, and 32 solid state power controllers (SSPC). The filtering protects the rest of ISS from noise generated by the experiment and the experiment from other noise sources on the station. The converters provide the first isolation barrier and deliver a stable 28 VDC to each of the subsystem boxes. The SSPCs are essentially remotely controlled circuit breakers. The 32 paired outputs from the SSPC's are simply OR'ed to supply each of the subsystem boxes with power from either of the two ISS feeds.

Special provision has been made to feed the cryomagnet avionics box (CAB) and the cryocoolers directly with 124 VDC.

A small amount of power is also directed though another pair of converters to provide an "Unswitched Power Supply". This is required to get the data links attached to the Monitoring and Control Computer (MCC) up and running and for other critical functions, for example to power the PDB control circuits.

This scheme attaches the minimum number of units to the ISS feeds, which allows the ISS requirements to be met. It also provides full monitoring, protection and control of the power to each box. The large size (1600 W) of the DC-DC converter sets allows a high efficiency (90%) in the conversion to 28 V, while minimizing the voltage fluctuations and noise that could be induced into the sensitive detector electronics.

The scheme within a typical subsystem box, for example an individual crate, is also shown in Figure 129. The box receives the 28 VDC into a temperature interlock which ensures that the electronics is not powered should it be outside of the operational range. When in range, after further filtering to avoid box to box interference, power is applied to a Universal Slow Control Module (USCM). The USCM then initializes and starts the other power supplies within the box in response to defaults and commands received from the MCC.

NASA planning indicates that no unscheduled interruptions will occur and that full power will be available for AMS about 364 days per year. However, given the lack of operational experience with ISS to date, our systems are planned to survive reduced and zero power levels foreseen or not.

(ii) Low Rate Data Link (LRDL) Interface

The LRDL is based on the MIL STD 1553B dual bus, which is widely used in aircraft. AMS has two MCC's which can process the LRDL data, however as there is only one connection available, an EVA connector has been installed should the active MCC fault. As shown in Figure 130, the MCC redistributes the commands received on the LRDL along the internal AMS CAN bus to the appropriate slave unit, typically a USCM. Within each slave is an interface to the CAN bus (CAN I/F) and a micro-controller (uProc) which sets, for example, switches and digital to analog converters (DACs) and reads monitors of temperature, voltage and current (T, V, I). As shown, the slaves are dual redundant.

The data returned from this slave is appropriately formatted and sent on to the LRDL. As shown in Figure 131, it then proceeds through a series of NASA units and then via radio beam to Earth, where it is routed to the AMS Payload Operation and Control Center (POCC). The NASA units involved include : the S-band with 50% duty cycle, the ACBSP S-band receiver, the Command and Control (C&C) Multiplexer/Demultiplexer (MDM), the Payload (P/L) MDM, the Automated Payload Switch (APS), the High rate Communications Outage Recorder (HCOR), the High Rate Frame Multiplexer & High Rate Modem (HRFM/HRM), the Ku-band system connecting the ISS via the Tracking and Data Relay Satellite (TDRS) through the White Sands Ground Complex (WSGC) to the Marshall Space Flight Center (MSFC), Johnson Space Center (JSC) and the AMS Payload and Operations Control Center (POCC). Within the US Lab on the ISS, the astronaut crew has access to this data via their Portable Control System (PCS) laptops and via the AMS Crew Operations Post (ACOP).

In total AMS is allocated about 10 KBits/sec of data bandwidth on the LRDL, with an expected duty cycle of up to 70%. A few highly summarized bytes per second of health and status data may be available and sent with near to 100% duty cycle. Commands originate in the POCC and follow the inverse path, the maximum command rate being about 1 Kbit/second. Along the way the ISS crew and NASA ground controllers can peek at this data, and, should the need arise, have the facility to issue a few key commands, for example to put the experiment into a standby state.

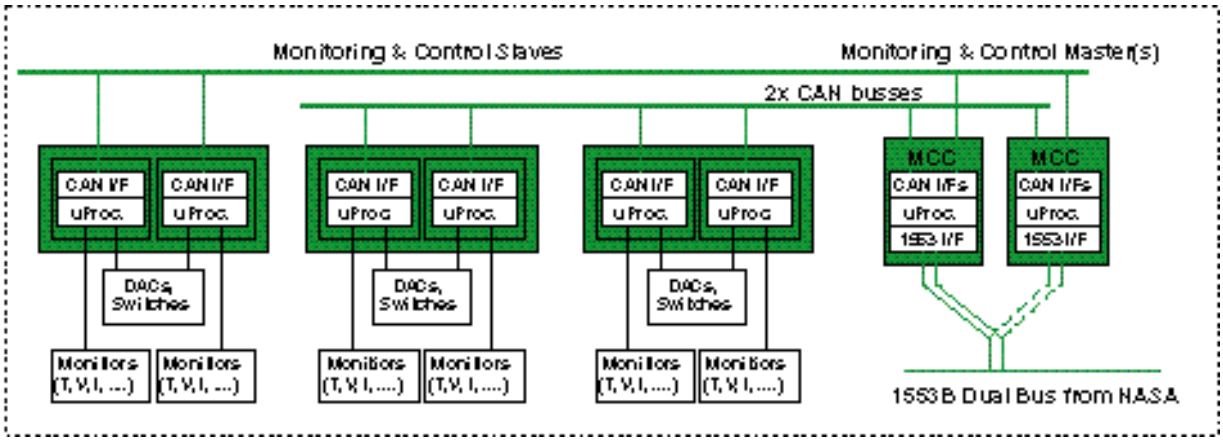

Figure 130 : Monitoring and Command flow within AMS.

(iii) High Rate Data Link (HRDL) Interface

The HRDL is the main data conduit out of AMS. It is based on a NASA specific implementation of fiber optic communications. The link can move data on the ISS at speeds up to 90 MBit/sec, and the radio down link supports up to 43 Mbit/sec, again with an at best duty cycle of 70%. Of this AMS has been allocated an orbit average of 2 Mbit/sec. The data flows from AMS over the paths shown in Figure 132. A key element in this path is the ACOP, which will be mounted in an express rack inside of an International Standard Payload Rack and is discussed below. The data arrives at the link from buffers located in the top level data acquisition computers.

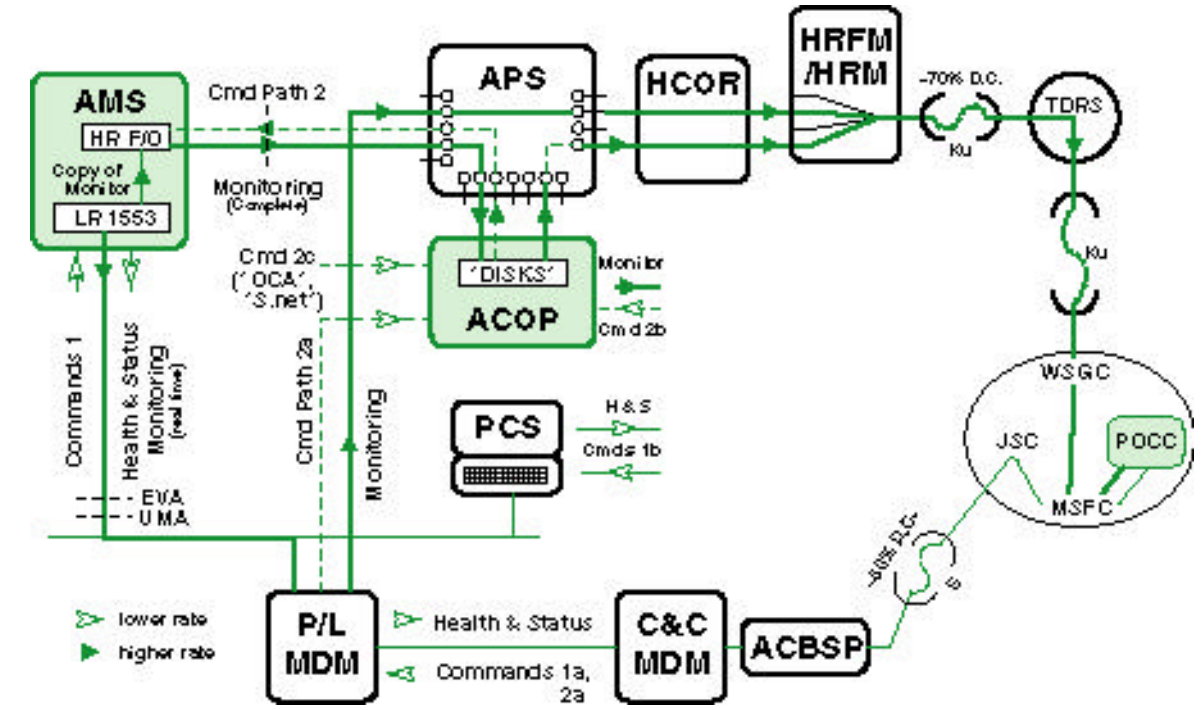

Figure 131 : Monitoring and Command Data Flow over both the LRDL and HRDL

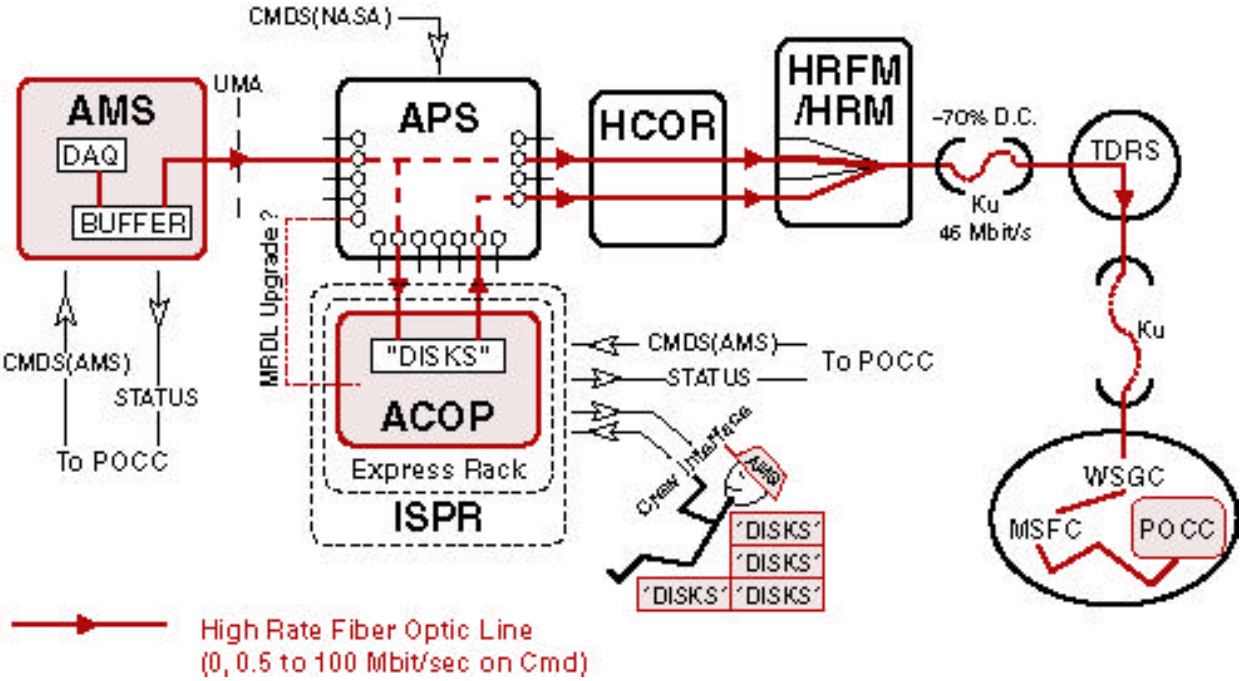

Figure 132 : AMS Command and Monitoring of High Rate data flow.

3) Subdetector Electronics

Though the detailed requirements imposed by the physics are different for each of the subdetectors, a unified approach has been adopted for their electronics. This approach is based on the successful experience gained with the AMS-01 engineering flight, updated for new technologies, for the subdetectors which were not installed on AMS-01 and for the tight resource requirements both on the ground (time, money, manpower) and on orbit (weight, power, data rate). This approach is shown in Figure 133. Analog signals from the detectors enter a detector specific Application Specific Integrated Circuit (ASIC) and are first shaped, and then held in response to a trigger, the trigger having been generated using signals from the detectors as shown in Figure 134. The held signals are then multiplexed with the ASIC. These are mounted close to the detector elements. Before or after digitization, typically with an ADC, the output is then sent over a cable to the data acquisition electronics.

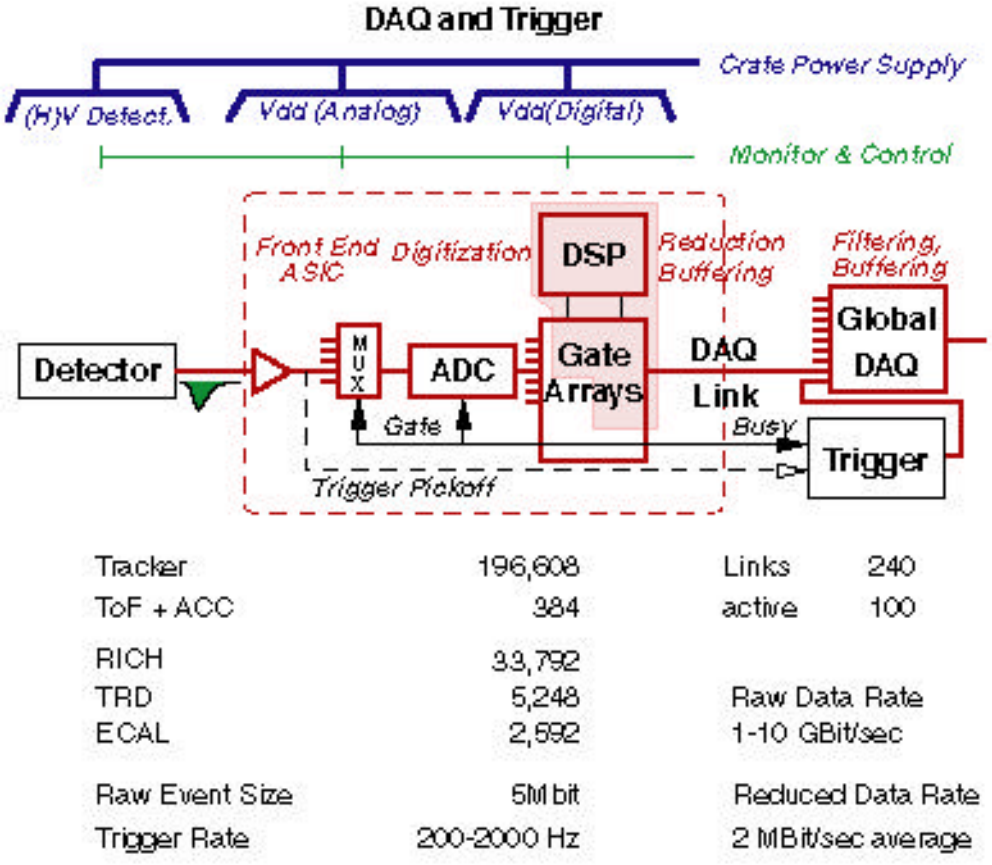

Figure 133 : Subdetector DAQ Electronics showing the channel count for each subdetector and the total rates and event sizes.

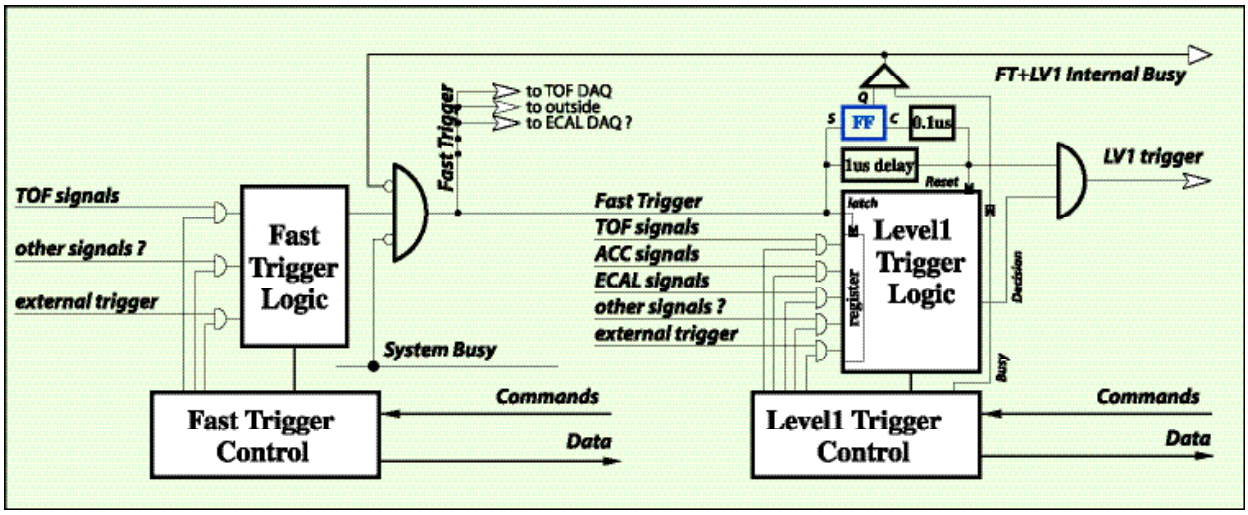

Figure 134 : Fast (FT) and Level-1 (LV1) Trigger Scheme. FF indicates a flip flop used to hold the internal busy until the subdetector electronics can respond.

Each of the subdetectors also requires power for the detectors, as well as power for the electronics. This is supplied by the DC-DC converters shown in Figure 129. Monitoring and control of the detector parameters, in addition to the power supplies, is also performed by the USCM.

4) DAQ and Trigger Electronics

From this point the data acquisition circuits are common for all the detectors. The raw digital information from about 1000 signals is reduced and buffered in a digital signal processor (DSP) (see Figure 133). When resources are available to receive it, the DSP output is shipped over a special data acquisition link into the global data acquisition tree as shown in the upper half of Figure 135. This happens in parallel for all of the detector elements with about 300 front end DSPs. The data from an event is successively agglomerated as it works its way down the DAQ tree. This tree consists of layers of nodes, each of which connects up to 24 branches into one stem. The nodes are again based on the common data processing circuit using a DSP.

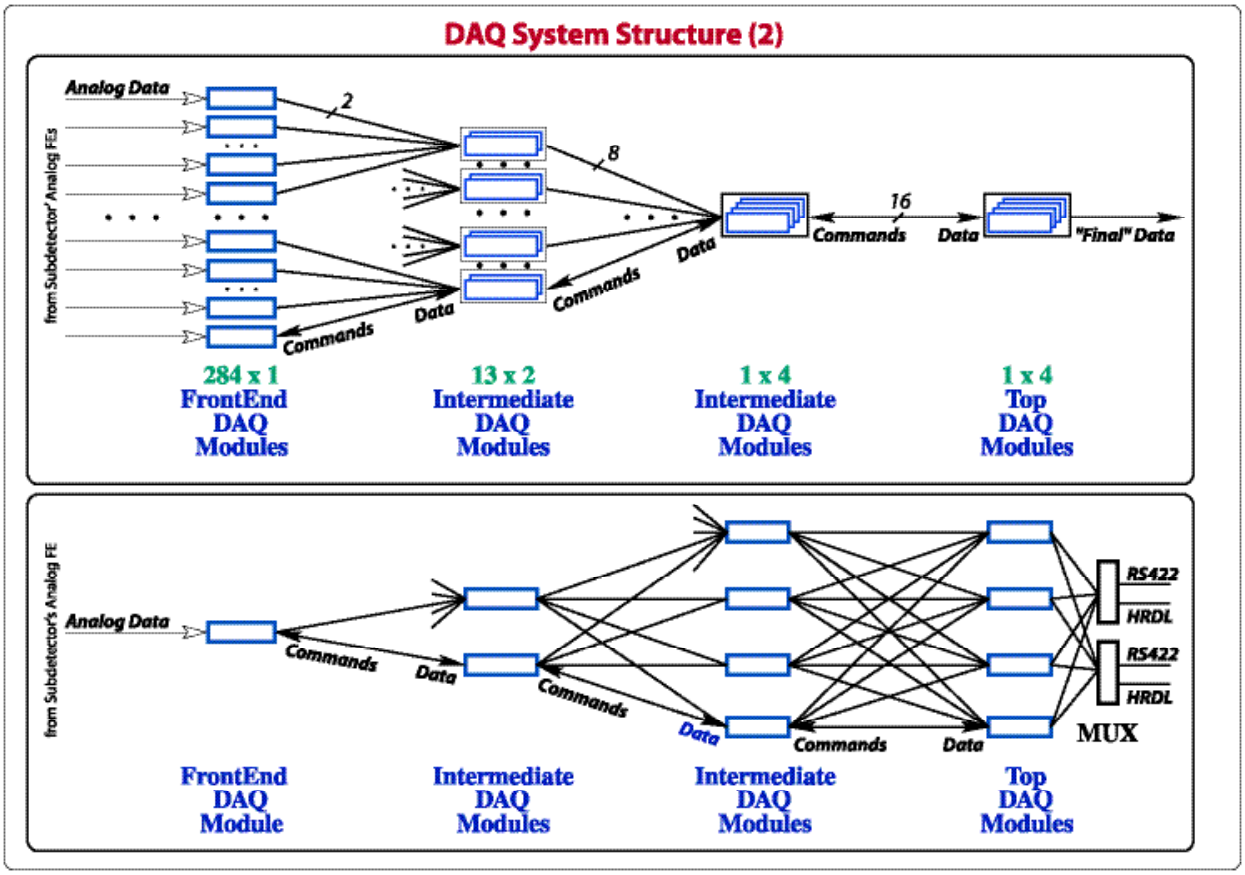

Figure 135 : The DAQ tree with redundant links.

At the root of the tree sits the Main DAQ Computer (JMDC), which receives the complete event. The JMDC analyses each event to ensure that it might contain interesting physics and also to monitor the detector performance. The event data is then buffered and sent out the HRDL when it becomes available.

The number of digitizations in response to each trigger is also given in Figure 133. For each trigger the resulting raw event size is 5Mbit. With the expected trigger rate of 200 to 2000 Hz, this yields a raw data rate of 1 to 10 GBit/sec. The initial data reduction in the DSP, shaded in the figure, is expected to reduce the event size by a factor of about 500. With the filtering in the JMDC this should allow the average allocated rate of 2Mbit/sec to be met.

After a thorough investigation of the available technologies and, again, based on our AMS-01 experience, the DAQ links in the tree are being developed by the collaboration to best meet our specific requirements (speed, reliability) and constraints (power, weight). A key to this is the large

degree of redundancy in the design, as shown Figure 135 and summarized in Figure 136. The output of each of the 300 front end DSPs can flow over either of two links, intermediate nodes are cross connected with four links up and down, and four JMDCs, each of which can do the job, are being flown.

The JMDC is based on a powerful recent microprocessor, the IBM PowerPC 750, which we are implementing into a custom built computer using a compact format PCI bus (cPCI), with specific peripheral interfaces to a 2 GByte solid state memory buffer, which is required when the HRDL is not available, to the AMS CAN bus for monitoring and command transfers, to the DAQ links and to the HRDL.

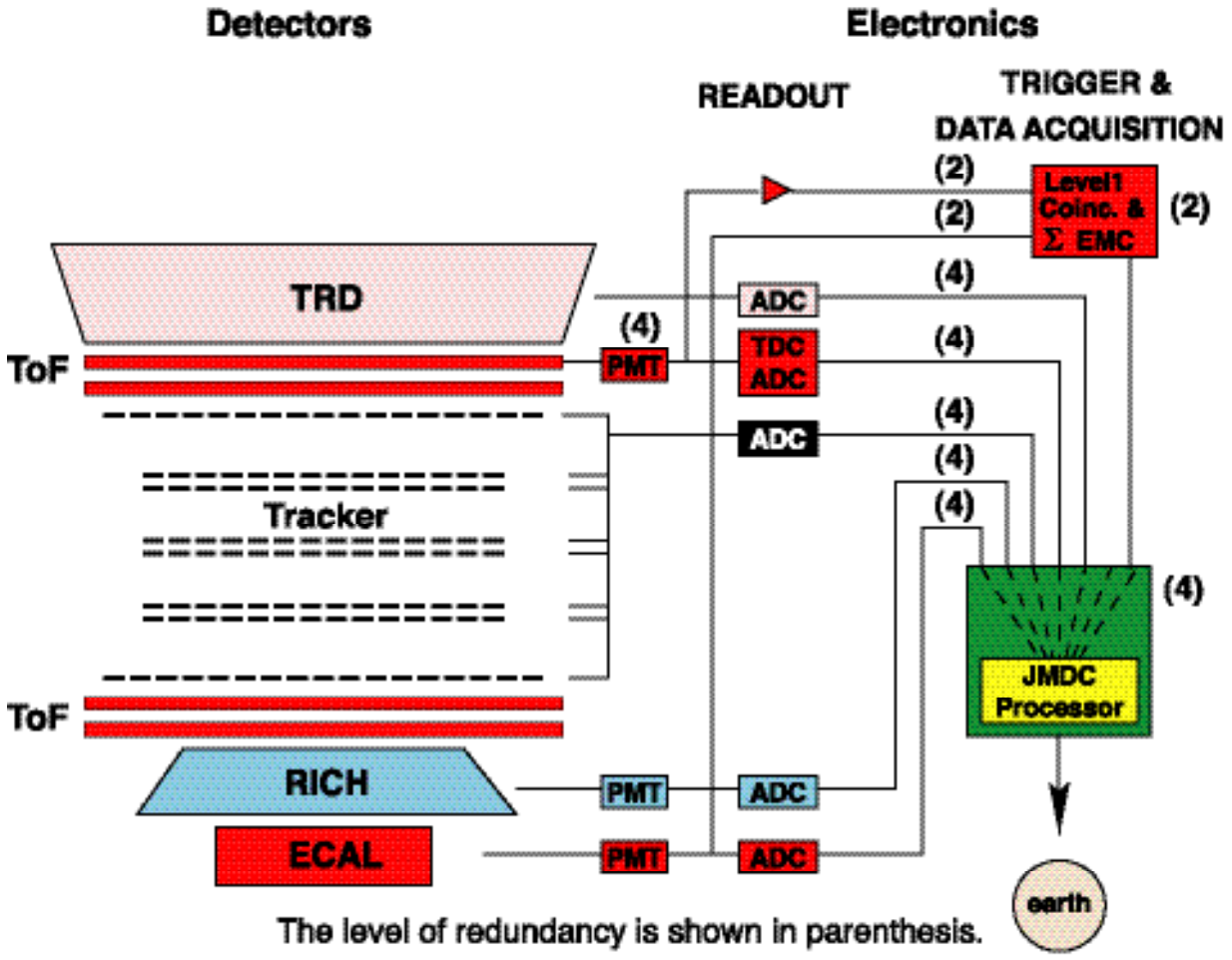

Figure 136: Redundancy in AMS Electronics.

5) AMS Crew Operations Post (ACOP)

The function of ACOP is to permanently record all the data coming from AMS. It is located inside the ISS in the US Lab which is the main work area for the crew. ACOP allows the crew a flexible interface for monitoring and, should the data path to the POCC be cut, commanding the experiment. This command path also serves as a fall back from the ground into AMS should problems arise with the LRDL. As ACOP is located inside the ISS and is accessible, it can be upgraded and modified as experience is gained in operating the LRDL and HRDL on ISS and as technologies evolve.

ACOP is implemented as a high end computer in a pull out drawer mounted inside an express rack inside the US Lab. Six hard disk drives are mounted on the drawer front panel. This provides sufficient capacity to record 20 days of AMS data without crew intervention. With the additional hard drives stored on board, a total of 100 days recording capacity is available on the ISS. The front panel also contains a simple button and screen user interface. More complicated functions can be accessed using a laptop networked into the rack.

6) Electronics in Space

Figure 137 summarizes the challenges faced by the AMS collaboration in preparing particle physics electronics for use in space. The key point for AMS-02 is that the electronics is derived from our experience with AMS-01 and is rigorously tested all the way from the design prototyping and component screening through box level acceptance tests. Another key is the selection of components. AMS has vastly different requirements than those for usual space electronics, both in terms of the performance and complexity and in terms of the resources. For example, in the Cryomagnet Avionics Box (CAB) it is not possible to connect completely redundant systems to the magnet, so heavy use is made of space grade components. In contrast the DAQ system primarily uses high grade commercial components and achieves reliability by interconnecting redundant elements. A key aspect of this selection is the measurement of cosmic ray heavy ion induced single event upsets and latch ups. Figure 138 shows one such set-up; however, the major effort in this regard is a series of beam tests at GSI, Darmstadt as shown in Figure 139. In the first round test (October 2000), candidate components were screened and in the second round (planned for October 2001) the required protection techniques will be tested.

Electronics in Low Earth Orbit

Challenge		Solution
Static loads	40+10+10 g	Design & Test
Vibration	6.3 g (rms)	
DePressure	1 to 0 bar / 2 min	
Zero G	Floaters	Conformal Coating
Vacuum	No Convection	Waste Heat Conduction
Thermal	-40,+80 C Survival -30,+50 C Operation	Parts Selection & Testing
Radiation	~ 1 KRad/year	TID Testing
Heavy Ions	Latch Ups, Bit Flips	Beam Testing, Error D/C
Atomic O	Etching	Material Selection
Solar UV	Aging	& Mechanical Shielding
MM/OD	Punctures	More Shielding
EMC	Noise, Requirements	Grounding, Filtering, Screen
Mag. Field	up to few 100 G	Testing, Placement
ACCESS	NONE for 3+ years	Reliability, Redundancy, Test

Design, production follow the processes validated on STS91.

Figure 137 : Challenges and solutions involved in flying state of the art electronics.

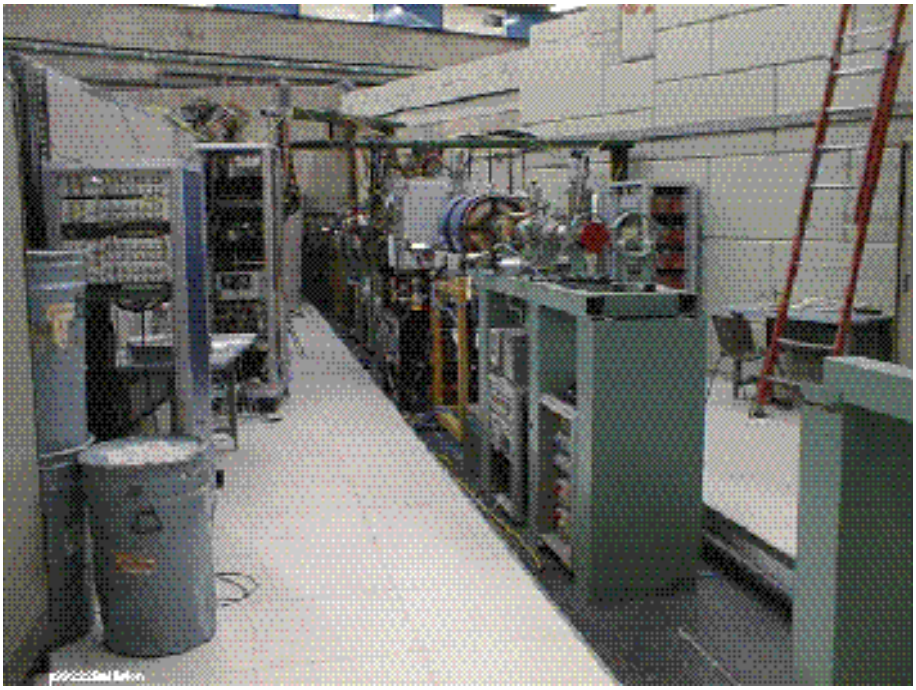

Figure 138 : Radiation tests in heavy-ion beam of AMS electronics, at INFN Catania accelerator, for electronic component selection.

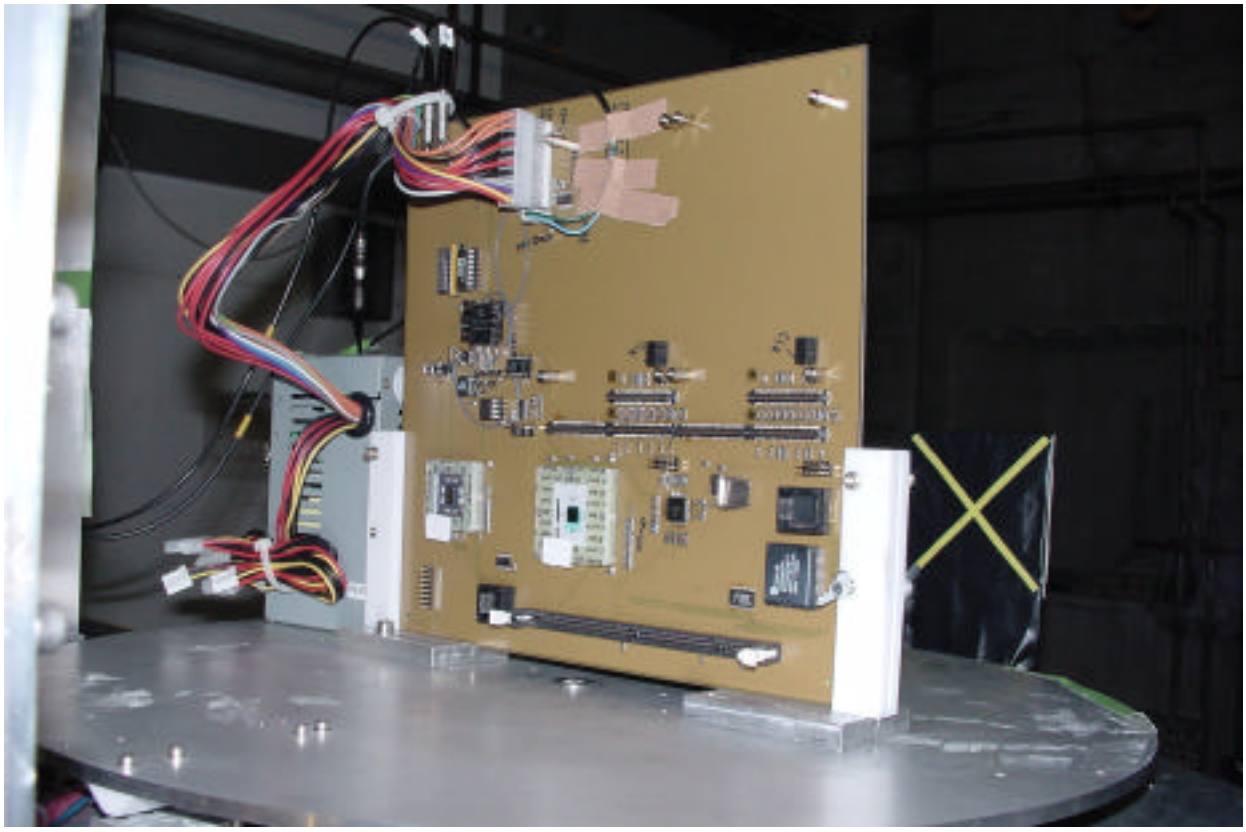

Figure 139 : JMDC under beam test at GSI.

Of particular concern is the thermal and thermal-mechanical design of the electronics. Our approach is summarized in Figure 140, which sketches a standard AMS electronics card mounted in a standard AMS crate, directly coupled to a radiator. About 30 different types of cards are being made and a total of 350 cards of all types will be flown. Eleven different crate configurations will be required and a total of 28 crates will be flown mounted in 6 racks which span the USS, as shown in Figure 26.

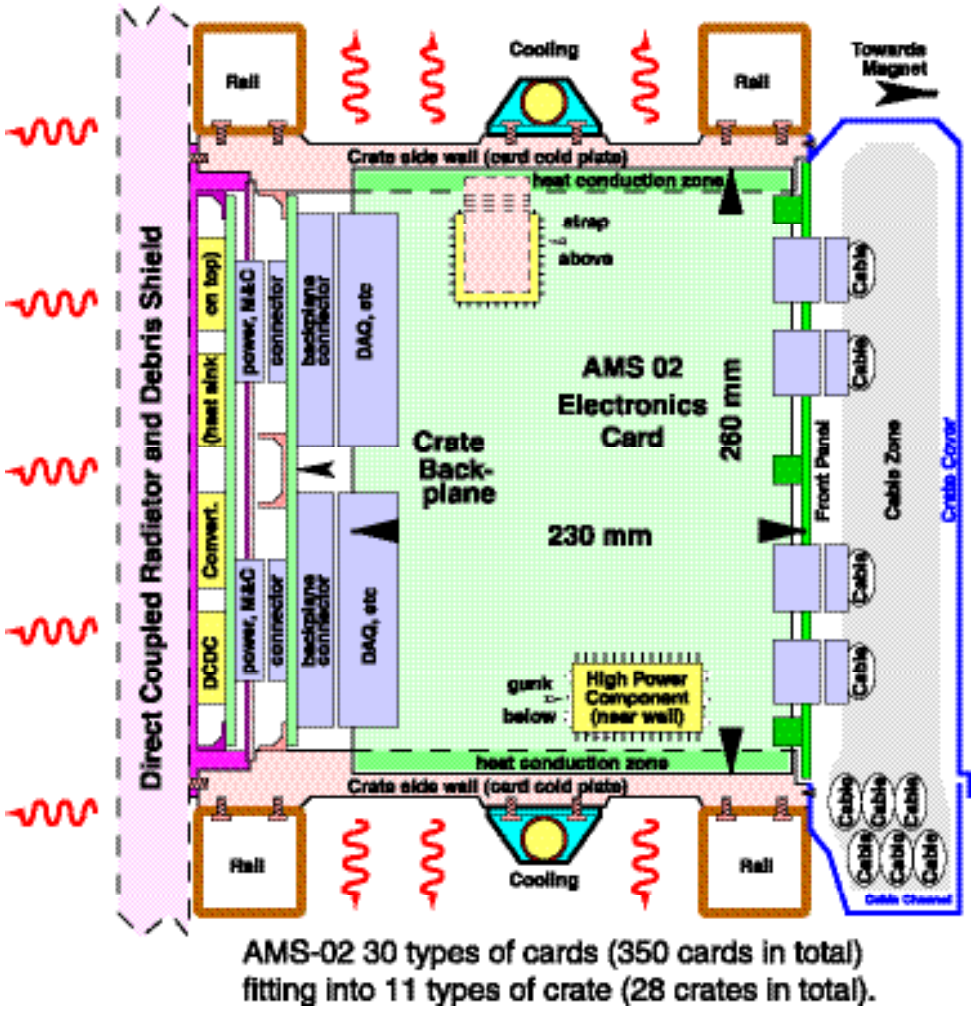

Figure 140 : Thermo-Mechanical design of a standard AMS electronics card.

7) AMS Electronics Organization

The electronics effort is coordinated by Dr M. Capell of MIT, and MIT is involved in most of the electronics:

X. Cai	Software design and programming of the JMDC computers and production of the JMDC test set ups.
G. Forconi	Software design and programming of the DSPs.
A. Kunin	Organization of the overall DAQ software effort and organization of the component beam tests.
V. Koutsenko	Design of the DSP boards and associated firmware and design of the TRD HV system.
A. Lebedev	Functional design of the DAQ, trigger and monitoring and control systems and data exchange protocols.
A. Rojkov	Design of JMDC and test boards.

As detailed below, our Taiwanese collaborators are making an enormous contribution to the electronics. The organization of this effort is shown in Figure 141. It is centered at the Chung-Shan Institute of Science & Technology (CSIST), which is again making available its extensive military grade design and production facilities, two examples of which are shown in Figure 142. The bulk of the electronics for AMS-02 will be produced and tested at CSIST. Board level thermal studies and thermal vacuum testing will be done at the Taiwanese National Space Program Office (NSPO).

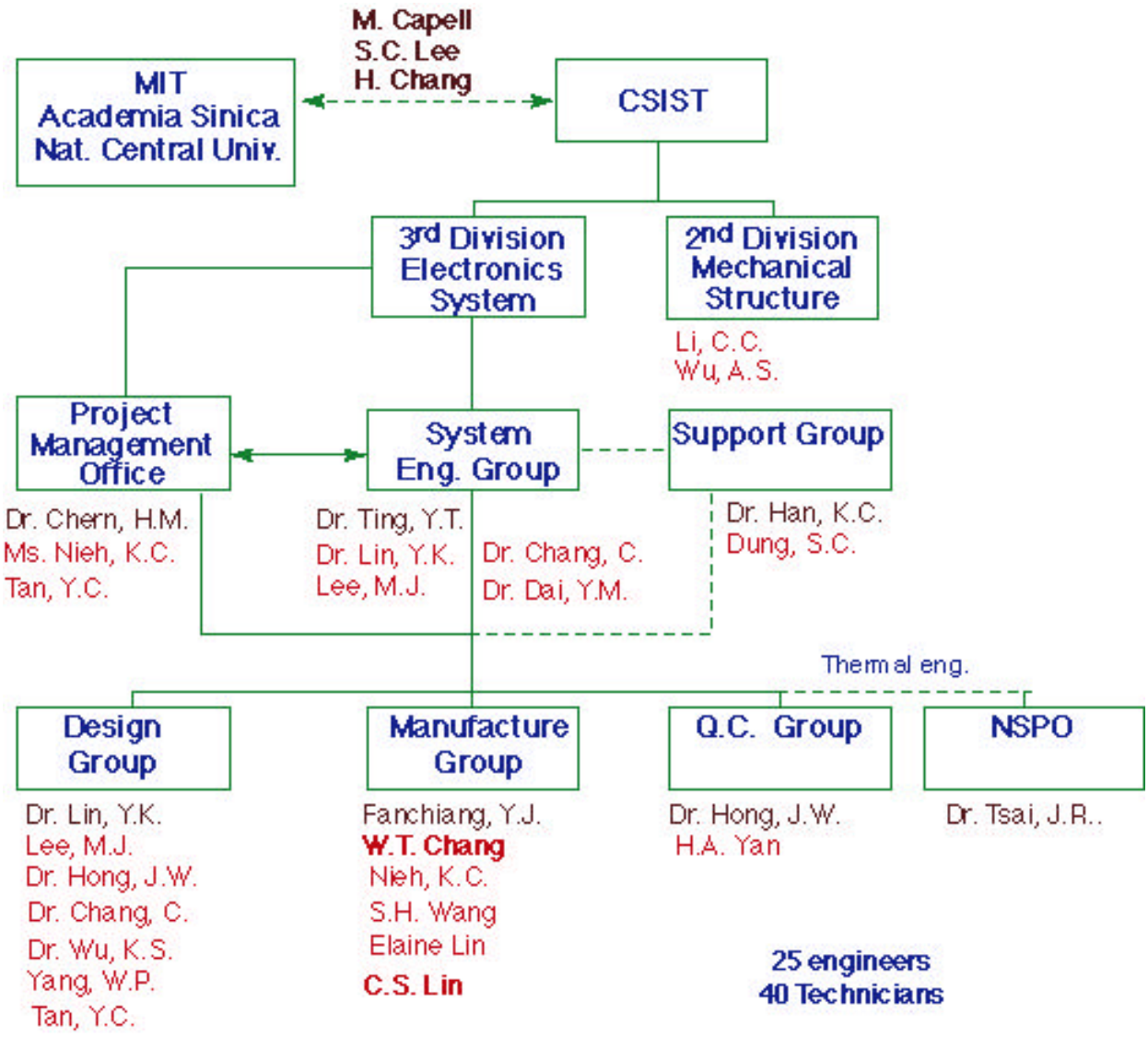

Figure 141 : Taiwanese contributions to AMS electronics.

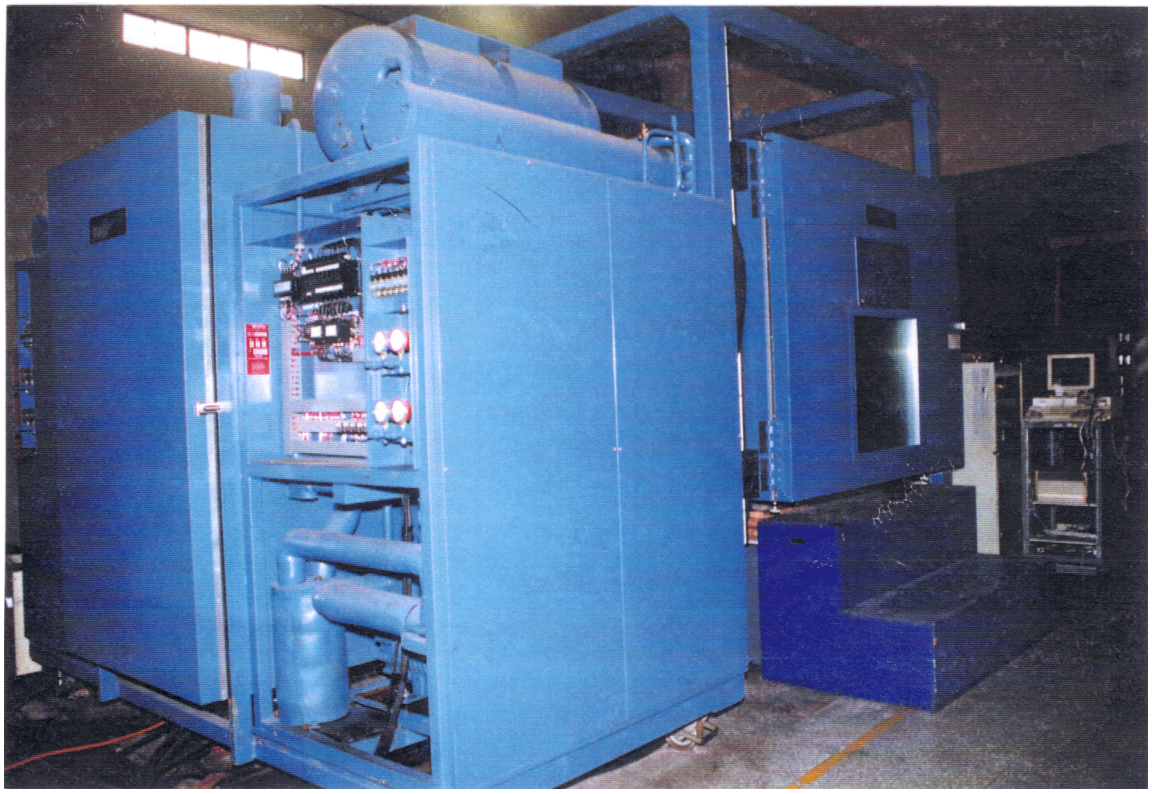

Figure 142a : Thermal Chamber for crate at CSIST.

Figures 142b : PCB production facilities made available to AMS at CSIST

For the tracker, based on AMS-01, the University of Geneva group has upgraded the current design and is producing the front end ASIC electronics. The Geneva group is also designing part of the front end DAQ board. The common digital part is being designed by MIT with assistance from the National Central University, Taiwan and it will be produced at CSIST, Taiwan, with parts procured by MIT and Academia Sinica of Taiwan. The power supply design is being done by INFN-Perugia based on DC-DC converters designed by CAEN under contract to MIT, and will likewise be produced at CSIST, as will the crates. The USCM boards to control the power supplies will be made by RWTH Aachen.

Similarly for the TRD, RWTH Aachen has the design and production responsibility of the front-end ASIC board and of the design of the TRD specific part of front-end DAQ board. The power supply will use the Tracker design. The rest of the design, including the HV supply, is being done by MIT. Except for the front-end ASIC board, all the TRD electronics and crates will be produced at CSIST. The electronics for the TRD gas system are under MIT and INFN-Rome responsibility and will use the USCM from Aachen.

The RICH front-end ASIC electronics is being made by ISN Grenoble and the rest of the electronics, power supplies and crates are under the responsibility of CIEMAT, Madrid, which will use the MIT designs for the common DAQ and DC-DC converters and also the USCM. The design of the high voltage system is in common with the ECAL.

LAPP-Annecy is designing the ECAL front-end ASIC and DAQ electronics using the MIT designs and the USCM. The high-voltage system is being made by INFN Pisa and Sienna, which are also sharing the production responsibilities for the electronics with LAPP-Annecy.

The time of flight electronics uses ASICs developed by MIT for AMS-01, the other common design elements and is under the responsibility of INFN Bologna. This design is also extended to include the veto counter electronics.

All of the groups are contributing to the on-board software effort. This effort is being coordinated by MIT and Taiwan.

The power distribution box is the responsibility of ETH-Zürich (in collaboration with RWTH), as are the monitoring and control electronics. ETH will also manage the inter-crate cabling

for power, DAQ and monitoring and control.

The global data acquisition and trigger system is being developed by MIT and Taiwan and will be built at CSIST. The JMDC computers are being designed directly by CSIST in close collaboration with MIT, especially as regards software.

The Italian Aerospace company, Carlo Gavazzi Space, is performing the thermal and mechanical design of the crates under contract to MIT.

ACOP has been funded by the Italian Space Agency, coordinated by R. Battiston and M. Capell and will be programmed by a collaboration group led by Helsinki Technical University.

The schedule for all of the electronics (which is not mounted directly on the subdetectors) is that it will be ready for integration at the end of 2002. Long term procurement for flight electronics has already started as prototyping continues through 2001.

8) AMS Ground Data Handling and Remote Commanding

The long duration of the AMS-02 mission in the International Space Station (ISS) makes the operation of the ground data handling complex fundamentally different from that of the AMS-01. Data analysis will be performed during the flight on a continuous basis. Detector experts will need access to scientific, calibration and monitoring data continuously.

Figure 143 shows our plans for Ground Data Handling and Remote Commanding System : an AMS-02 controlled computer located in the Payload Operations Integration Center (POIC) at Marshall Space Flight Center (MSFC) will act as an interface between the Internet and AMS allowing monitoring and control of AMS and collection and distribution of data. The computer will be located in the Huntsville Operations Science Center (HOSC) at MSFC and will be controlled and maintained by the AMS collaboration. This computer will have the following specifics duties:

- Receive high rate, low rate and ancillary data from AMS and the ISS, remove various NASA headers and store the data on local disks.
- Retransmit high rate, low rate and ancillary data to remote centers, where it will be stored permanently. Retransmission may be over the Internet or dedicated lines.
- Receive and verify commands from the remote POCC and retransmit to AMS via the ISS. While the location of the POCC may change from time to time, the POIC computer will only ever accept commands from the active remote POCC.

The POIC computer will use the Telescience Resource Kit (TreK) system to transmit data from MSFC to MIT and then on to CERN. Remote Payload Operations Command Centers (POCC) will be located both at MIT and at CERN, which will allow the monitoring and control of the experiment. Data will be continuously transmitted at the same rate which it is acquired by AMS (2 Mbit/s) and stored in both locations. Preliminary tests with the TreK system indicate the Internet has ample bandwidth to accommodate AMS data and a final design of the computer for the POIC and the TreK stations is in progress. The complete Ground Data Handling and Remote Commanding System is scheduled to be up and running six months before AMS launch to support AMS testing at KSC and the early installation of ACOP on the ISS. This effort is being led by P. Fisher and A. Klimentov of MIT. Funds and office space have been requested from MIT to accommodate the MIT POCC and Science Center. The space for a POCC at CERN has been approved by CERN.

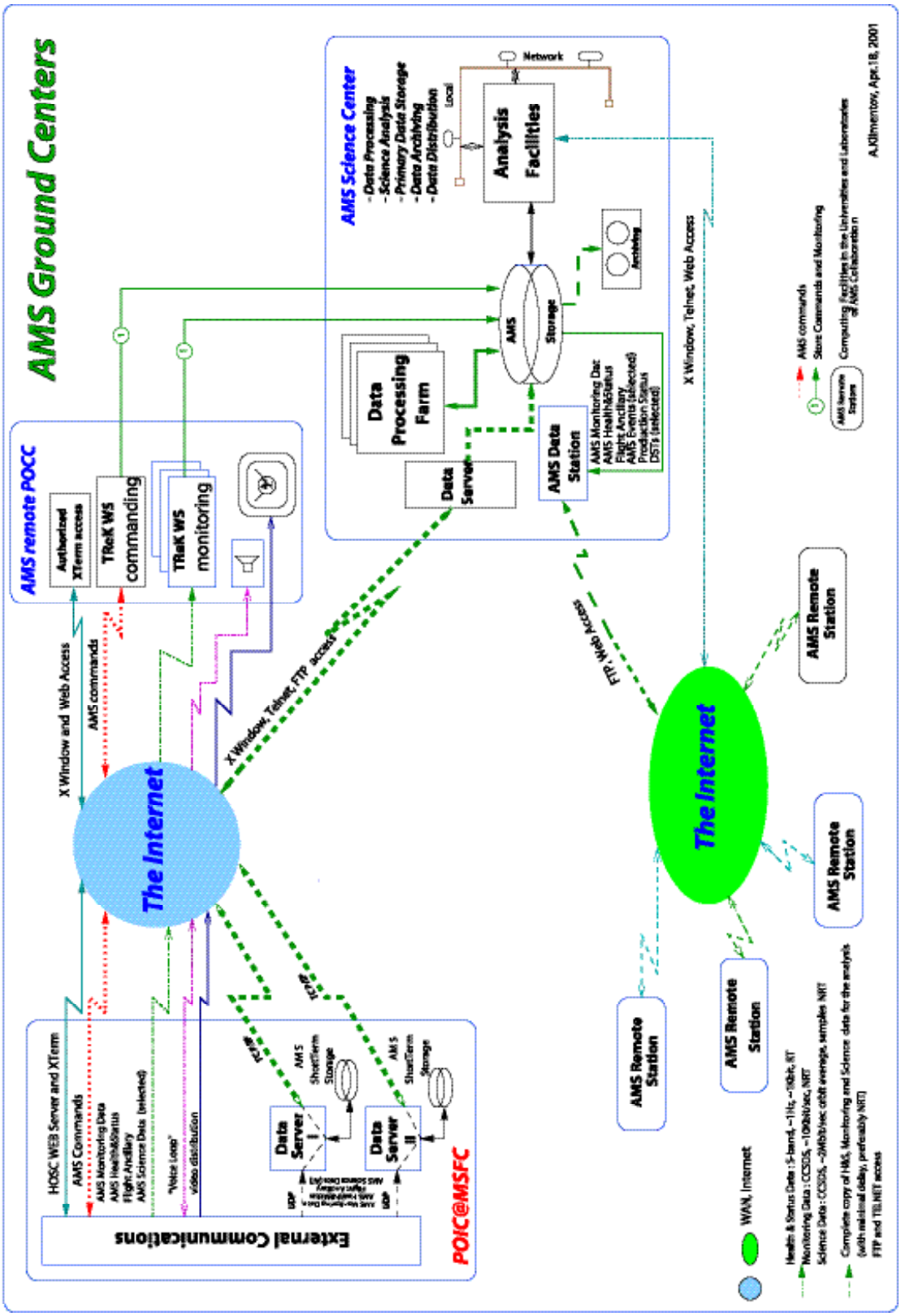

Figure 143: Data transmission from NASA-MSFC to remote AMS sites via the Internet.

IX. Monte Carlo predictions

AMS is scheduled to be installed on Space Station on space shuttle flight STS-127 on March 2004 (see photo below). AMS-02 will be the first major particle physics experiment on the Space Station.

The purpose of the AMS experiment is to perform accurate, large acceptance, high statistics, long-duration measurements of energetic (multi-TV) primary charged cosmic ray spectra in space.

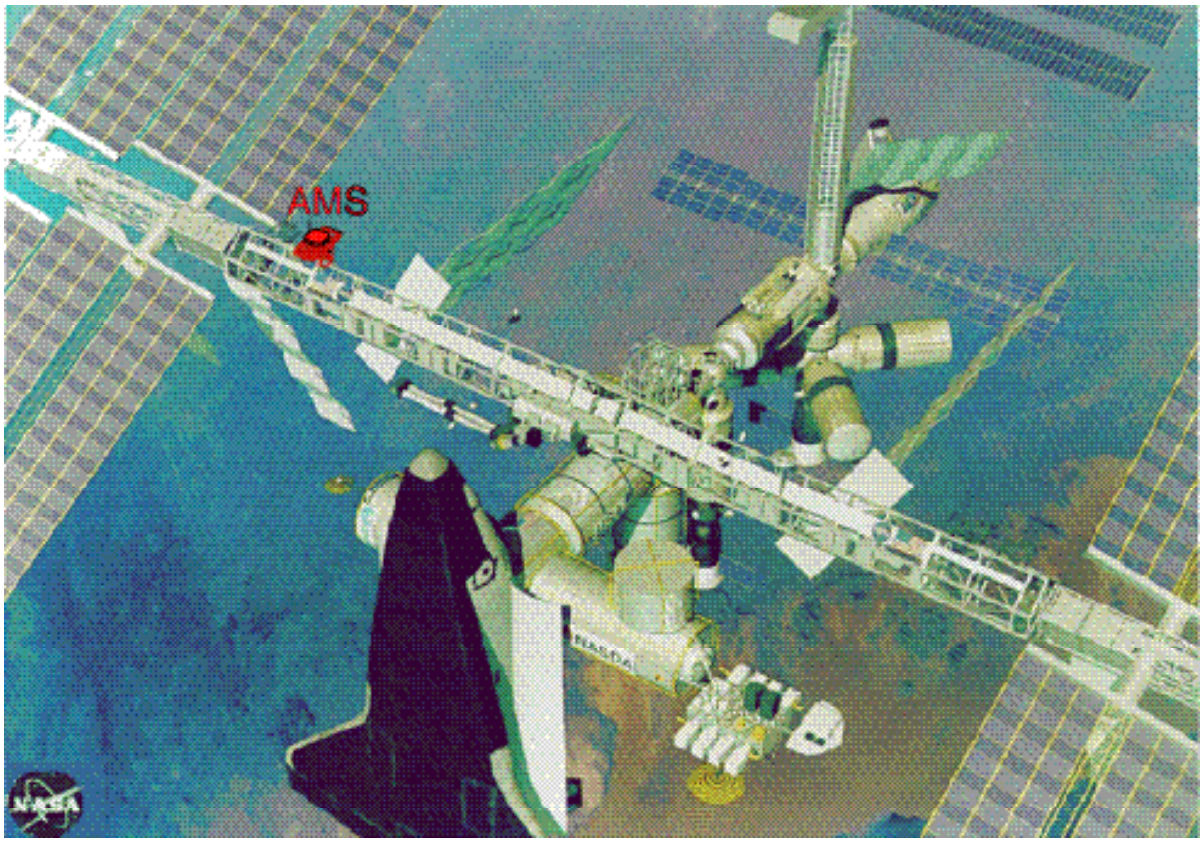

AMS-02 Flight: March 2004 – STS127. To be on Space Station for 3-5 years.

The overall AMS Monte Carlo simulation software has been developed by V. Choutko and A. Klimentov of MIT. Members of the MIT group coordinating subdetector simulations include V. Choutko, E. Choumilov and K. Scholberg.

We can predict AMS-02 sensitivity using our AMS-01 results and from balloon and satellite measurements, together with astrophysics models.

A few typical Monte Carlo results are presented here as examples for the physics potential of AMS.

As shown in Figure 144, we will see $2x10^9$ He events up to the rigidity of 3 TV. This represents many orders of magnitude improved sensitivity both in improved yield (by a factor of 10^3) and improved rigidity (by a factor of 20) as compared to the AMS-01 search for $\overline{He}$.

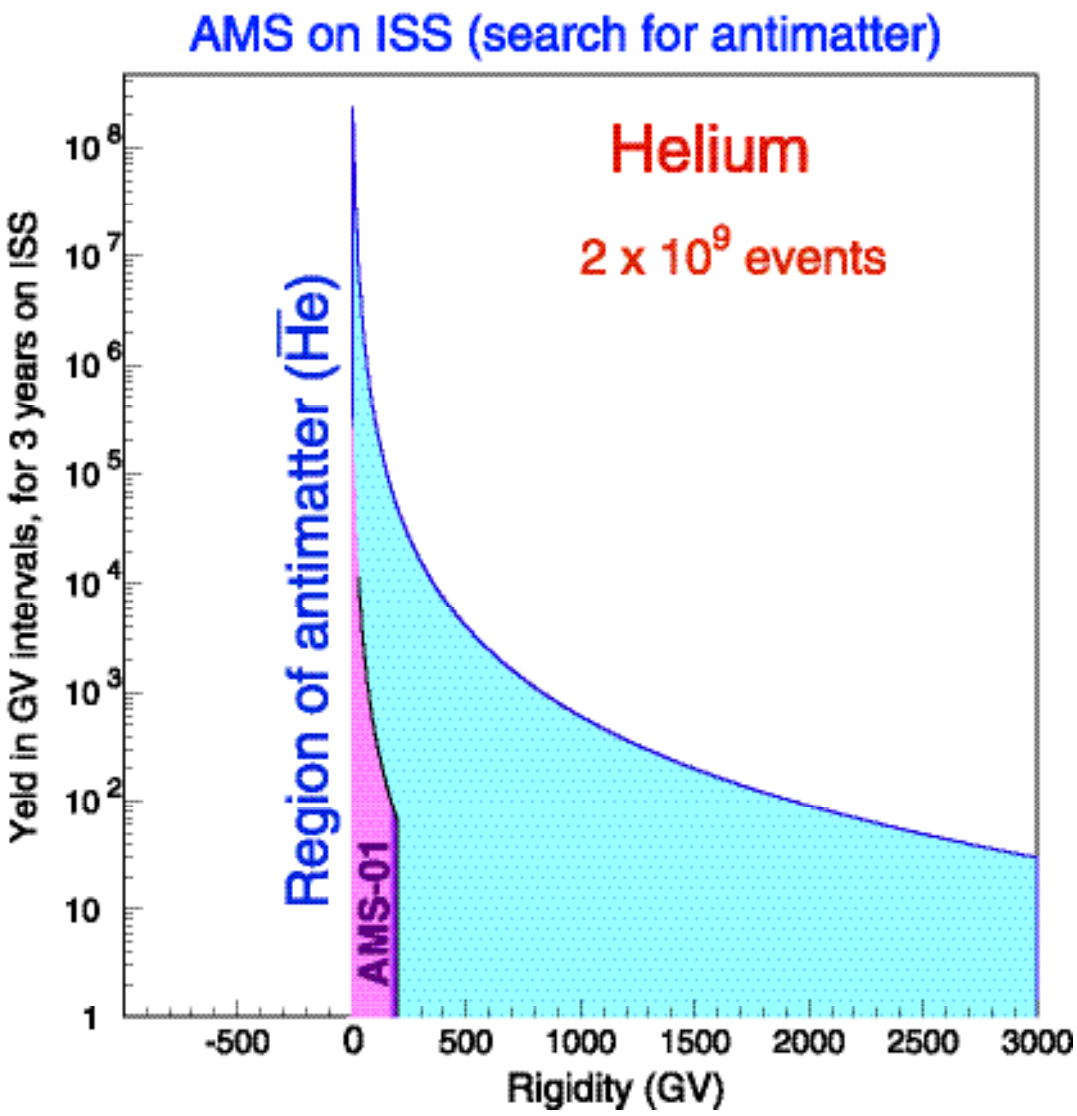

Figure 144: Yield of He. AMS-02 on ISS for 3 years as compared with AMS-01 results. (AMS-01 has 2.8 x 10^6 events up to 140 GV).

The proton and antiproton yield for AMS-02 is shown in Figure 145. As seen we will observe ~ 10^6 events with energy > 1 TeV. This provides an accurate study of very high energy cosmic rays. The accurate measurement of π will provide an independent tool to search for dark matter.

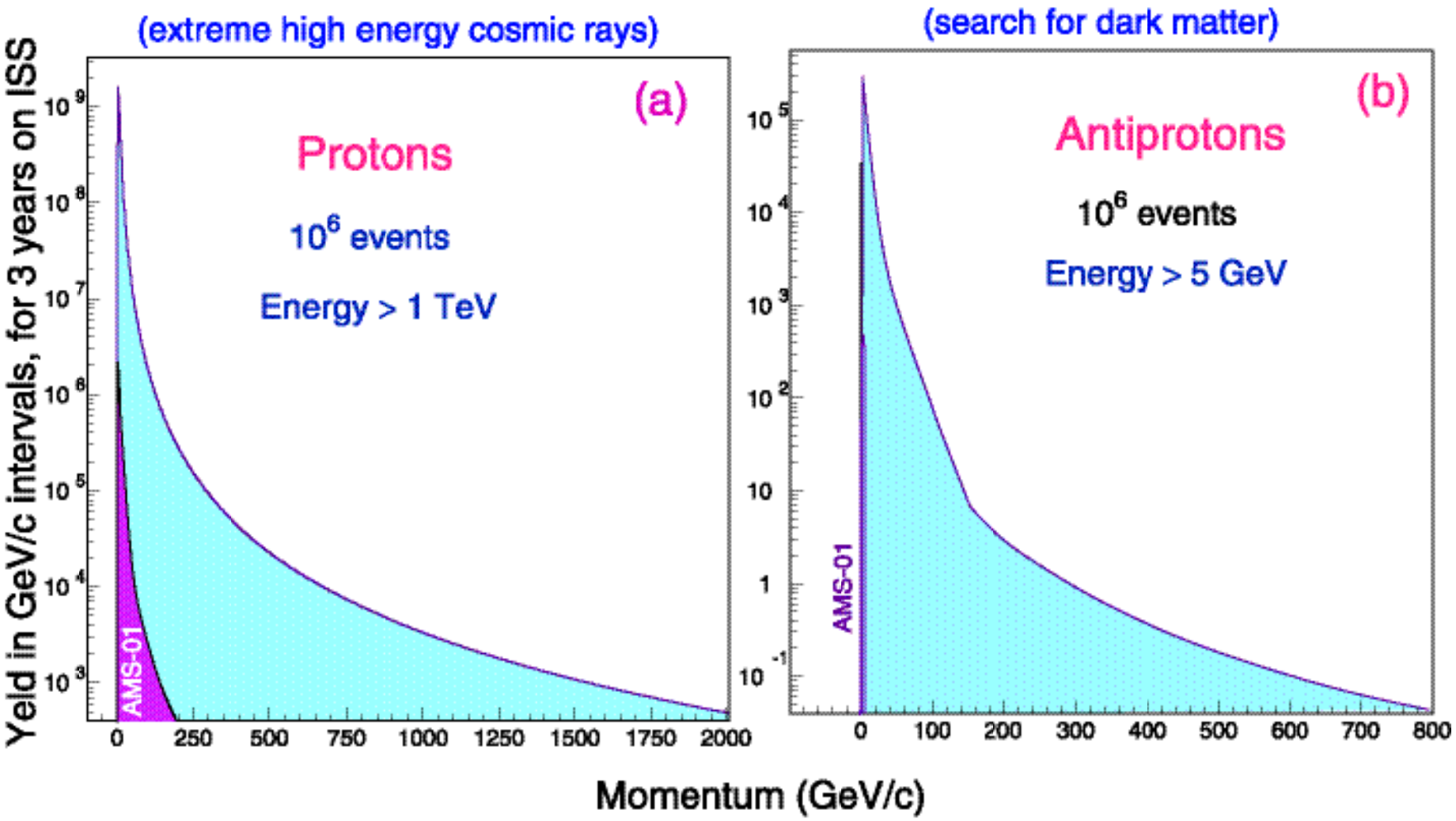

Figure 145: Monte Carlo yield of p $\bar{p}$, for AMS on ISS.

The e^-, e^+ yield for AMS-02 is shown in Figure 146. As seen we will measure accurately e^- up to 1.4 TeV with 10^7 events above 10 GeV and $2x10^6$ e^+ events > 5 GeV.

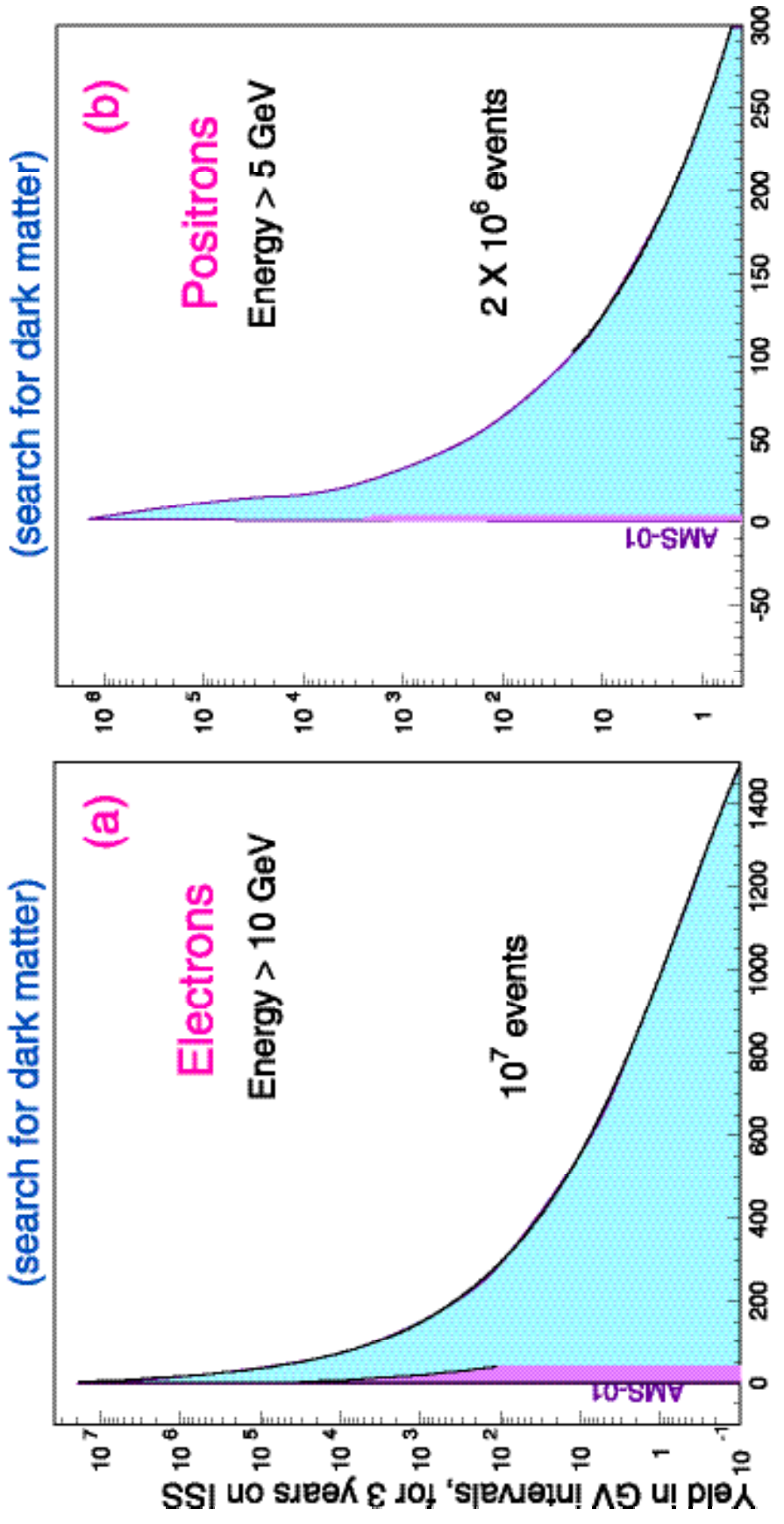

Figure 146: Monte Carlo yield of e^+, e^- in 3 years of AMS-02 on ISS.

The ratio of $e^+/(e^+ + e^-)$ provides a sensitive search for $\chi\chi \rightarrow e^+, e^-, \ldots$ This is shown in Figure 147.

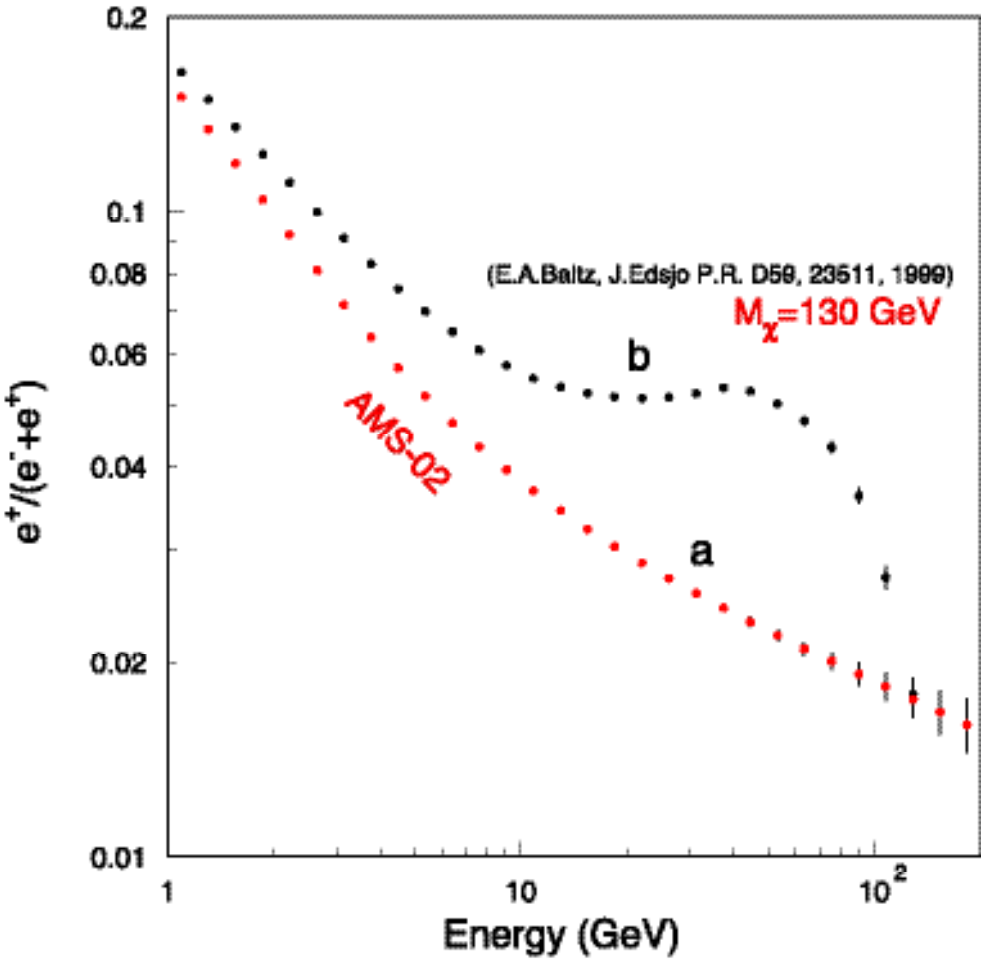

Figure 147: Sensitivity to Dark Matter. The ratio of $e^+/(e^+ + e^-)$ to AMS-02 without contribution for $\chi\chi$ annihilation (curve a) or with a χ at mass 130 GeV (curve b).

Since ^{10}Be has a life time of $2.8 \cdot 10^6$ years the ratio of ^{10}Be/^{9}Be provides us interesting information on the origin and propagation of cosmic rays (see Figure 148).

The mass resolution (Δm/m) capability of AMS for beryllium isotopes is shown in Figure 97 of section VI (RICH Counter). The isotope ^{10}Be can be separated from ^{9}Be clearly. The ability to make a high statistics determination of the ^{10}Be/^{9}Be ratio would enable AMS to achieve one of the most important measurements in cosmic ray physics, enabling (a) a highly accurate determination of the cosmic ray confinement time in the galaxy, and (b) a determination of the mean density of interstellar material traversed by cosmic rays. The ^{10}Be/^{9}Be ratio provides information concerning the amount of time cosmic rays spend in the halo of the galaxy.

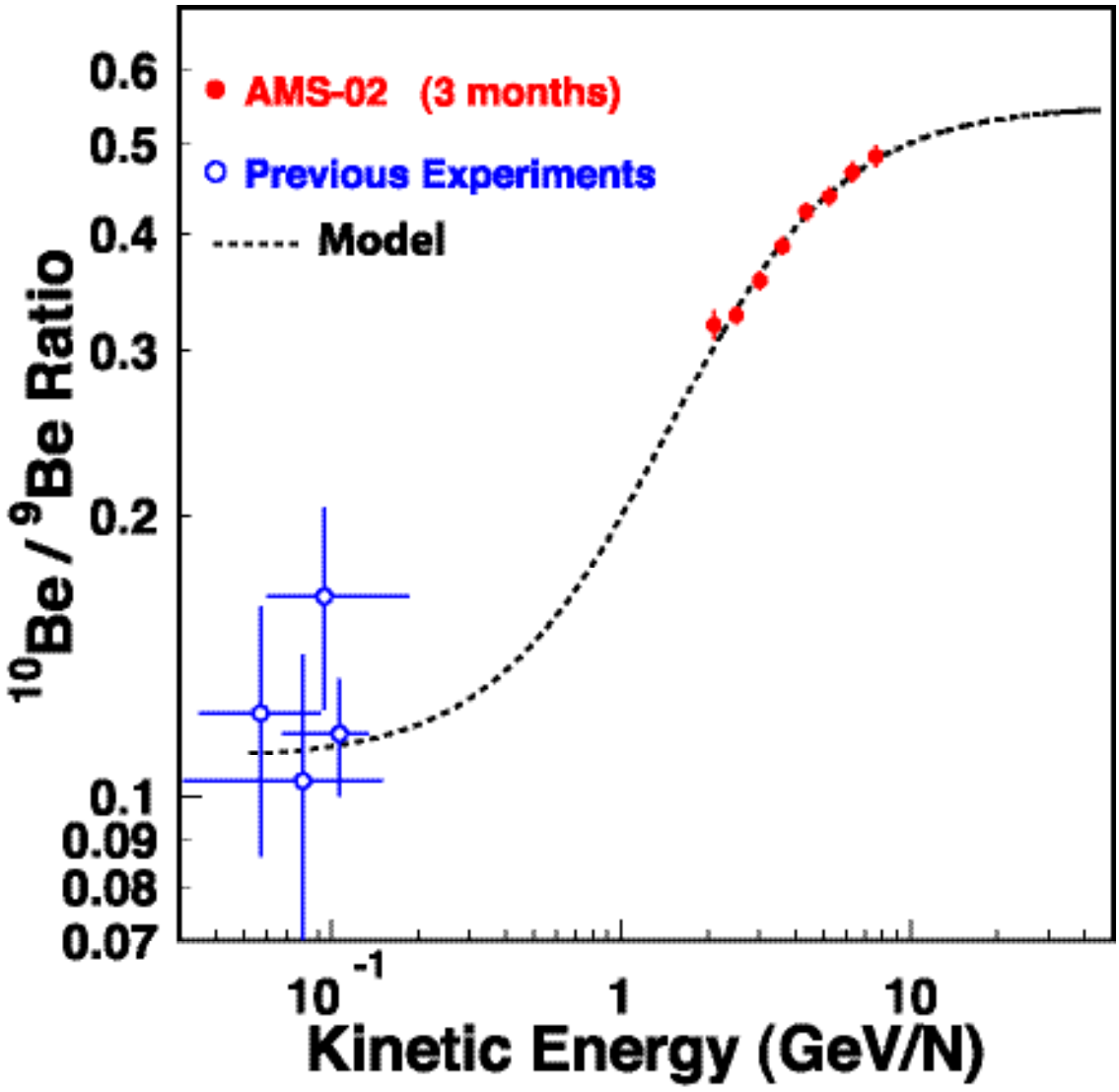

Figure 148: ^{10}Be / ^{9}Be energy dependence compared with a diffusion/convection model prediction together with the results from satellite measurement. AMS will be able to cover the high energy rise of the curve.

X. Conclusion

In conclusion, from the detailed description of the elements of AMS-02, progress is proceeding well and on schedule. After completion, each detector will be tested thouroughly in a particle or ion beam. In parallel, close attention is being paid by AMS and NASA engineers to ensure a successful detector integration program (see Tables 8 and 9). After the detector is fully assembled, it will be tested again in the CERN test beam and transported to Johnson Space Center for thermal-vacuum tests and then to Kennedy Space Center for final pre-flight processing before its launch to the International Space Station.